博士論文

# Electric field induced Insulator-Metal transition in $Ca_2RuO_4$

〔$Ca_2RuO_4$における電場誘起絶縁体金属転移〕

坂木　麻里子

広島大学大学院先端物質科学研究科

2014年3月

# 目次

## ３．参考論文


(1) Anisotropic giant magnetoresistance near the Mott transition in Pressurized $Ca_2RuO_4$
Fumihiko Nakamura, Ryuji Nakai, Tetsuo Takemoto, Mariko Sakaki, and Takashi Suzuki, Patricia Lebre Alireza, Satoru Nakatsuji, Yoshiteru Maeno
PHYSICAL REVIEW B **80**, 193103 (2009).

(2) Pressure induced novel-phenomena in Mott insulator $Ca_2RuO_4$
Y.Yamauchi, F.Nakamura, M.Sakaki, T.Takemoto, T.Suzuki, P.L.Alireza and Y.Maeno
Physica C**470** (2010) S877

(3) 公開特許 ペロブスカイト型酸化物の相転移誘起方法、電子機能素子材料として用いられているペロブスカイト型酸化物、ペロブスカイト型酸化物を用いた電子機能素子及び電子装置
中村　文彦、竹本　哲雄、坂木　麻里子、山内　洋平
JP 2010-166039 A 2010.7.29

# 主論文

## Contents

# Chapter1 Introduction

## 1.1 Introduction of 4*d* systems

The technology innovations based on electronic, optical, and magnetic materials have fundamentally changed the way we live. These technological revolutions would be impossible without continuous increases in our scientific understanding of materials, phenomena, and the processing and synthesis of these materials. The search for new materials is still the fundamental driving force for the continuous flourishing of modern technology.

In the last decade, there has been a growing interest in developing energy-saving devices based on novel quantum phenomena. In particular, the Mott transition is one of the most attractive many-body effects [1]. Extensive and intensive search for novel electronic materials has been carried out mainly in the strongly correlated electron system. Typically, the 3*d* transition metal oxides (TMO), including the cuprates and maganites are included. This class of materials has created great sensation in condensed matter physics by exhibiting exotic electronic and magnetic phenomena, such as high $T_c$ superconductivity and Colossal Magnetic Resistance (CMR), Mott (Metal-Insulator) transition (MIT) [2]. These phenomena are closely related to the strong electron-electron correlation, which originates from the on-site Coulomb repulsion between the localized 3*d*-orbitals electrons.

## 1.2 Ru 4*d*-electron systems

Ruthenates, the ruthenium oxides, have 4*d* electrons of the outermost electron. Electron configuration is 4*d*5*s*5*p*6*s*. The oxide include 2,3 cycle transition metal (Mo,Ru,Re,Os,Ir) is the optimum stage to study the absorbing phenomena. The 4*d* electron transition metal atoms have more extended orbitals compared with the 3*d* electron, and were thought to have smaller and insignificant electron-electron correlation effect. Because the 4*d* electron has a big expanse orbital more than 3*d* electron (ex, Mn), and the orbital hybridization is stronger, it must be sight set on the effect of "orbit".

Hence relatively less attention was paid to this class of materials. However, with the observations of numerous intriguing properties, such as unconventional superconductivity, Metal-Insulator transition, and non-Fermi liquid behavior, new attention is stimulated to the 4*d* oxides. Relatively few quantitative studies have been carried out on the 4*d* metal-insulator transition series and our understanding of this class of materials remains at a qualitative level.

Ruthenate is one of the few classes of materials that provide us with a rare opportunity to study the strong correlation in the 4*d* metal-insulator transition. The orbital degree of freedom is quenched in the *d* electron system, and it has itinerant characteristic. It has three degree of freedom "electron", "spin" and "orbital". It not only belongs to the transition metal oxides but also show superconductivity in both $Sr_2RuO_4$ [3,4] and $Ca_2RuO_4$ [5,6].

## 1.3 Perovskite structure

$Ca_2RuO_4$ has a perovskite structure. The perovskite compounds are formed by octahedron of $MO_6$ [transition metal (M) and around anion (O,Cl…)] in Fig1.1. The layer perovskite compounds have the alternating layer stacks $MO_6$ and block layer (Alkaline earth Metal and Alkyl group). $MO_2$ layer is at the center of $MO_6$ it plays the conduction layer. In most cases it is the lamination to *c*-axis, conduction layers and block layers are alternating layer stack to *ab*-plane. The conduction layer ($MO_2$) made of O and metal is *ab*-plane (vertical *c*-axis).

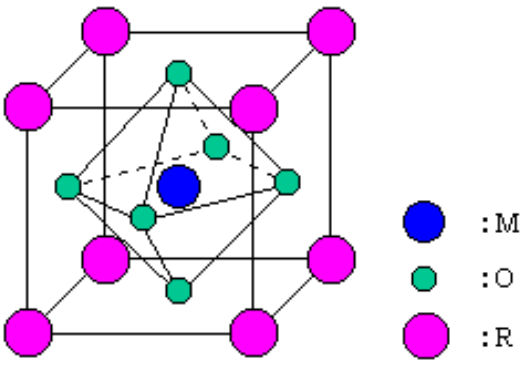


Figure 1.1 Perovskite structure with $MO_6$ octahertron

In the layer perovskite compounds, quasi-two dimensions characteristics become higher so that it is representative by a high-temperature superconductor. The thing necessary for the study (experiment) of this system is the single crystal, which is high quality with a little disorder. The dispersion by impurities tends to be increased in the strong correlation electron system, and fear covering the essential quantum critical phenomenon in particular is big in the cryogenic temperature.

### 1.3.1 Perovskite structure of the Ruthenate

Ru variety features a wide range of phenomena that are among the most important and interesting topics in the field of Condensed Matter Physics: Mott Metal-Insulator transition, metamagnetic transition, Colossal Magnetic Resistance, and Shubnikov-de Hass oscillations. As a result, any small perturbation such as an external magnetic field can readily tune the physical properties in the ground state.

The ruthenate system has aroused a lot of attention since the discovery of p-wave superconductivity in $Sr_2RuO_4$, consequently inspiring great enthusiasm in exploring the Ru-based Ruddlesden-Popper (RP) series. This series has the general formula $(Sr, Ca)_{n+1}Ru_nO_{3n+1}$, with n being the number of the coupled layers in one unit cell. They adopt layered perovskite structure ($ABO_3$) with the $RuO_6$ octahedron corner-share with each other to form planes, resembling a structure similar to that of the cuprate superconductors.

In this series, as *n* progresses from 1 to ∞, the number of the nearest-neighboring $RuO_6$ octahedra increases from four to six, representing a systematic enhancement of the structure dimensionality. The series is then found to have an astonishing and distinctive dimensionality dependence of all physical properties due to the strong magneto-elastic interactions between the Ru ions. For example, as *n* progress from 1 to ∞, the antiferromagnetic ordering is systematically suppressed for the $(Sr, Ca)_{n+1}Ru_nO_{3+1}$ system in Fig1.2.

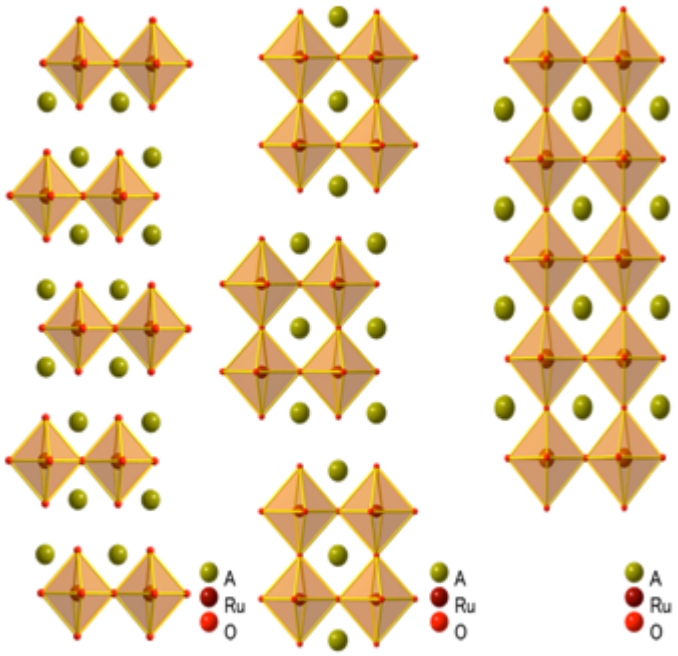


Figure 1.2 The layer perovskite compounds (left;n=1 214system,center;n=2 327system, right;n=∞ 113system).

The Ruddlesden-popper series $(Sr, Ca)_{n+1}Ru_nO_{3+1}$ (n = number of Ru-O layers in one unit cell) are perovskite based systems sharing the same $Ru^{4+}$ in an octahedral environments with corner sharing topology. However, despite the structure similarity, magnetic and electronic properties revealed in these series are extraordinarily diverse.

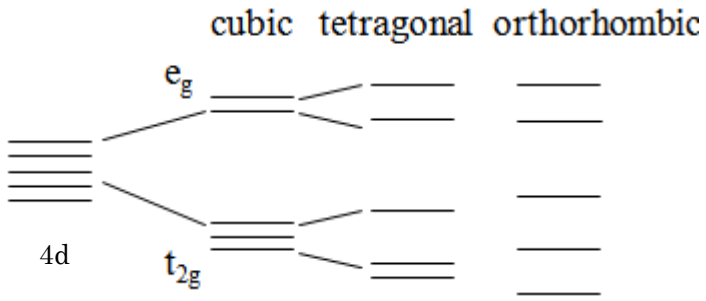


Figure 1.3 4*d* orbital splitting with crystal structure transition

### 1.3.2 Structural transition and electric state

Generally, with the 4*d* electron perovskite structure, it is reported that the 4*d* orbit is divided by the distortion of the crystal structure. Originally the 4*d* orbit degenerates five folds. $MO_6$ is piled up and is divided in $e_g$ (Two folds are retracted by shrinking) and the $t_{2g}$ (three folds are retracted by shrinking) orbit when it becomes cubic by making stratification. The $e_g$ orbit is divided more, and the $t_{2g}$ orbit is divided to one to two when it becomes tetragonal next. Finally all $t_{2g}$ orbits are divided, and it is in an energy state varying in all five orbits when it becomes orthorhombic in Fig1.3.

Both $Ca_2RuO_4$ and $Sr_2RuO_4$ have layered perovskite type structures, they form stratification octahedron of $RuO_6$ and block space of Ca/Sr. The order state with journey characteristics is very interesting. In addition, since the ionic size of $Ca^{2+}$ ($Ca^{2+}$ = 1.00Å) is smaller than that of $Sr^{2+}$ ($Sr^{2+}$ = 1.18Å), replacing Sr with Ca generally induces structure distortion, leading to smaller bandwidth.

This structural distortion induced by replacing $Ca^{2+}$ with $Sr^{2+}$ gives us an extra choice to explore this class of materials. The systematic variances of properties with dimensionality and structure distortion make the Ruddlesden-Popper series an excellent system to study the interplay between lattice, orbital, charges, and spin degrees of freedom in the 4*d* Metal-Insulator transition. See next chapter for a complete description.

## 1.4 The Ruddlesden-Popper series

### 1.4.1 n = 1 (214 series)

$Ca_2RuO_4$ is the Ruddlesden-Popper series $Ca/Sr_{n+1}Ru_nO_{2n+1}$ with n = 1, is a single layered system. In n = 1 series, Conduction layer (ex, $RuO_2$ layer in the case of $Ca_2RuO_4$) is made to separate to one level. The antiferromagnetic metallic phase intermediate between $T_N$ and $T_{MI}$ is rare for an un-doped compound at ambient pressure [7,8].

The isothermal magnetization measurement shows that for fields applied along the *a*- and *b*-, *c*-axis, the system remains at antiferromagnetic state. The study presented in this dissertation is then dedicated to further exploring its properties in greater detail.

In spin triplet superconduction material $Sr_2RuO_4$ is a reference material, it is apparent to do the exotic superconduction of the *p* wave with item three folds of spins with ground state. The crystal structure does not have a distortion, and symmetry of crystal is tetragonal. $Sr_2RuO_4$ has the same crystal structure (KNiF type) as the high-temperature superconductor (La system copper oxide), and the comparison with the high-temperature superconductor as the superconduction ($T_C$~1.5 K) in the stratified formation perovskite which does not include copper more at first alone.

$T_C$ is extremely lower ~1.5 K than a high-temperature superconductor, and r of the electronic specific heat coefficient is 39 mJ/K$^2$mo1. This value is considerably large. It is thought with the system that strong electronic correlation because there is 4 times of the prospective value from a band calculation.

Previous work on $Ca_2RuO_4$ has revealed strong anisotropy in structural, magnetic, and transport properties of this system, showing intimate couplings between lattice, spin and charge. However, the richness and complexity displayed in these properties indicate that the in-field state of this system is still far from being well understood.

This system has severe structure distortions due to the small ionic size of the $Ca^{2+}$, resulting in a rotation (on the *ab*-plane) and tilting (away from the *c*-axis) of the $RuO_6$ octahedra [7]. The tilting projects primarily along the *bc*-plane rather than the *ac*-plane, leading to a strong anisotropy between the *a*- and *b*-axis [7]. At low magnetic field, the system undergoes antiferromagnetic ordering at $T_N$= 56 K, followed by an abrupt metal-insulator transition.

### 1.4.2 n = 2 (327 series)

$Sr_3Ru_2O_7$ is the RP series $Ca/Sr_{n+1}Ru_nO_{2n+1}$ with n = 2, is a bilayered system intermediate between the superconductor $Sr_2RuO_4$ (n = 1) and the matallic paramagnet $SrRuO_3$ (n = $\infty$) .

In $Sr_3Ru_2O_7$, it was found that although the ferromagnetic state can reduce the $\rho_c$ (interplane resistivity or resistivity measured with both voltage and current running along the *c*-axis) by one-order of magnitude at 7.8 T when $B$ //$c$ (a magnetic easy-axis) [9,10]. Parallel study between the $M$ and $\rho_c$, together with the comparison between properties for *a*-axis and *b*-axis, suggest that the metamagnetic state could be intimately related to the degrees of freedom. In addition, the orbital degree of freedom is apparently associated with unusual quantum oscillations. In the following, I will describe a general reply to the each outside field.

## 1.5 Effect of external field

Pressure is a suitable tuning method to explore such novel phenomena; however, high-Pressure conditions are generally achieved in a complicated apparatus requiring sophisticated skills. In contrast, there has been growing recognition of applying an *E*-field as a complementary method to Pressure, since an insulator-metal switching, namely for controlling an *E*-field, has many advantages for practical use, especially for electronic devices. Moreover, application of *E*-fields can govern the electronic states directly, whereas Pressure tunes the electronic states indirectly via the change of lattice parameters.

### 1.5.1 Pressure effect

Recently, there has been growing interest in pressure effect on quantum phenomena such as unconventional superconductivity in strongly correlated electron system. This is because pressurization is generally known as a powerful tool to tune the properties of materials without introducing randomness.

In the neighborhood of Mott transition, a lot of novel quantum phenomena, such as the high temperature superconduction and the giant magnetoresistance effect are reported. For the elucidation of these novelty quantum phenomena, a lot of studies and experiments that applied external field to control of an electronic state are made. At

such a point, it may be said that static magnetic field and the still water pressure method are very effective techniques.

The experiment under the still water pressure method needs a very special technique. The information that we can observe is limited to each experiment under the still water pressure method. We cannot deny the height of the hurdle to treat it as a broad topic.

In addition, one method includes the *E*-field as a kind of outside field, by which we can control the parameter of this technique by adding outside ground to a material relatively easily. It is thought in electrostatic Carrier Doping, that the effect of the *E*-field generally corresponds to the number of carrier controls it holds.

Element substitution is possible by chemical technique if controls the number of carriers in the material simply. However, disorder is introduced into a crystal by the element substitution in . The element of the chemical disorder in a material is that we want to remove in the measurement of the essential quantum phenomenon as much as possible, as having touched on it some time ago.

In addition, it may be said that it is the technique that helped us to approach practical use more, even if one thinks about the control that is assumed by an *E*-field its outside ground from an applied side. The parameter is controlled by the electric field because one tied to the application, such as a new device or the magnetic memory directly. The parameter controlled by the *E*-field is tied to an application such as a new device, and the magnetic memory directly.

If the material, in which we can operate near room temperature by changing the composition ratio or the shapes is discovered, rapid progress like what is hard disks is expected. An *E*-field is effective for the study of the multi-ferroic material; where as applying it has the intersection correlation like as magnetic field or/and an *E*-field origin. Seeing both sides from there, the fundamental researches application, and the behavior that the material under the electric field shows from these points, is very interesting.

### 1.5.2 Pressure cell

Many of the ferromagnetic properties remain to be veiled because of a lack of a non-magnetic pressure cell allowing us to achieve pressure over 2 GPa at low temperatures in Fig1.4. We have recently developed a piston-cylinder pressure cell for a commercial SQUID magnetometer (Quantum Design, model MPMS) allowing us to achieve pressure of 2.1 GPa at low temperature [13].

### 1.5.3 Electric field

Generally, the electric field increases rapidly with a certain threshold value. It is called “the dielectric breakdown” when we apply an *E*-field to a solid. There are some models to explain it, and the bulk (genuine) destroy and the “snowslide” phenomenon that electronic it causes, the temperature rise due to the Joule fever.

Those phenomena are divided into two names (1) bulk transition done with a representative phenomenon Metal-Insulator transition and (2) local (of the filament like) phenomenon and is called dielectric breakdown. By the Insulator-Metal transition of the bulk, the threshold electric field is regarded as a thing peculiar to a material does not move to the size of the sample, form, an electrode, neighboring mediums. In addition, there are usually many "snowslide" phenomena to be heterogeneous, and to have such as impurities or the surface when threshold electric fields of the Insulator-Metal transitions are low.

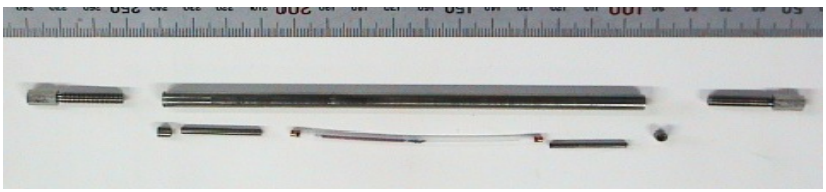

Figure 1.4 Pressure cell for model MPMS (upside is scale).

Let us mention two well-known examples of electric field induced phenomena. One is "electrostatic carrier doping" [11,12], which controls carrier density in a surface region of an insulator by an extremely large electric field. Indeed, electric field induced superconductivity has recently been reported in the surface layer of a band insulator $SrTiO_3$ by the electric field application of 20 kV/cm[13,14]. The other is a Mott transition induced by applying electric fields, namely, "switching".

Some transition-metal oxides in strongly correlated electron systems have gained attention as a candidate for the switching to practical use as an electronic device such as resistance RAM[15,16]. Most of these previously reported switching phenomena have been achieved only at low temperatures and/or high voltage (typically 1–100 kV/cm)[17-21]. In order to develop energy saving devices, it is essential to find a switching system driven at room temperature (RT) and by weak electric fields. An example is the metal-insulator-transition (MIT) induced above room temperature in films of a Mott insulator $VO_2$[17]. It would be desirable to find a system in which bulk metallic state is induced by electric switching with low *E*-field.

As another challenge, it is desirable to maintain the E-field-induced metallic state in a "volatile" switching system on cooling and identify interesting ground states, since there have been few such reports in a system stabilising a steady but nonequilibrium state.

## 1.6 Mott transition (Metal-Insulator transition)

The Mott transition (metal-insulator transition/ MIT) is the central strong correlation effect because it addresses directly the competition between the Coulomb repulsion energy and the kinetic energy. It occurs when an onsite Coulomb repulsion energy $U$ exceeds the electronic bandwidth $W$, leading to the breakdown of independent electron pictures [5]. $U/W > 1$ shows insulator state.

There are a variety of transition metal oxides that were predicted to be conductor by band theory turning out in fact to be insulators. For example, according to the band theory, for a material to be insulating, it is necessary to have an even number of electrons per unit cell in order to make its band fully occupied or empty.

On the other hand, with an odd number of electrons per unit cell, we will necessarily have a partially filled band, and the material must be metallic. But the prediction of the band theory fails in a number of cases. One of the old known, the clearest example is provided by the transition metal oxide CoO. The outer shell of Co has the configuration $3d^7 4s^2$ and the oxygen has $2s^2 2p^4$. The number of electrons per unit cell is then 15, an odd number. According to band theory, CoO should be metal. But in fact, CoO is one of the toughest insulators we have ever known.

Nevill Mott and R.Peierls then proposed that the strong correlations between electrons can be responsible for the insulating character of these materials. The theory they proposed addresses directly the competition between kinetic energy and Coulomb repulsion energy (or correlation energy) and is the central issue of strong correlation electrons. Different from the conventional insulator which can be predicted by band theory, a Mott insulator arises due to the correlation between electrons instead of incomplete filling of the *d*-bands.

The Hubbard model is one of the simplest approximations that describe the Mott insulator. It is built on two assumptions. First, only a single band has to be taken into account; second, the interaction is purely local, or in other words, we will consider only the on-site or intra-atomic Coulomb interaction between electrons.

The Hubbard model relies on the tight-binding model to describe the itinerant tendency for electrons to jump between neighboring atoms, and also considers the localized tendency with on-site electron-electron repulsion that is not usually considered in regular band theories. These two tendencies, represented by $W$ and $U$, compete to determine whether the materials is conducting or insulating and will drive the materials through Mott transition from a metallic state to insulating state.

The Hamiltonian for this model is then expressed as the sum of the band energy and Coulomb interaction energy, representing the itinerant tendency and the localization tendency. The Hubbard gap is usually defined as “the difference between $U$ and $W$”. The two bands that are separated by the Hubbard gap are called the "upper Hubbard band" and "lower Hubbard band" respectively. These two sub-bands may look like the valence and conduction band of a semiconductor, but in fact they are not the same.

For a valence of a conduction band, each band can hold up to $2L$ ($L$ is the number of the lattice sites) electrons, while the Hubbard sub-bands can't contain more than $L$ electrons. The splitting into two Hubbard bands is a correlation effect that could not be described by independent electron theories.

The system should then be treated in the charge transfer regime with an ionic model. On the other hand, if the energy of the Hubbard lower band is higher than that of the O $2p$ band, then $U > \Delta pd$, the charge excitation is between the Hubbard subbands and the system can be treated with a Mott-Hubbard model. Ruthenates, compared with the early $3d$ TMO which are classified to be in the Mott Hubbard regime, have smaller $U$ (~1.8 eV) and larger $\Delta pd$ (~3.2 eV) (for the case of $SrRuO_3$) and should be treated with the Mott-Hubbard model as well [26]. Since the discovery of high temperature superconductivity in layered cuprates, the issue of the Mott transition in a quasi-two-dimensional system has become especially important.

### 1.6.1 Mott-Insulator and effect of external field

The study to let Mott insulator become metal as bulk so far in an electric field is reported in $La_{2-x}Sr_xNiO_4$ or $Sr_2CuO_3$. Those threshold electric fields need number of few kV/cm and a considerable high electric field. I summarized the threshold electric field of representative the Mott insulator in a list. I referred to it about one of a representative semiconductor for a comparison.

In addition, as for applying an electric field to Mott insulator, it is thought with filling control if we assume the effect of the electric field the control in Fig 1.5. However, electric field is unlike the substitution of the material. Sample can control an electronic number without introducing direct disorder in itself.

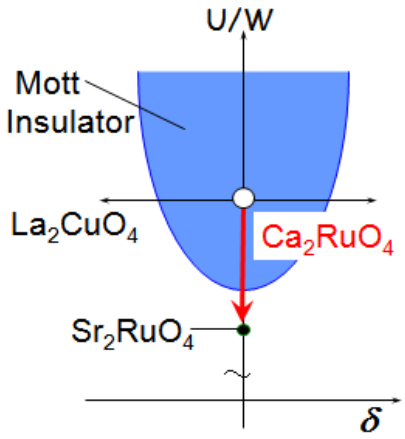


Figure 1.5 The MODEL of Mott Metal-Insulator transition

## 1.6.2 Mott-Hubbard model in Ruthenates

Layered ruthenium oxides $(Sr/Ca)_{n+1}Ru_nO_{3n+1}$ are similar to the cuprates in terms of structure. The bandwidth $W$ of this system can be well tuned by varying the dimensionality and the Sr/Ca ratio, giving rise to the different Mott parameter $U/W$. Varying the transition element itself can induce a greater change due to the different ability of the transition elements to overlap with their surroundings. Dimensionality is another important parameter that is found to be effective in the alteration of $W/U$ ratio. These factors are subtle and interweave with different kinds of couplings, making the studies of the Mott transition even more challenging and interesting as well.

By investigating physical parameters such as $t$ (charge transfer energy), $U$ (Coulomb repulsion energy), and $10D_q$ (crystal field splitting energy), it is found that although the $U$ values of $4d$ metal-insulator transition oxides are smaller than those of $3d$. Their $t = \Delta_{pd}$ and $10D_q$ values are relatively larger, so that the more extended $4d$ -orbitals electrons have weaker on-site Coulomb repulsion energy $U$, (~1 to 2 eV) but stronger hybrization energy, $W$ (~2 to 5 eV) with the neighboring O $2p$-orbitals. When the ratio of $W/U$ is comparable, the competition between these two energies gives rise to rich and complex phases for this class of materials. In addition, due to the small value of $U$, the roles $4d$-orbitals become more important and the spin-orbit coupling is then significant.

Methods to make by Mott insulator to metal here include two methods. One is filling

control by the valence different elemental substitution of the atomic value, the other one is band control by the different atomic radius with equal elemental substitution. When I look at the electronic state of $Ca_2RuO_4$, 4 electrons existing around one Ru ion take low spin state after the degeneration was removed in 5 folds, it enters the dε-orbit of the ground state.

When the electron of the dε orbit originally stands in line according to hund-rule, it takes anti-parallelism and should enter the same level, but exist with parallelism because $U$ is bigger than $W$. Two electrons cannot occupy the same orbit and are located in two orbits. Thus, $Ca_2RuO_4$ takes a Mott insulator state under room temperature and ordinary pressure.

### 1.6.3 Electronic correlations

After almost a century's effort, the physical properties of some solids have been successfully explained with an independent particle picture, in which the interactions between the electrons can be ignored or well represented by an average potential. The macroscopic behavior of a system can then be understood by starting from a detailed description of the individual particles and the way they interact.

Band theory is one of the approximations that are built based on this picture. It provides a conceptually simple explanation for electron transport. This approximation has proven remarkably accurate for estimating electron flow in silicon chips and many other materials.

However, there are materials such as CoO whose transport behavior disobeys the prediction from this theory. The Mott insulator is one of these types of materials. They are fundamentally different from the conventional (band) insulators. The conductivity of the latter is blocked by the Pauli Exclusion principles.

In a Mott insulator, the conductivity is blocked instead by the electron-electron Coulomb repulsion, or strong electronic correlation. To minimize the Coulomb repulsion energy, electrons have to stay away from each other as far as possible and tend to be localized. As a result, the electrons can "see" each other and the statistic correlations

between the motions of individual electrons are important.

In such cases, an independent particle picture is inappropriate and a many body model has to be considered. Materials with strong electronic correlation generally display a broad range of interesting phenomena that show departure from the standard model of solids, such as metal-insulator transition, colossal-magneto-resistance (CMR), and high $T_C$ superconductivity. Transition metal oxides (TMO) are this kind of materials that feature electronic correlation. These properties arise mainly due to the *d*-orbital wave functions which are confined more closely to the nucleus than for *s* or *p* states of comparable energy.

As a result, the overlap between the transition metal ions and the neighboring metal ions is small and the electrons in this system can move only through the hybridization with oxygen. The electronic correlation usually involves the interactions between the charge, spin, lattice, and orbital degrees of freedom in a nonlinear, synergetic manner, leading to an intrinsic complexity such as the coexistence of several competing states.

Theoretically, it has always been difficult to deal with strongly correlated electron systems. After several decades of efforts, even the basic properties of the strongly correlated electron system, such as linear temperature dependence of resistivity, are still beyond our understanding. The difficulty arises mainly from the wide range of energy scales involved and many competing orderings and instabilities that are associated with small differences in energy.

One of the frontiers in strongly correlated electron physics, Dynamical Mean Field Theory, is to develop new concepts and new computational methods to describe electronic states between the itinerant and localized states. Dynamical Mean Field Theory has led to some significant advances in our understanding of strongly correlated systems. Different from the static mean field theory which could not describe the strong electronic correlation between the electrons, the Dynamical Mean Field Theory is able to treat the many-body system both in momentum-space and in real-space, thus capable of describing both the wave-like and particle-like characters of the strongly correlated electrons. The Dynamical Mean Field Theory has been very successful in reproducing complicated physical properties in a variety of materials and it would continue to be one of the most powerful tools that help us to better understand complicated phenomena in transition metal oxides.

## 1.7 Background of $Ca_2RuO_4$

We have devoted considerable efforts on the Mott insulator $Ca_2RuO_4$ to induce switching and explore its ground state because $Ca_2RuO_4$ has the following versatile properties. Firstly, pressurised $Ca_2RuO_4$ displays a variety of quantum states, ranging from an antiferromagnetic (AFM) Mott insulator to superconductivity via a ferromagnetic (FM) quasi-two-dimensional metal [22-24]. Secondly, the magnetic and electronic properties of $Ca_2RuO_4$ are known to be quite sensitive to coupling of spin, charge and the orbital degrees of freedom [25,26]. Lastly, the metalisation of the Mott insulator $Ca_2RuO_4$ can be achieved by heating above $T_{MIT}$ = 357 K[27].

### 1.7.1 The historical background of $Ca_2RuO_4$

The first compound $Ca_2RuO_4$, which is a superconductor for pressure above 9 GPa and $T$<0.4 K and is also a Mott insulator. In $Ca_2RuO_4$ the transition from an insulator to a metal can be induced by temperature (357 K), by pressure (0.5 GPa) in Fig 1.6 [28] and by substitution with strontium ($Ca_{2-x}Sr_xRuO_4$, x = 0.2). Just recently, it was found that a small electric field could also unduced the metal-insulator transition in $Ca_2RuO_4$.

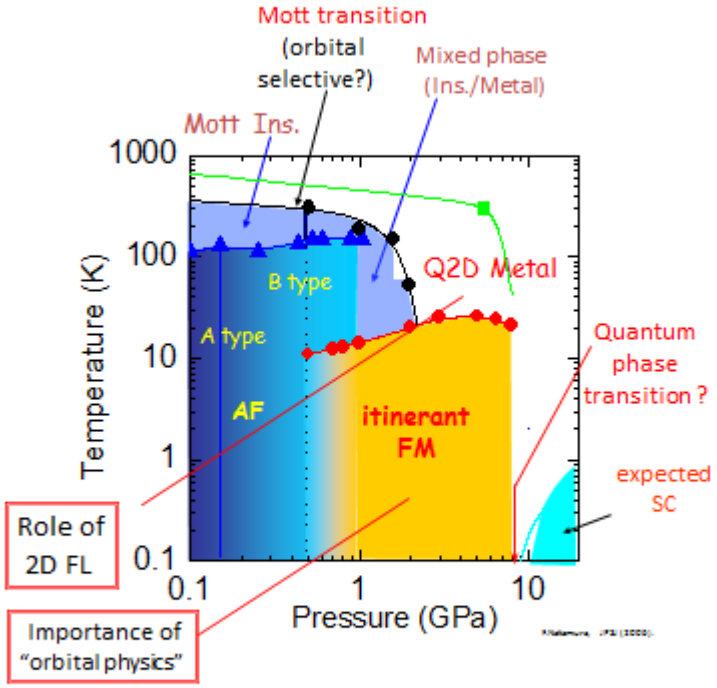


Figure 1.6 Pressure phase in $Ca_2RuO_4$

This is noteworthy in such as the electric field needed is far smaller than those needed to induce the metal-insulator transition in other common Mott Insulators. The Mott transition is induced by such a small field that it even becomes interesting for applications. This phenomenon was one of the main interests of this work.

The gap energy in $Ca_2RuO_4$ is 0.2 eV determined from the activation energy based on the temperature (T) dependence of resistivity [29]. On the basis of a simple Zener breakdown model [30], we estimate $E_{th}$ for $Ca_2RuO_4$ to be, 4 MV/cm (we use here the in-plane lattice spacing of a = 5.45Å. Since $E_F$ has been unknown for $Ca_2RuO_4$, the Fermi energy of $E_F$ ~0.2 eV for the c band of $Sr_2RuO_4$ )[31].

## 1.7.2 Crystal Structure

The Ru-214series $Ca_2RuO_4$ and $Sr_2RuO_4$ are perovskite based systems − the type of $K_2NiF_4$ with single layers of $RuO_6$ octahedral corner-sharing with each other. The single-layered $RuO_6$ forms planes with the Ca-O layers intervening within and between them. The Ca-O layer helps stabilize the perovskite structure without contributing to the total spins of this system. Since no oxygen ions within the intervening Ca-O layer are shared by the Ru ions of the adjacent double layers, the exchange interactions and conductivity perpendicular to the RuO planes would be weaker compared to those within the RuO planes.

In the other end product, $Ca_2RuO_4$, the space group is accordingly *Pbca* (orthorhombic), with the S- *Pbca* (at room temperature at ambient pressure) phase up to the first order phase transition at 537 K where the phase becomes L-*Pbca*. Lattice parameters are $a$= 5.41Å, $b$= 5.50Å, $c$= 11.94Å at room temperature at ambient pressure . In this thesis, we take $c$-axis as the short axis with space group S-*Pbca* in Fig1.7 [8]. Similarly, a change of the crystal structure is reported by the pressure dependence in Fig1.8[35].

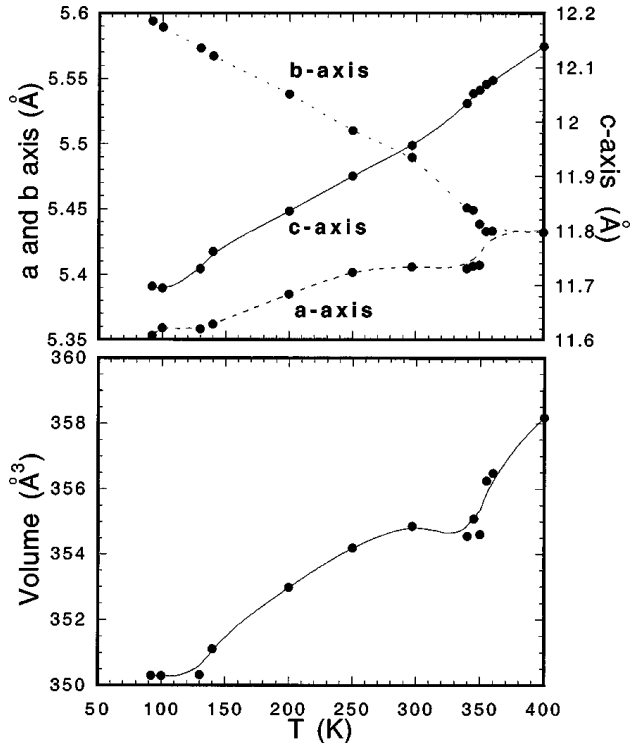


Figure 1.7 upper: Temperature dependence of lattice parameter,
Low: Temperature dependence of volume

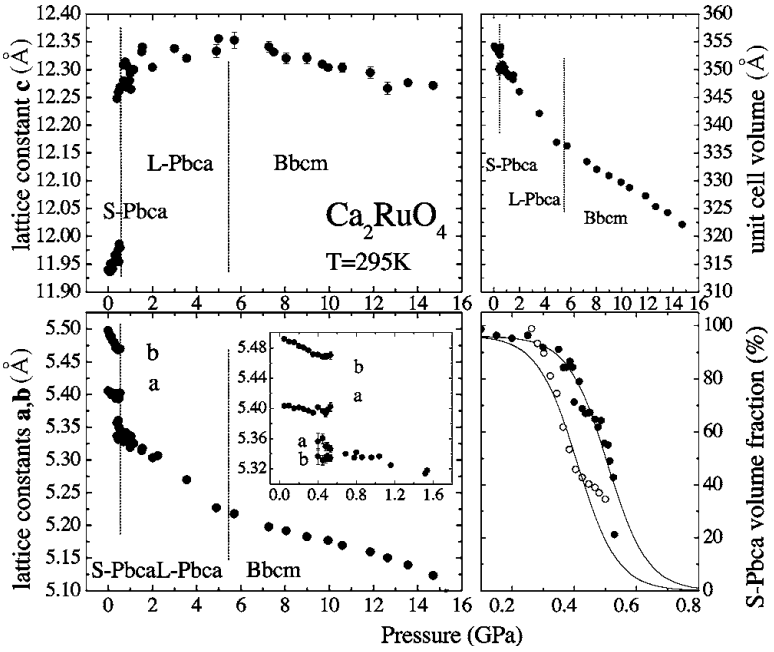


Figure 1.8 Left: Pressure dependence of the lattice parameter. Upper right: Evolution of the unit-cell. Lower right: Hysteresis of the *S*-Pbca volume fraction.

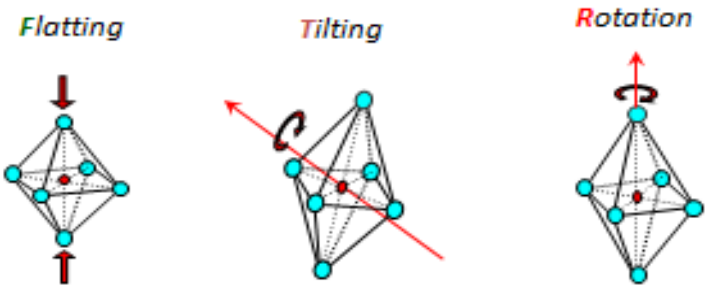


Figure 1.9 $RuO_6$ distorsion.

The three kinds distortion exhibits itself as "Flatting" "Tilting" "Rotation" of the $RuO_6$-octahedral in S-*Pbca*. Flatting is compression to the *c* axial direction of the octahedron so that top oxygen of the octahedron gets closer to a Ru-$O_2$ plane. Tilting is the angle of rotation $\theta$ to turn the angle of rotation of the octahedron to the that assumed [010] direction of axis away from the *c*-axis [110]. Rotation is the angle of rotation $\Phi$ around *c*-axis of the crystal Fig 1.9,10.

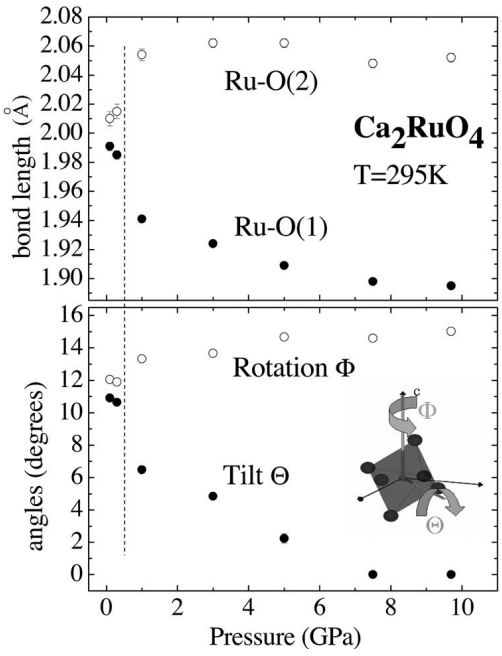


Figure 1.10[35] upper: Pressure dependence of the Ru-O bond lengths.
Low: Pressure dependence distortion (Rotation, Tilt) angles of the $RuO_6$ octahedra.

It is reported in transition of temperature dependence and pressure dependence, that it is caused by the distorted cancellation of the $RuO_6$ octahedron, being considered to be it at the time of the representative Insulator-Metal metastasis.

For $Ca_2RuO_4$, since the exchange interaction is limited to be within the *ab*-plane, the lattice distortion induced by the $Ca_2RuO_4$ ions turns out to be one of the dominant energy terms in the interaction pictures, which results in severe structure transition by the external field. However for $CaRuO_3$, when the dimensionality is higher, the structural distortions are not that important, as indicated by the similar resistivity behaviors between $SrRuO_3$ and $CaRuO_3$.

As a bilayered system which lies between n = 1 and n = ∞, $Ca_2RuO_4$ is believed to be placed in a unique position at which the orbital degree of freedom plays a critical role in determining the physical properties. The orbital degree of freedom is sensitive to lattice via orbital-lattice coupling, and to the magnetic field via spin-orbital coupling. In this chapter, we are going to probe the orbital physics through magnetic field, pressured field and elemental substitution tunings.

## 1.7.4 Resistance, Magnetic susceptibility

$Ca_2RuO_4$ is a Mott insulator with antiferromagnetic. The magnetic transition occurs at Neel temperature, $T_N$ = 110K, going from a paramagnetic state to antiferromagnetic state in Fig 1.11[8].

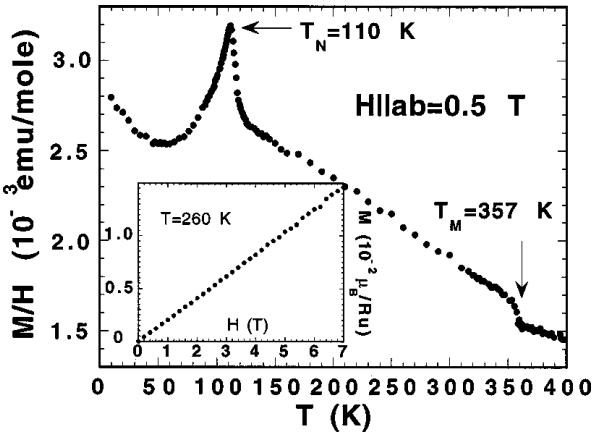


Figure 1.11 Temperature dependence of the magnetic susceptibility defined as M/H for the *ab*-plane in air pressure. Inset: Isothermal magnetization vs magnetic field

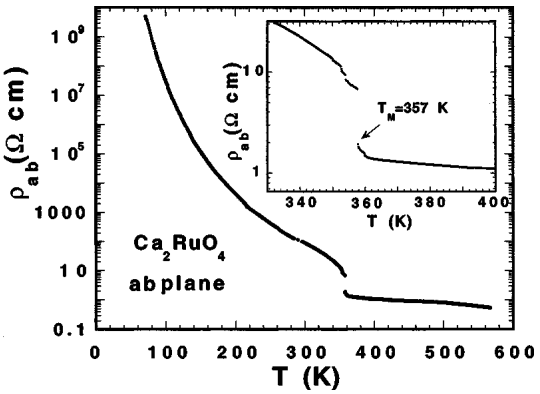


Fig 1.12 Temperature dependence of the electrical resistivity $\rho_{ab}$ in air pressure.
Inset: Detail of the abrupt jump in $\rho$ (T) near the transition $T_{MI}$=357K

When further pressure is induced, it shows the itinerant electron ferromagnetism and exotic superconductor. The anisotropy in magnetization is better illustrated in the angular dependence of magnetization. However, it displays a sharp distinction between the magnetic easy and hard axis. Corresponding to the magnetic anomalies, the resistivity measurement at zero field features two transitions at $T_{MI}$ = 357 K and $T_N$ = 113 K in Fig1.11,1.12[8]. For $B$ // $c$ -axis, the interplane resistivity $\rho_c$ drops abruptly by one order of magnitude, corresponding to the first-order metamagnetic transition.

X-ray diffraction studies reveal a shrinkage of the $c$-axis lattice parameter at under $T_{MI}$= 357 K when heated up, and a few of changes in the $a$ -axis and $b$ -axis lattice are observed. The shortening of the $c$-axis suggests the Jahn Teller effect, which lifts the degeneracy of the $t_{2g}$ orbitals by lowering $d_{xy}$ level relative to $d_{xz}$ and $d_{yz}$ energy levels. As a result, orbital ordering may occur, weakening the mobility of conduction electrons.

## 1.7.5 Pressured phase

It is known that a 4$d$-electron single-layered ruthenates $Sr_2RuO_4$ shows spin-triplet superconductivity below 1.5 K. The isovalent replacement from Sr to Ca change from quasi-2D metal ($Sr_2RuO_4$) to a Mott insulator ($Ca_2RuO_4$). To bridge this gap without introducing disorder, Nakamura et.al have studied the pressure effect upon the 4$d$-electron $Ca_2RuO_4$. This shows the magnetization process of the purresure-induced ferromagnetic and superconducting states in $Ca_2RuO_4$.

Pressurisation to $Ca_2RuO_4$ above 0.5 GPa transforms a Mott insulator with antiferromagnetic ground state to a metal with ferromagnetic ground state, $T_C$ ~10 K. The ferromagnetic state over $P$ = 0.5 GPa has the itinerancy. At $P$ = 2 GPa, it is quantitatively evidenced by the magnetistation process 2 K. The metal-insulator mixed state at 0.5 - $P$ - 2 GPa is the documented case of the magnetic anisotoropy [32].

$T_C$ is maximum ~ 25 K at $P$ = 6 GPa, above $P$ = 6 GPa, $T_C$ goes to the decrease, the pressure phase diagram of this system suggests the existence of a ferromagnetic quantum phase transition at ~10 GPa, the vicinity of ~15 GPa superconductivity. It may be said that $Ca_2RuO_4$ is one of the most suitable systems to study a novel quantum phenomenon in strong correlation with an electron system than these reports.

In the isothermal magnetization measurement, the magnetic state is driven from antiferromagnetic state to ferromagnetic state through a first-order metamagnetic transition upon $P$ = 0.5 GPa. The saturation moment reaches as high as $\mu_B$/Ru for B T, the expected saturation moment (assuming $M_S = 2 \mu_B$/Ru for an S = 1 system)[33]. As more $P$ > 0.5 GPa increases, $T_C$ increases ferromagnetic state remains.

Next mention the pressure phase diagram of $Ca_2RuO_4$, especially the key of the structural transition. First, for the crystal structure that Flatting drawing the *c* axis head is cancelled with a Metal-Insulator metastasis of ~0.5 GPa, it is with L-*Pbca* from S-*Pbca* when I chase an abnormality of the crystal structure looking at the $Ca_2RuO_4$ under pressure in detail. Then, the Tilting of the degree of leaning to the *c* axial direction is cancelled, and the crystal structure becomes an orthorhombic *Bbcm*.

It is predicted that when the Tilting is completely cancelled by pressurization of ~8 GPa (Fig.I-7). Where Rotation is saturated to a constant value by pressurization more than ~5 GPa. $Ca_2RuO_4$ shows various quantum phenomena as showed so far by adding a place outside the element substitution or pressure.

When we look the $Ca_2RuO_4$ under pressure in detail, we chase an abnormality of the crystal structure. At first, Flatting drawing of *c*-axis head is cancelled with metal-insulator transition at ~0.5 GPa. The crystal structure becomes L-*Pbca* from S-*Pbca*. Then, the Tilting of the degree of leaning to the c-axis direction is cancelled and the crystal structure becomes an orthorhombic *Bbcm*.

It is predicted that Tilting can be completely canceled by pressurization of ~8 GPa. Furthermore, Rotation is saturated to a constant value by pressurization more than ~5 GPa (Fig.I-7)[8]. $Ca_2RuO_4$ shows various quantum phenomena, as has been demonstrated so far by adding a place outside element substitution or pressure.

The octahedral start to rotate around the *c* –axis, out of their symmetrical positions and as they are connected to each other by the basal oxygen atoms, neighbouring octahedral start to rotation in the opposite direction which changes their periodicitiy. This means that the *a* and *b*-axis become longer by a factor of $\sqrt{2}$ as the area of their plane is doubled.

The constant Γ value over the metamegnetic transition suggests an A-type antiferromagnetic ordering . This argument agrees with the scattering study and the density functional calculation, both supporting an A-type antiferromagnetism with ferromagnetic order within the plane. This observation is consistent with the fact that the transition itself is a first-order transition, as indicated by the hysteresis in the isothermal magnetization curve.

### 1.7.6 Fundamental Physical Properties of $Ca_{2-x}Sr_xRuO_4$

The Ca series and Sr series exhibit entirely different physical properties. The Sr series is metallic and tends to be ferromagnetic but the Ca series is both insulating and antiferromagnetic. Such features strongly suggest that the properties of this (Ru) series of materials are intimately correlated with the lattice degree of freedom. Because orbit spreads out more than 3*d* electron system as for this series, an orbital effect is thought about with important physics.

A study of $Ca_{2-x}Sr_xRuO_4$ (0-x-2) carried out by Nakatsuji et. al. $Ca_2RuO_4$ can be metalized by two kinds of method; one is filling control is to exchange from Ca ion($Ca^{2+}$) to La ion($La^{3+}$), the other is band width control is although Ca ion ($Ca^{2+}$ = 1.18Å) and Sr ion($Sr^{2+}$ = 1.31Å) are isovalent ions, difference in their ionic size leads to significant difference in structural distortions in Fig 1.13[].

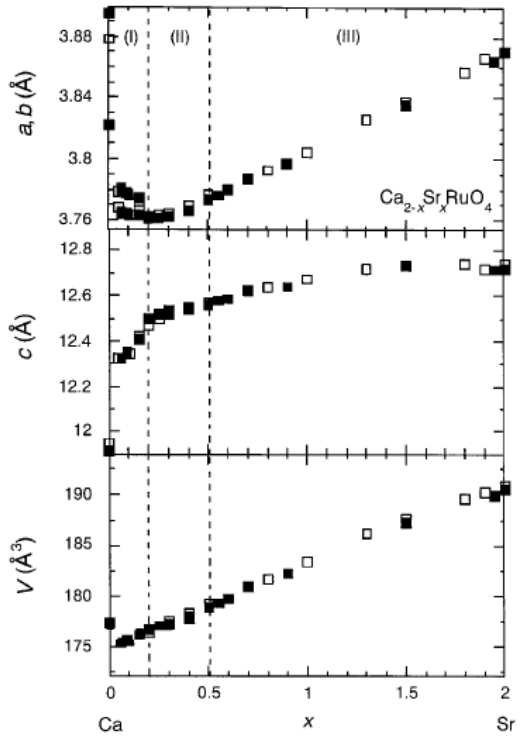


Figure 1.13 $Ca_{2-x}Sr_xRuO_4$ (0-x-2) lattice parameter

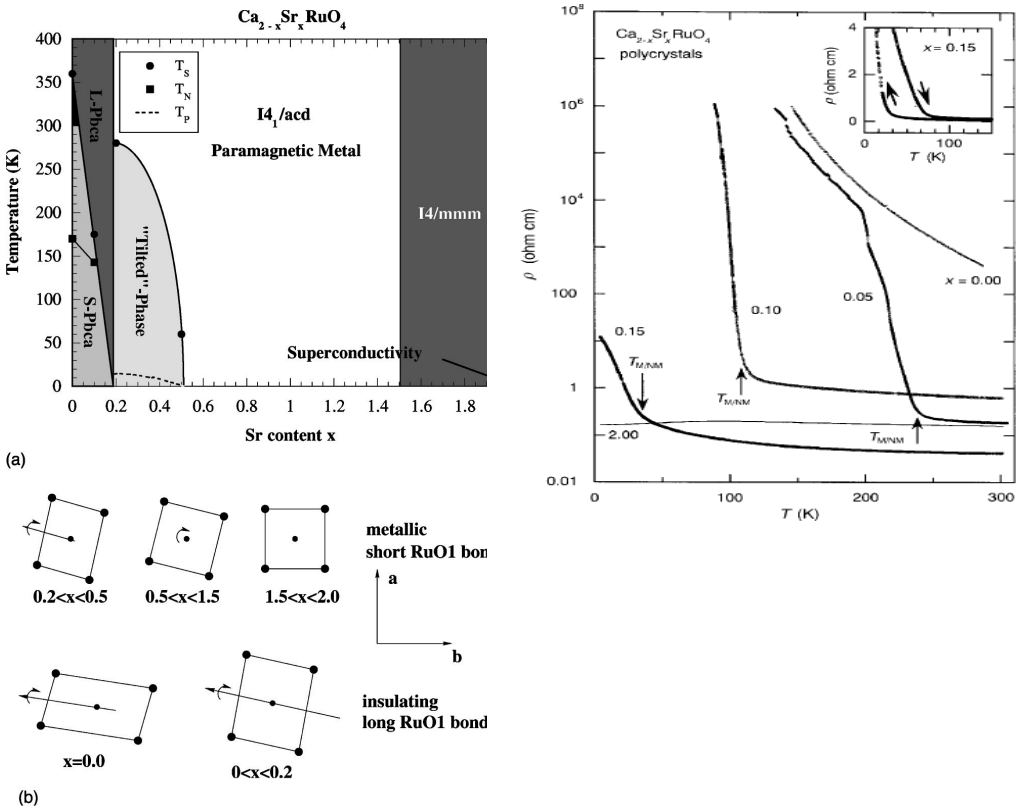


Fig 1.14 Temperature-Sr content x ($Ca_{2-x}Sr_xRuO_4$ ;0-x-2)

The systems $Ca_{2-x}Sr_xRuO_4$, and $Ca_{2-x}La_xRuO_4$ are the layered perovskite system and isostructural to $Ki_2FO_4$. At low temperatures, the area for 0-x-0.2 has a Mott insulator with antiferromagnetic ordering, the area for 0.2-x-0.4 has a metal and that is paramagnetic, the area for 0.4-x-0.7 has cluster glass aspect. The point of x = 2 ($Sr_2RuO_4$) is spin-triplet superconductor $T_C$=1.5 K. At this point, $Ca_{2-x}Sr_xRuO_4$ has multistage phase transition and orbital selective Mott transition shown in 1.14[].

## 1.7.7 Insulator-metal transition of $Ca_2RuO_4$ and relations with the electronic state (Ru 4*d*)

We examine the relation between the structure and electronic properties in single-layered ruthenates. It has been known that the electronic phase stability of $Ca_2RuO_4$ is governed not simply by the effective correlation energy $U/W$, but also by the orbital degeneracy of the $Ru^{4+}$ $t_{2g}$ levels, both of which may abruptly change due to the $RuO_6$-octahedral distortions such as flattening, tilt and rotation [34,35]. In particular, the Mott transition is mainly due to the Jahn-Teller effect that produces a change in the orbital occupation associated with the flattening distortion [36].

4*d* Ru-oxides display versatile quantum phenomena in an external magnetic field. (The integral effect of an external field has yet to be determined?) It does not yet reach so that an effect of the external field is understood integrally. It is not suitable for close parameter control as a technique to add disorder to a crystal in the element substitution in particular. We choose an electric field for the method so it could control the number of the carriers without adding disorder to the material.

From an electronic point of view, the Insulator-Metal transition in $Ca_2RuO_4$ is perceived as the change of the occupation and/or energy levels of the three nearly degenerate Ru 4*d* $t_{2g}$ orbitals ($d_{xy}$, $d_{yz}$, and $d_{zx}$). In the insulator phase, two of four 4*d* electrons occupy the lowest lying $d_{xy}$ orbital due to the rather short *c*-axis in S-*Pbca* phase within the framework of a crystal field model [37,38]. On the other hand, in the metallic phase, the energy level of $d_{xy}$ to $d_{yz}$ / $d_{zx}$ is inverted due to the elongation of the

*c*-axis in L-*Pbca* phase. As a result, a hole is created in $d_{xy}$ state, which leads to the two-dimensional conductivity.

A redistribution of the *d* electrons of such is nicely demonstrated by Mizokawa et, al. on the basis of temperature- and angular-dependent x-ray absorption spectroscopy at the O *K*-edge [39-41]. Taking into account the difference in the angular dependence between the apical O 2*p*-Ru 4*d*-$t_{2g}$ bonding and planar O 2*p*-Ru 4*d*-$t_{2g}$ bonding , the spectral weight-transfer within two $pd\pi^*$ states can be elucidated by the change in the numbers of holes in $d_{xy}$ ($n_{xy}$) and $d_{yz}$ / $d_{zx}$ states ($n_{yz}$ / $n_{zx}$).

The same or similar changes in $n_{xy}$ and $n_{yz}$ / $n_{zx}$ are expected for the Insulator-Metal transition induced by the *E*-field induced. The total electron yield method commonly used for x-ray absorption spectroscopy measurements in soft x-ray region is, however, inapplicable in an electric field-dependent x-ray absorption spectroscopy measurement because of the deflection of electrons.

## Chapter2　Purpose of the Present study

In the present study, we set up the following purposes.

- Insulator-Metal transition under the Electric-field

  To investigate the switching phenomena, voltage-current (V-I) curves have been measured by using two-probe and four-probe method for $Ca_2RuO_4$ single crystals.

- Crystal structure change under the electric field

  In pure $Ca_2RuO_4$, the high-Temperature ($T$ > 357 K) or high-Pressure ($P$ > 0.5 GPa) metallic phase shows the structure called "L-*Pbca*", with a weaker flattening and as well as a weaker tilt and smaller volume than the low-Temperatume ($T$ < 357 K) or low-Pressure ($P$ < 0.5 GPa) insulating phase with the "S-*Pbca*" structure. Thus, it is anticipated that the application of electric field to $Ca_2RuO_4$ is accompanied by the structural distortion to release the "flattening" (by the c-axis expansion). To confirm the electric field induced structural transition, we performed x-ray diffraction measurements for single-crystalline $Ca_2RuO_4$ in $E$ //$c$ at 290 K.

- By x-ray absorption spectroscopy and x-ray emission spectroscopy with electric field induced $Ca_2RuO_4$

  A redistribution of the *d* electrons at the insulator-metal transition accompanied by the structural change is nicely demonstrated by Mizokawa *et al.* on the basis of temperature- and angular- dependent x-ray absorption spectroscopy at the O *K*-edge. We curry out oxygen 1*s* absorption and emission spectroscopy using synchrotron radiation x-ray to know a novel insulator-metal transition induced by an applied electric field in the 4*d*-electron Mott insulator $Ca_2RuO_4$. In order to the spectral weight shifts caused by the field. In this study, we therefore employed the partial fluorescence yield method for x-ray absorption spectroscopy measurements using a soft x-ray spectrometer, which was also applied to observe O *K*-edge x-ray emission spectra [16]. The O *K*-x-ray emission provides information about $pd\pi$ states which are the counterparts of the $pd\pi^*$ states. The complementary

measurements of x-ray absorption spectroscopy and x-ray emission spectroscopy can give an insight into the electrical conducting properties of $Ca_2RuO_4$.

- CRM (Colossal magnetoresistance) under the pressured $Ca_2RuO_4$

  Pressure phase diagram is quite unique and different from that of the substituted system. We reported that pressurization of Ca2RuO4 transforms it from an antiferromagnetic insulator to a quasi-two-dimensional metal with a FM ground state. We have measured in-plane magnetoresistance $\Delta\rho_{ab}/\rho_{ab} = [\rho_{ab}(\mu_0 H) - \rho_{ab}(0)] / \rho_{ab}(0)$ up to 14 T for $Ca_2RuO_4$ pressurized at 2 GPa.

# Chapter3　Experiments

In this chapter, I show the growth method of the $Ca_2RuO_4$ single crystal sample, the Current-Volt characteristic measurement, the x-ray diffraction measurement, the soft x-ray measurement, the setting method of the sample which went originally.

## 3.1　Single crystal synthesis

Here is shown about the growth method of single-crystal $Ca_2RuO_4$. The growth trip greatly separated you and went in the following procedures. Weighting capacity and mixed → first sintering → second sintering → single-crystal upbringing by the Floating Zone method using manufacture [42].

The first, it is to make the polycrystalline ($Ca_2Ru_{1+0.33}O_4$) rod.　The polycrystalline rods for the crystal growth are prepared by a standard soild-state reaction method. To start with, $CaCO_3$ and $RuO_2$ compounds are cooked separately at 600℃ for 12 hours to get rid of moisture.　Then, they are mixed, ground in an agate mortar and cooked at 1300℃ for 12 hours.

$2CaCO_3 + RuO_2 \rightarrow Ca_2RuO_4(\text{polycrystalline}) + 2CO_2$　　(1-1)

To ensure a uniform mixing of these two materials, the mixtures are reground and cooked again at 500℃ for another 10 hours.　After that, the mixtures are filled into a clean cylinder-like rubber balloon and compressed under a pressure.　The compressed rod is then remove from the balloon and sintered at 1000℃ in Ar Gas for another 12 hours. For $Ca_2RuO_4$, $CaCO_3$ and $RuO_2$ mixtures, the ration is Ca : Ru : O = 2 : 1.33 : 4. Because Ru has volatility at a high temperature, that increased $RuO_2$, to use Ru-rich polycrystalline stick here.

$0.33RuO_2 + Ca_2RuO_4 \rightarrow Ca_2Ru_{1.33}O_4 + \delta$　　(1-2)

The raw materials are $CaCO_3$ (99.999% by Rare metallic) and $RuO_2$ (99.9% by Rare metallic). In addition, in $CaCO_3$, Na density was less than 60 ppm, and Fe density used

raw materials of 4 ppm because it was known that a superconducting transition temperature of $Sr_2RuO_4$ decreased by mixture of the Na. Furthermore, the work had rubber gloves to prevent mixture of the Na with the sweat. We do not use the appliances such as metallic medicine spoons such as iron to prevent mixture of Fe in all processes.

### 3.1.1 Floating zone technique

$Ca_2RuO_4$ can also be synthesized by floating zone (FZ) technique using a NEC SC-M15HD-SP image furnace. The furnace is a focus-heating furnace with rotary double ellipsoidal mirrors as illustrated in Fig 3.1,2.

The rods used in the floating zone synthesis are about 4-6 mm in diameter and 4-5 cm in length. The feed rod was hung from the upper shaft using Platinum wire, and the seed rod was fastened to the sample holder on the top of the lower shaft. To start with, tips of the feed rod and seed rod are brought together to the central focal zone, melted and then connected to form a molten zone.

During the growing of the crystal, both the upper and the lower shaft move down inside sealed quartz tube, driving the polycrystalline rod through the central focus zone. The crystallization occurs as the molten zone of the materials move vertically away from the central focal zone. At the end of the growth, the upper rod and the crystallized rod are separated and the system is cooled down. During the growth, both rods are kept rotating.

Single crystals are critical to material study, as they possess the most intrinsic properties of the materials. However, synthesis of single crystals of complex materials has been a deep challenge. In the following, we describe sophisticated procedures developed during the course of our studies on the ruthenates.


Fig 3.1 Floating Zone furnace for growing single crystal

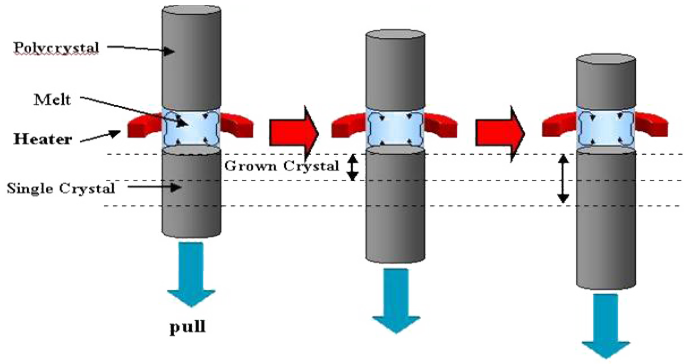


Fig 3.2 Schematic diagram of crystal growth by Floating Zone method

A smooth growth of the crystal is achievable by carefully adjusting the following parameters: pressure of the gas, mixture gas ration, lamp voltage, main shaft speed. Because of volatile $RuO_2$ for temperature above 1100℃ (ref), a Ru-rich feed rod is used instead of a stoichiometric one. The excess $RuO_2$ compensates the loss of $RuO_2$ at high temperature.

In this furnace, each of these ellipsoidal mirrors is equipped with a halogen lamp located at one of the focal points. The infrared rays emitted from the lamps are then reflected by the gold-plated mirrors towards the other focal point, which is arranged to sit at the center of these two mirrors. Generally, with two 1.5kW halogen lamps, the ultimate temperature the apparatus can reach at the central focus zone is around 2050 °C.

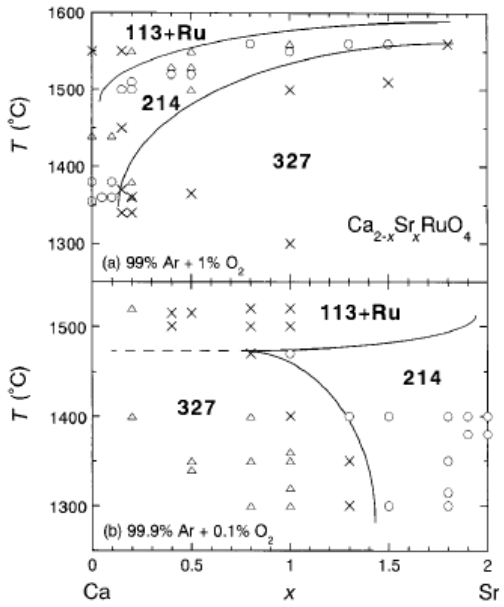


Figure 3.3 Crystal upbringing temperature and composition

The temperature at the central focus point can then be adjusted by tuning the power of the lamps. With a transparent quartz tube, we can manipulate the growing atmosphere, and at the same time observe the growing condition through a camera. The furnace is also equipped with water-cooling system to prevent overheating on the mirrors and the whole system. Composition slips off with a difference of slight temperature in Fig 3.3.

One major advantage of FZ technique is its capability to grow large single crystals, which may not be possible by conventional methods such as flux technique. The diameters of the single crystals that can be grown by FZ technique are limited only by the surface tension of the molten zone [43]. In any atmosphere, crystal growth using the FZ method is in this way possible.

It is advantageous in that impurities do not get mixed because the FZ method does not use a pot unlike the Czochralski methods who is the same fusion method. Usually the crystals can be as large as 60 mg in mass and $4\times3\times1$ mm$^3$ in dimensionality.

In addition, $Ca_2RuO_4$ collects causing structure phase transition with the volume of 5% expansion in 357 K during cooling process, and as for the single crystal stick, it is with a small piece. A plate-shaped crystal with a (001) plane was obtained by self-cleavage. The crystal size to be provided is *ab* plane 1~10 mm$^2$, *c*-axis 0.1~1 mm, mass 1~10 mg degree.

The crystal quality is checked with powder x-ray diffraction measurement and the magnetic susceptibility. We used RINT2000 (by Rigaku) with x-ray diffraction (XRD) measurement. This measured a single-crystal structural change. On the occasion of impurities evaluation, $Ca_2RuO_4$ is opened on a glass plate uniformly by the above into pieces and measured.

We check the lattice constant of crystal and the impurity element. The magnetic susceptibilities of the $Ca_2RuO_4$ are measured using the SQUID (Superconducting Quantum Interference Device) with MPMS (Magnetic Property Measurement System) by Quantum Design. The sample temperature can be precisely controlled from 2 K to 300 K. And a magnetic field as high as 5.5 T is achievable by applying current to superconducting solenoid. From each result of x-ray powder diffraction and magnetization measurement, that the crystals are pure, no detectable foreign phase such as $Ca_3Ru_2O_7$.

## 3.2 Pressured cell

We have two ways of the method to maintain pressure at low temperature and in the magnetic field. One method is that increases weighting from the outside while I change temperature and a magnetic field. Another one method is that beforehand having added pressure at room temperature, and to clamp it for maintain pressured.

The former is cubic-anvil pressure device to change pressure at the time of the measurement. It is large-scale and an experiment is assigned to a limit. On the other hand, we can measure a change of the pressure continually and can always estimate accurate pressure level.

As for the latter is a clamp-type piston cylinder pressure device, it is to pressurize beforehand method. It is possible downsizing and a combination with other measuring equipment. On the other hand, we must examine pressure level with the measurement because a pressure level changes by temperature dependence.

In this measurement, the size of the pressure cell includes a limit to use PPMS (Physical Property Measurement System; sample space is $\varphi$ = 24.5). We used a clamp-type piston cylinder cell. It is made of MP35N alloy compounds and is double structure.

MP35N is nonmagnetic metal and has excellent compressive strength, tensile strength, hardness, noncorrosive, by the alloy including Ni 35%, Co 35%, Cr 20%, Mo 10%. The structure can be realized with higher pressure in the two-layer type. Maximum generated pressure of the pressure cell used in this study is 3.5 GPa at low temperatures.

Pressures were generated with Daphne oil 7243 (Idemitsu Kosan Co., Ltd.) as a Pressure-transmitting medium (ref 2009N-13). We pressurize with the oil-press (Riken seiki Co., Ltd.) in this study and fix it with a piston. I speak below the procedure. (Fig 3.4,1.4)[44]

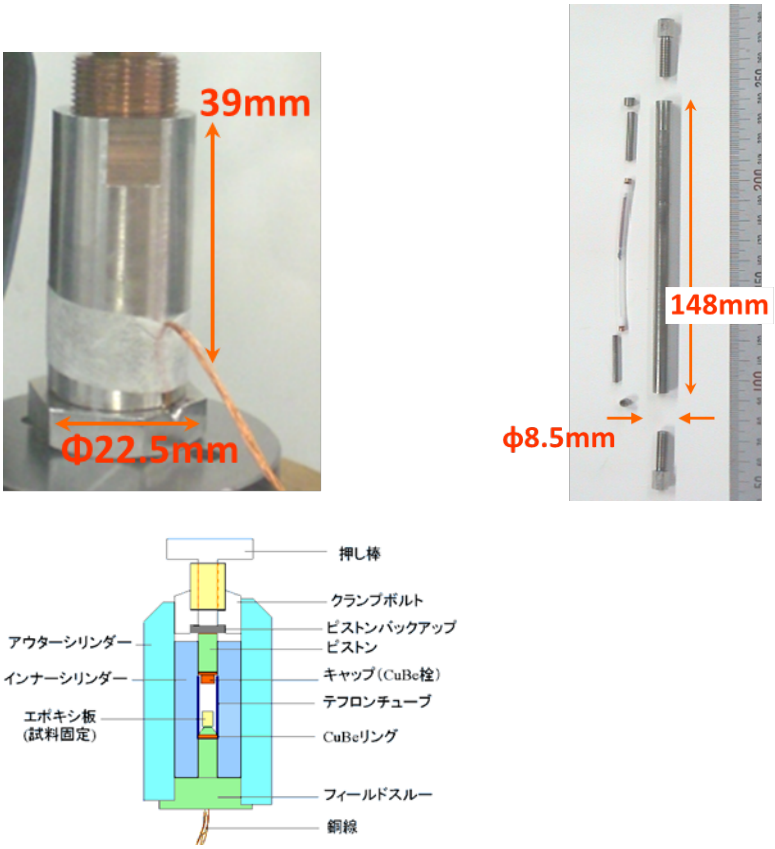


Figure 3.4 Pressure cell for PPMS (left) for MPMS (right)
Schematic view of PPMS cell (under)

*We put a pressure cell on a stand and place a pushing rod for pressurization on piston backup.
*We tied an electrode terminal of sample to LR-700 to pressurize it while measuring a change of the electrical resistance of sample.
*We pushed the pushing rod for pressurization with a press machine. A rod and a press machine are careful to become perpendicular on this occasion.
*The Teflon cell in the pressure cell is pressurized and has a margin shrank. We clamp two bolts as much as was tightened, and maintained pressure.

In this time, we enclosed Daphne oil 7243 as a pressure medium which solidifies in about 3 GPa under room temperature. The electrode terminal is cut and the resting hydraulic pressure characteristics are disturbed when we change pressure as the state that the oil solidified. After it have pressurized, when we changed pressurize once after warming enough the pressure cell with a dryer.

We pressurized until pressure to aim for repeatedly 3 or 4. We can estimate the pressure in the pressure cell at the time of the pressurization from the indication of the press machine. The conversion type is as follows.

$P_{press} \times S_{press} = P_{cell} \times S_{cell}$
$P_{press}$ ; Pressure meter level of the press machine (MPa)
$S_{press}$ ; The area of the cover pressurization part of the press machine (14.52 $mm^2$)
$P_{cell}$ ; Pressure in the pressure cell (GPa)
$S_{cell}$ ; The area of the cover pressurization part of the pressure cell

We can estimate the pressure in the pressure cell as wrote down in a foregoing paragraph, but the true pressure in the pressure cell changes by the total condition of the clamp bolt and the press machine with the value of the pressure meter. In addition, the value of pressure at the low temperature becomes small than the value of pressure at room temperature because the solidified pressure medium under low temperature and high pressure is the volume decreases. The superconducting transition temperature ($T_c$) of lead is changed by the value of pressurization. We measured the interchange susceptibility to estimate pressure $P_{LT}$ at the low temperature with a lead coil and attached outside and inside of the pressure cell.
The conversion type is as follows.

$P_{LT}$ [GPa] = ($T_{c(0)}$ - $T_{c(P)}$)/0.365

$P_{LT}$ ; The value of pressure in the pressure cell at the low temperature

$T_{c(0)}$ ; The superconducting transition temperature of lead under atmospheric pressure

$T_{c(P)}$ ; The superconducting transition temperature of lead under pressure

As for the first-class superconductor such as lead and tin, when a superconducting state is destroyed, the real part of the interchange susceptibility suddenly changes into the conductor at that time gradually give temperature from a superconducting state (or the time of lower temperature from the conductor that it is usual) and the transition temperature. We can identify a transition temperature by this.

We attached a pressure cell to the tip of the cryostat in this study and demand a transition point (temperature) by putting a pressure cell in liquid $He^4$, and measured the interchange susceptibility of lead coil the pressure cell inside and outside. We speak below the procedure.

* We attached a pressure cell to the tip of cryostat and let it glue the thermometer (Carbon Glass Resistance; Model CGR1-1500 by Lake Shore 2-300 K) and an outside lead coil (a coil using copper wire of $\pi$ 37 $\mu$m) together. We took the heat contact using N grease (M&I MATERIALS LTD) to coil and a thermometer of the pressure cell and roll a copper sheet around a pressure cell, so that three temperature of inside lead coil, outside lead coil, the thermometer are same, considered difference of temperature of sample space and the pressure cell outside.
* We attached a pipe of the brass to surround a pressure cell and performed a vacuum pull.
* Because heat conduction of the brass pipe worsened when a vacuum degree was too high, I enclosed He gas after having performed a vacuum pull.
* We connected interchange resistance bridge LR-700 (LINEAR RESEACH CO; frequency is 16 Hz), AVS48, digital voltmeter 2000 and measured some resistance of Sample, inside lead coil, outside lead coil, the thermometer. We measured temperature and the interchange susceptibility at the same time.
* We performed temperature adjustment by regulating the height of the rod.
* We measured the interchange susceptibility about the lead coils in the pressure cell and an outside.

We estimated the value of internal pressure of the cell at the low temperature by these measurements. Because the transition temperature of lead sensitively changed by pressure to understand from an expression in front, we measured in small space neighborhood the transition point to get for more exactly transition point. In addition, it was repeated several times and performed reproducible confirmation.

## 3.3 Pressured resistivity measurement under magnetic field

In this experiment, we used a piston cylinder type pressure cell to hold pressured at room temperature. Where we attached two kinds of samples to make a clear difference to be seen by the difference of the direction to apply of the magnetic field to a sample in the inside of the pressure cell, one is the longitudinal magneto-resistance it is parallel to the magnetic field direction and the current flowing through the sample ($J$//m$_0H$), another is the transverse magneto-resistance it is perpendicular to the magnetic field direction and current flowing through the sample ($J$//m$_0$H) in Fig3.5.

In addition, we have placed the Pb coil (Fig 3.6) used for the determination of applied pressure at low temperatures.

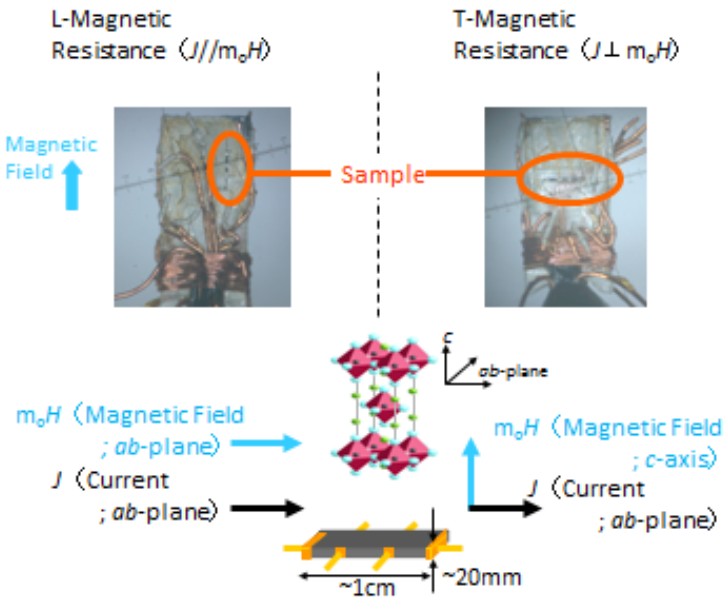


Figure 3.5 Magnetic resistance measurement setting

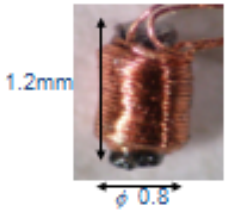


Figure 3.6 Pb coil in Pressure cell

We performed some terminal for electrical resistance measurement. 4 terminals method was used for the measurement of the electrical resistance. But in this study, we attached 6 terminals in consideration of the damage of the terminal with the pressurization. We made gold evaporation in an adhesion side to attach a terminal.

We may not be able to measure the electrical resistance exactly when we attach with the terminal at the upper (bottom) of the missing sample. The reason for the structure of $Ca_2RuO_4$ is the layered and the thickness of a few $\mu$ m, they mounted. Therefore, we performed vapor deposition of the Au on the side of $Ca_2RuO_4$ for the electrical resistance measurement.

In addition, the voltage terminal was connected to the place inside than a one-third or less of the long side, this is because to get a stable electric current. If a terminal is attached towards the edge of side, an electric current becomes easy to be confused.

Au thin-films with sub-micrometers thickness are formed on the fleshly cleaved (001)-surface by using a gold sputtering technique (ULVAC QUICK COATER) at 4 mA for 30 minutes to ensure good contact points. The gold sputtering reached by each three times both the top surface and the base of sample.

We cooled enough $Ca_2RuO_4$ after having evaporate once and the next, because it caused structure phase transition in 375 K and was broken. We measured a size of Sample and position of the gold evaporation to calculate it in specific resistance. Longitudinal resistance ; Voltage terminal (3-4) $S / l = 19.0 \times 10^{-4}$, Voltage terminal (5-6) $S / l = 20.2 \times 10^{-4}$ Transversal resistance ; Voltage terminal (3-4) $S / l = 95.1 \times 10^{-4}$, Voltage terminal (5-6) $S / l = 81.0 \times 10^{-4}$ Unit of credit.

Magnetic-resistance was measured by a standard four-probe method under P up to 4 GPa and fields up to 14 T by using a physical properties measurement system Quantum Design, model PPMS equipped with a homemade nonmagnetic clamp-piston-cylinder cell in fig3.5. We measured two kinds of the longitudinal resistance (J $\perp \mu_0$ H) and

the transversal resistance (J// $\mu_0$H) using AC Transport Mode at the same time.

The magnetic field dependence fixed temperature with 2, 4, 6, 7, 8, 9, 10, 12, 14, 16, 20, 25, 30, 50 K, and we changed magnetic field to 100 Oe/sec in 0~10 T and 50 Oe/sec in 10-14 T. The temperature dependence fixed a magnetic field with 0, 3, 5, 7.5, 10, 14 T, and we changed temperature to 1 K/sec in 2-300 K. Pressured $C_2RuO_4$ has Insulator-Metal (Mott) transition was in approximately 100 K and large change of magnetic-resistance in the low temperature side (less than about 40 K).

We made a small temperature interval of the measurement point around those temperatures. The measurement point at magnetic field 0 T draws hysteresis from a state of zero field cool both temperature-dependence and magnetic-field dependence. Therefore, we compare it with other data, which we do the magnetic field in 0 T after having run the magnetic field of number temperature once (field cool).

Shown in result is the field dependence of the resistivity for the *c*-axis (inter plane) $\rho_c$ for $T$ = 2K and under pressured $P$ = 2 GPa with $B$ // *a*-axis. For the $B$ // *a*-axis (magnetic easy axis), $\rho_c$ shows an abrupt drop by an order of magnitude, corresponding to the first-order metamagnetic transition leading to the spin-polarized of ferromagnetic state with a saturated moment $M_s$ of 1.8 $\mu_B$/Ru or more than 80% polarized spin. For the B // *c*-axis (magnetic hard axis), there is no spinflop transition and the system remains antiferromagnetic. As magnetic field is increased further from 0 to 12 T, $\rho_{ab}$ and $\rho_c$ increases linearly with magnetic field.

The resistivity reduction achieved by this metamagnetic transition can be associated with a tunneling magnetoresistance. Because of the layered nature, the insulating Ca-O plane and the spin-polarized Ru-O planes from the ferromagnetic–insulator-ferromagnetic junction which facilitates coherent motion of the electrons along the *c* -axis. The magnetoresistance mechanism is similar to the traditional magnetic materials like the Fe/Ge/Fe multilayers.

## 3.4 The voltage-current properties measurement at room temperature and low temperature

At first, we measured the voltage-current characteristics by two-point-probe method to estimate the threshold electric field ($E_{th}$) that we checked whether the

insulator-metal transition was induced by an electric field. It is necessary to remove an outside effect as much as possible to find the accurate value of the threshold electric field. Therefore, we speak the experimental method that a measurement circuit and to estimate a threshold electric field.

Next, in the state that held metal by an electric field, we measured the temperature dependence of the electric resistance. It is extremely difficult to lower temperature with holding metal-state. we speak a method to hold metal of $Ca_2RuO_4$ stably, and to lower temperature.

The voltage-current properties were measured by applying standard two-point-probe technique and four-point-probe technique. The transport property measurement is carried out with a TR6143 (The power supply by ADVANTEST). It can carry out Max voltage; 110V, Max current; 2A with ammeter.

When four probes, furthermore, we used a digital volt meter (KEITHLEY 2000). Four-point-probe technique is chosen over a two-point-probe method because four-point-probe technique eliminates the probe resistance, contact resistance. As illustrated circuit diagram in Fig 3.7, two (four) probes are brought into contact with a tested sample at known distance and geometry.

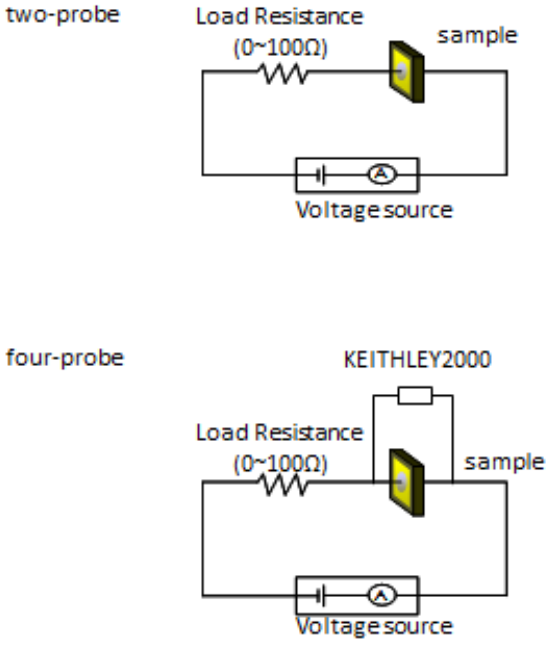


Figure 3.7 Illustrated circuit diagram for 2,4 probe

In addition, it is measurement in the state that we dipped the sample into in insulating oil (Dafney oil 7243) and nitrogen gas. It went to avoid the fever of the sample and the electronic whom-like breakdown by the weak point of the sample surface.

The terminals were performed charge account of the sample like a foregoing paragraph. Gold electrodes were sputtered on both ends of the sample and then twisted gold wires with diameter of 25 $\mu$m were attached to them by silver paste (EMERSON &COMING ECOBOND56C). To make a solid contact between the probe and the sample, silver paste is used as glue to attach lead to the sample.

Since the studied crystals, $C_2RuO_4$ has highly anisotropic and has cleaved surface. We have to special attention for $Ca_2RuO_4$ when putting the leads on the samples. We minded the installation of the electrode (gold evaporation and gold wire). Particularly, the measurement of the *ab* -plane may not measure partial electrical resistance when we attach a terminal (probe) from upper to bottom aspect. Therefore we performed Au vapor deposition on the whole side and did it with a terminal surface for the electrical resistance measurement. The shape of sample is formed that dimension is $d$ ; $1\times10^2$ ~3 $\times10^1$ cm, and square is $S$ ; $5\times10^4$ ~$2^1$ cm$^2$ in Fig 3.8. In single crystal $Ca_2RuO_4$, thickness is very thinly with of dozens $\mu$m for *c*-axis lamellar structure .

Then, we speak how to the temperature-dependent measurement of the electrical resistance in the metal state under electric field. In this study, we measured temperature dependence by letting the rod which I attached a sample for 2 terminals method measurement to go up and down in liquid-He-Dewar. In addition, we used for a thermometer "Cernox-Cx-1050-AA". The thermometer resistance was measured an interchange resistance bridge (AVS-46 by RV companies).

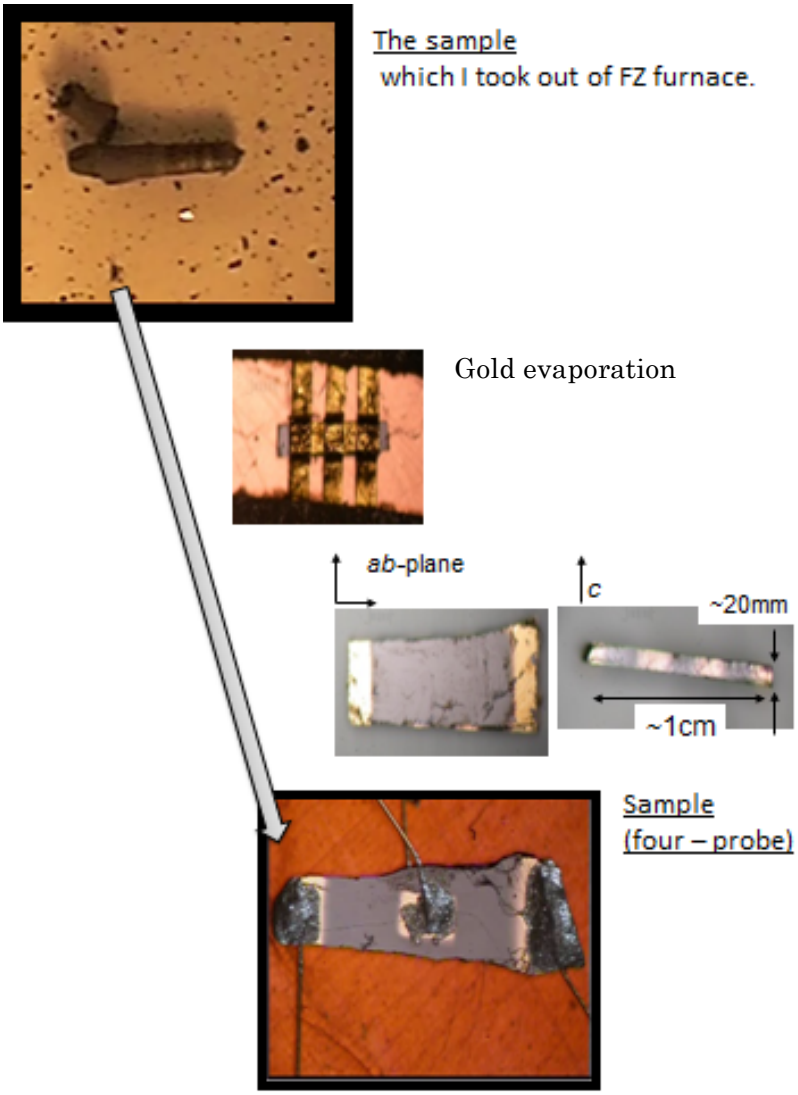


Figure 3.8 Electrode manufacture process

At first, we applied an electric field in a top of He-Dewar, and a sample become metal. Insulator-Metal (Mott) transition comes to have a big threshold electric field in low temperature, and this is to prevent the destruction of the sample by a large electric suddenly current flow when it became metal. After metallization, we lowered temperature at 2 K/min, but electrical resistance increased suddenly and may become unstable. We amplify an electric current with lowered temperature each time while maintain a metal state. After the sample temperature was confirmed at 4.2 K and the electrical resistance was stable, we reached the measurement.

## 3.5 X-ray diffraction measurement

The knowledge of crystalline structure is essential for an understanding of the physical properties of materials. X-ray powder diffraction is one of the methods that have been widely applied in condensed matter physics to study crystalline structure. X-ray is in fact electromagnetic radiation with wavelength around 1 A.

Since that wavelength is comparable with the size of an atom, they are used to explore within crystals. The diffraction pattern of x-ray reveals critical information about the structure of the materials. Positions of the peaks determined by the Bragg law reflect the crystal structure. The combination of peak positions and the intensity is unique for different types of crystal structures.

X-ray diffraction profiles at room temperature were measured with $CuK\alpha$ radiation ( $\lambda$ = 0.1542 nm, 30 mA, 40 kV ) on a RINT2000 diffractometer. The data were collected in a step-scanning mode over the $2\theta$ range of $5^\circ$ -$2\theta$ $-135^\circ$ . The step width and step time are $0.02^\circ$ and 1 sec, respectively. The samples were well ground, and then were put on the glass holder in measurement. The crystal structures of sample were determined by the Rietveld analysis method.

The key procedure that determines the success of this experiment is to find the x-ray diffraction measurement under the electric field. There are three important characteristic points. First point is the sample size and it is the irradiation direction of the x-ray. In this study, x-ray diffraction apparatus used was the originally powder sample measurements.

However, we performed experiments using a single crystal to measure the change in the crystal structure while applying an electric field was essential. Therefore, by using the fact that cleavage plane direction between *c*-axis which is one of the features of $Ca_2RuO_4$, commensurate with the size of the sample holder for powders, and was measured by processing the sample thickness 0.1mm. The measurement is performed in an arrangement utilizing this characteristic it has become possible to measure indicating the *c*-axis length (002) direction. The change in the *c*-axis length of the by chance an important position in the Insulator-Metal transition which that accounting has been reported in studies in external field under such pressure and temperature.

Second is the shape of the terminal. Initially to measure Insulator-Metal transition by an applied electric field in $Ca_2RuO_4$, in order to be applied electric field uniformly to the entire crystal, the shape of the gold deposition to serve as an electrode surface has

been applied widely as possible in the whole of the voltage induced surface of the sample. However, the x-ray diffraction spectrum of the sample cannot be measured gold deposition is overlap in the x-ray irradiation position.

It was devised so as not to perform the gold deposited on the center of the *ab*-plane corresponding to the x-ray irradiation position. As a result, we made a ring-shape (donut-like shape) of the electrode and another is full filmed in fig3.9.

Last point is the fixed method of the sample. The sample with the gold wire was not glued to the glass plate with something varnish like, it is because we did not want to put the effect that prevents to self-distortion from the external environment. In a past study, it was showed so far that $Ca_2RuO_4$ has the change of the lattice parameters to the *a,b*-axis when Insulator-Metal transition under pressured and temperature-dependence.

So we measured of x-ray diffraction under the electric field, the sample of single crystal is keeping flexibility. Fixing neighboring the gold wires to the glass plate without itself fixing to the glass plate by varnish. And, the gold wires are then attached to the probe leads with silver paint. I enabled the x-ray diffraction measurement under the electric field in equally to a sample.

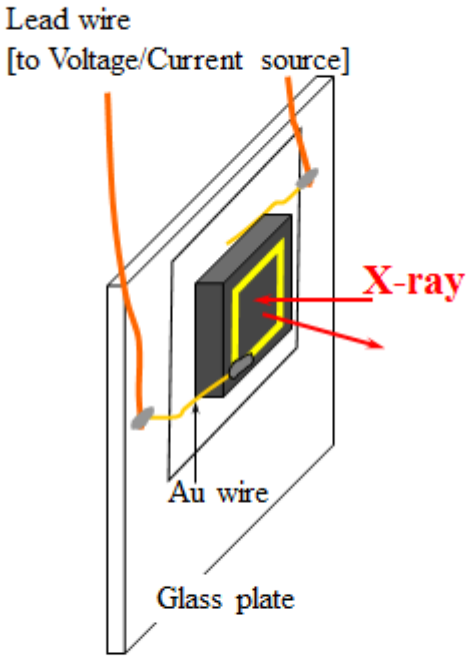


Figure 3.9 Schema of electric field induced single crystal x-ray measurement.

The sample was placed on this center part of the glass plate. We put the single crystal with the terminal on the glass plate for powdery x-ray measurement. The set of the sample performed x–ray measurement at the same time to apply an electric field by an outside power supply. And x-rays irradiated area was se*t* c-axis direction for the structure transition with the metallization of $Ca_2RuO_4$ because the *c*-axis head showed it conspicuously. Cleavage characteristics seemed the *c*-axis in $Ca_2RuO_4$, and a sample was attached to a glass plate to have cleavage planes in the *c*-axis direction.

## 3.6 Soft x-ray measurement

Both x-ray absorption spectroscopy and x-ray emission spectroscopy at the O *K*-edge were measured on the linear undulator beamline 2C at the Photon Factory of the High Energy Accelerator Research Organization (KEK-PF), Japan. Here, a varied line spacing plane grating with an averaged groove density of 1000 lines/mm is used to monochromatize the soft x-ray beam [45]. The beam spot size on the sample was 1 mm in diameter and the energy resolution of the incident photon was ca. 0.1 eV.

The spectrometer used for the partial fluorescence yield method for x-ray absorption spectroscopy and x-ray emission spectroscopy measurements was installed at the end of the beamline [46]. The base pressure of the chamber was on the order of $10^{-6}$ Pa. The angle between the incident and emitted x-rays (scattering angle) was fixed at 90° . The x-ray incident angle during the electric field-dependent measurements was 45° with the polarization vector lying in the *ab* plane. We turned $Ca_2RuO_4$ around at the incident angular dependent spectra.

This is the polarized configuration in which the emitted photon contains the same polarization vector as that of incident photons [47]. The scattered x-rays were monochromatized with a grating that had a groove density of 1200 lines/mm and their energy resolution was ca. 0.5 eV. The O 2*p*-1*s* fluorescence (O *K*) was then collected using a 2-dimensional multichannel detector.

The partial fluorescence yield method for x-ray absorption spectroscopy spectra were obtained by changing the incident photon energy $h\nu$ from 522 to 565 eV, while the x-ray emission spectroscopy spectra were obtained with $h\nu$ fixed at 536.1 eV. It should be noted that the relation between the polarization vector of the incident photon and the crystal axes is more important rather than the configuration of the polarization in our study.

The angular dependent spectra were collected with polarized and depolarized configurations. X-ray absorption spectroscopy and x-ray emission spectroscopy spectra taken for the incident angular $\theta$ varying between 20° and 60° , $\theta$ is the angle between the surface parallel and the incident x-ray beam. The incidence angle of the soft x-ray was about 30-70° to avoid the self-absorption effect. The x-ray absorption spectroscopy and x-ray emission spectroscopy were measured at "depolarized" and "polarized" configurations.

When the x-ray absorption spectroscopy was measured in the depolarized configuration, the polarization vector of the emitted photon rotates by 90° from the polarization vector of the incident photon. On the other hand, when the x-ray absorption spectroscopy was measured in the polarized configuration, the polarization vector of the emitted photon contains the same polarization vector as that of the incident photon.

The sample holder of applied electric field was connected the two blocks of cupper, highly insulated alumina, and played the role of the electrode with performing at a fixed sample.

### 3.6.1 Sample evaluation of the on site

The voltage-current (V-I) characteristics were measured *in situ* during the spectroscopic measurements with a two-probe method using a DC voltage-current source/monitor (ADVANTEST, TR6143). A 100 Ω load resistance was connected in series to prevent short-circuit damage at the Insulator-Metal transition. The electric field was applied parallel to the *ab* plane. For each Voltage-Current (VI) condition, approximately 1.5 hours were required to obtain one set of x-ray absorption spectroscopy and x-ray emission spectroscopy spectra, and therefore, the current-control mode was used to ensure long-term stabilization.

# Chapter4　Result and Discussion

In this chapter, I report a result of $Ca_2RuO_4$

・Impurities evaluation of the sample

・Magnetic resistance measurement under the pressure

・Voltage-Current properties under the electric field in room temperature

・Lattice parameter under the electric field by x-ray diffraction measurement

・Electric state under the electric field by soft x-ray absorption and emission measurement

## 4.1　Sample evaluation

In the single crystal of $Ca_2RuO_4$ by the Florting-Zone method, $Ca_3Ru_2O_7$ is generated at the same time and may become the impurity. The sample was confirmed by the magnetic measurement and the powder x-ray diffraction measurement which is not included in impurities ($Ca_3Ru_2O_7$, Ru *et al.*).　We show the powder x-ray diffraction measurement in fig4.1.

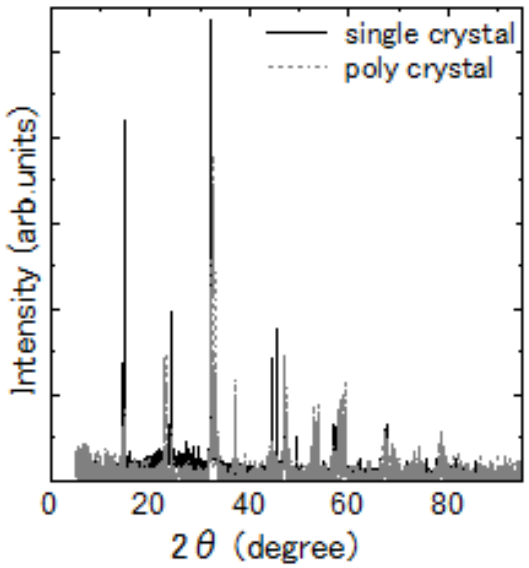


Figure 4.1 The powder x-ray diffraction in $Ca_2RuO_4$

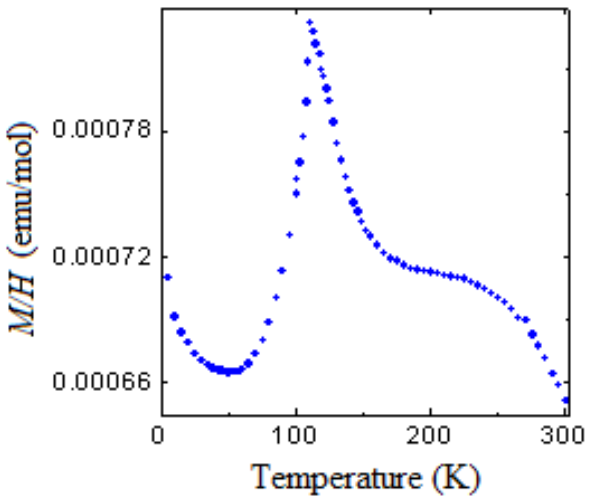


Figure 4.2　Magnetic susceptibility

We also confirmed a single phase of $Ca_2RuO_4$ from powdered crystals. Using an orthorhombic symmetry with space group *Pbca*, we are able to estimate the crystalline lattices to be $a$ =5.41Å, $b$ =5.50Å and $c$ =11.94Å. We notice that the impurity phase such as $Ca_3Ru_2O_7$ is not absent in the diffraction patterns.

We show the temperature dependence of magnetic susceptibility from 2 to 300 K in fig 4.2. No data of magnetic phase had been shown. To compere this sample and to have been showed, we do not have impurity, it is small so as to be able to ignore it. It is cleared that the sample is pure by $\rho_0$~3 $\mu\Omega$cm in the metallic state at high pressures.

## 4.2　Pressured resistivity of $Ca_2RuO_4$ under the magnetic field

In contrast, pressure ($P$), phase diagram is quite unique and different from that of the substituted system. It is reported that the $Ca_2RuO_4$ is transformed to a quasi-two-dimensional metal with a ferromagnetic ground state from antiferromagnetic Mott insulator by pressurization at 0.5 GPa. We have measured in-plane magnetoresistance $MR_{ab/ab}$ is up to 14 T.

The longitudinal $MR_L$-MR : $J_0H_c$ and the transverse $MR_T$-MR : $J_0H_c$ at several fixed temperatures between 50 and 2 K are plotted against magnetic fields. Respectively. Application of magnetic field up to 14 T enlarges the longitudinal- magnetoresistance negatively and monotonically over the whole temperature range we measured. The longitudinal resistance (J $\perp \mu_0$ H) and the transversal resistance (J// $\mu_0$H).

On heating from 2 K, the amplitude of the negative longitudinal- magnetoresistance continues to rise from 7% at 2 K and 14 T, reaching a maximum of 55% at 10 K of $T_C$, then it turns to decrease. Moreover, the negative longitudinal- magnetoresistance curve turns from concave to convex one in the vicinity of $T_C$ 10 K. It can, thus, be seen that the negative magnetoresistance effect becomes remarkable at $T_C$.

On the contrary, the magnetic field variation in the transversal- magnetoresistance is mainly positive but relatively complicated magnetic field and temperature variations. At 2 K, the transversal- magnetoresistance rises positively and monotonically, peaking at the maximum of +120% in 9.7 T, and then it turns to reduce. We note that the value of +120% at 2 K and 1.9 GPa is the largest effect in the temperature and pressure ranges we measured in Fig 4.3.

Such a large magnetoresistance is actually rare among positive than negative effect. With temperature, however, the amplitude of the positive the transversal- magnetoresistance reduces, and then the sign turns from positive to negative in the vicinity of $T_C$. Above 30 K the amplitude becomes quite small, similar to the longitudinal- magnetoresistance. The characteristic peaks were observed at magnetic fields of 9.7, 9.4, 8.9, 8.6, 8.4, and 7.4 T for $T$ = 2, 4, 6, 7, 8, and 10 K, respectively.

Thus, the peak decreases gradually and vanishes suddenly above 10 K of $T_C$. Thus, the peak nature is most probably related to the ferromagnetic ordering. In order to display the complicated magnetoresistance nature intelligibly, the changes of longitudinal- magnetoresistance and transversal- magnetoresistance at 3 T are plotted as a function of transversal- magnetoresistance.

With reducing temperature from 50 K, the longitudinal- magnetoresistance enlarges negatively, reaching a peak of 30% in the vicinity of $T_C$ = 10 K, then it decreases rapidly toward zero at absolute zero. Qualitatively similar magnetic field and temperature variations in longitudinal- magnetoresistance can be seen in a typical ferromagnetic metal such as nickel in the vicinity of $T_C$. This behavior is interpreted in terms of a change in the ferromagnetic spin fluctuation, which is suppressed in the vicinity of $T_C$ with magnetic fields.

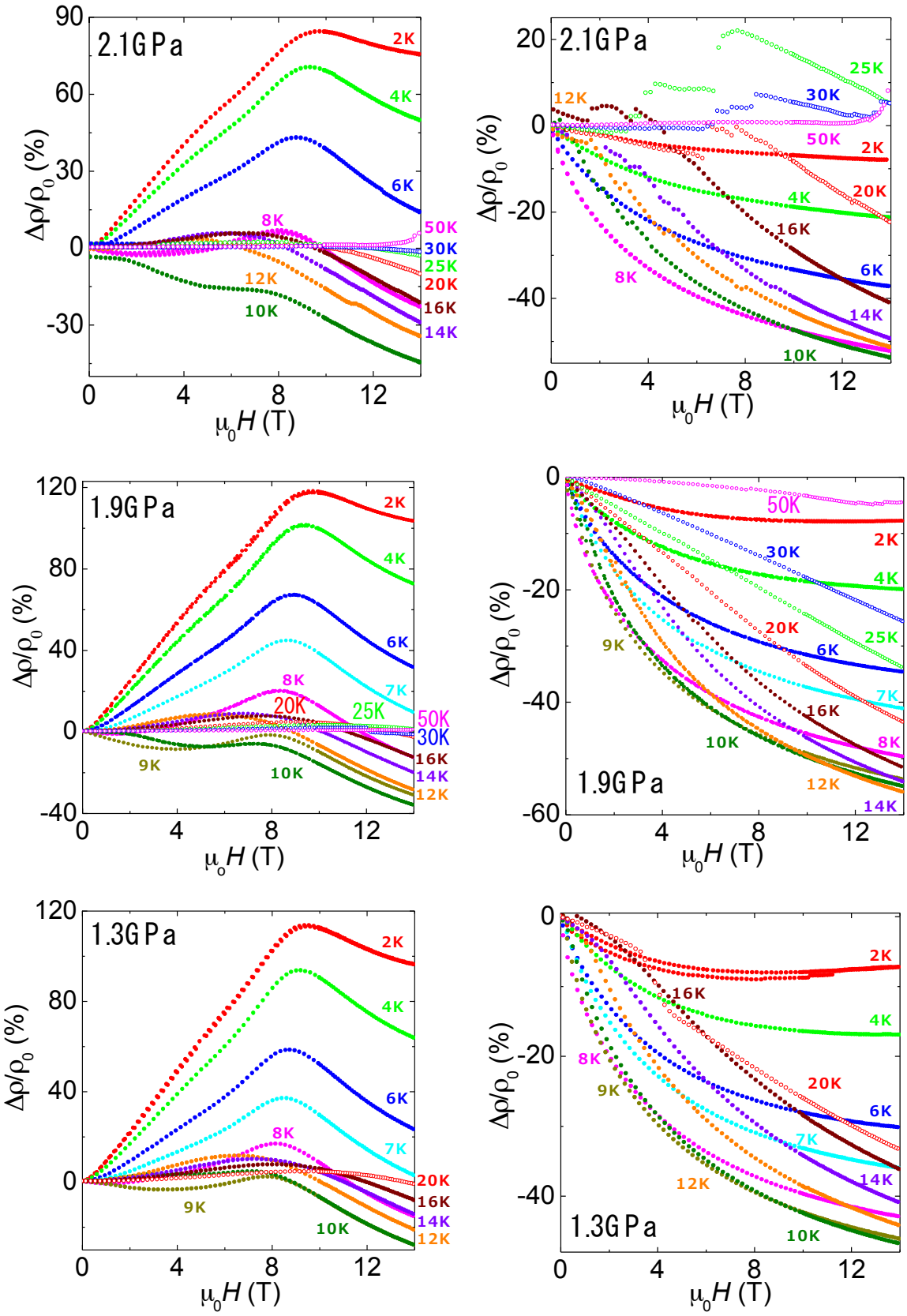


Figure 4.3 Magnetic resistance under pressure

(Left; transversal- magnetoresistance Right; longitudinal - magnetoresistance)

We can, therefore, understand the observed nature of longitudinal - magnetoresistance as a typical ferromagnetic behavior near $T_C$. In contrast, the transversal- magnetoresistance nature, especially T dependence, remains puzzling. On cooling from 50 K, the transversal- magnetoresistance increasing positively and weakly dips suddenly into the negative value of 8% on the border of $T_C$ . Below $T_C$ it rises again toward 40% at 2 K.

On the analogy of magnetoresistance of nickel, the negative dip at $T_C$ appears naturally in both colossal magnetoresistance and longitudinal- magnetoresistance. That is, the dip in the transversal- magnetoresistance is most likely due to the same origin as seen in the longitudinal- magnetoresistance. It is generally known that a resistance caused by magnetic scattering obeys the Matthiessen rule; therefore, the transversal-magnetoresistance excluding the ferromagnetic fluctuation effect is obtained after subtraction of the longitudinal-magnetoresistance from the observed transversal-magnetoresistance,

### 4.2.1 Collosal Magnetic Resistance

Collosal magnetic resistance is let us consider the reason why application of $H_C$ only causes the characteristic changes in the resistivity. We infer that the characteristic magnetoresistance nature is due to a change in the magnetization, namely, the magnetic scattering. Indeed, the characteristic magnetoresistance has mainly been observed in the ferromagnetic state only.

Recently we show that the ferromagnetic moment is strongly anisotropic; that is, the *c* axis is the hard direction. A comparison of the anisotropic magnetization processes at 2 K and 1.8 GPa gives us $H_A$ 9.5 T of the anisotropy field, at which the direction of the spin orientation is forced from the *a*-axis to the *c* -axis by applying $H_c$. Here we note that $H_A$ 9.5 T corresponds to the peak field of the transversal- magnetoresistance.

Indeed, a change in magnetoresistance at 0 $H_A$ has often been reported as a characteristic nature of a ferromagnet. That is, a rotation of ferromagnetic moment is known as a factor for a change in magnetoresistance. In our transversal - magnetoresistance case, the current and fields are applied perpendicular and parallel to the hard direction of the *c* axis, respectively.

With applying $H_A$, the angle between the magnetized and the current directions initially increases, then it becomes a right angle above $H_A$. At $H_A$, such a change in magnetization is naturally reflected in the transversal - magnetoresistance. In contrast, the longitudinal- magnetoresistance shows no characteristic change because the application of $H_C$ induces no characteristic change in the ferromagnetic moment.

It, thus, can be seen that the anisotropic magnetoresistance is interpreted in terms of anisotropic magnetization, namely, spin flop induced by fields applied to the hard direction of c However, there remains a question why the transversal - magnetoresistance shows positive and giant magnetoresistance effect. We can fully expect that our finding of the positive and giant magnetoresistance effect is interpreted in terms of the tunnel magnetoresistance effect although there is no direct evidence to confirm this so far.

It is known that the tunnel magnetoresistance effect, which can often cause a large and positive magnetoresistance, occurs in magnetic tunnel junctions consisting of ferromagnet isolated by thin insulators. Electron tunneling between the isolated ferromagnetic islands can occur in the case that the insulating layer is thin enough. Moreover, an angle dependence of magnetoresistance is known as a characteristic behavior of the tunnel magnetoresistance.

In the pressurized $Ca_2RuO_4$, the ferromgnetic metallic phase is induced and enlarged by pressurizing above 0.5 GPa, then it is dominant above 1.5 GPa. Indeed, the linear extrapolation of pressuring the S-*Pbca* volume fraction vs Pressure suggests that the S-*Pbca* insulating phase is almost killed by $P$=1.5 GPa. Moreover, pressurization above 1.5 GPa kills TN and makes it possible to reach the remnant ferromagnetic moment as a bulk system the ferromagnetic moment is almost constant above 1.6 GPa, as indicated by our magnetization 10 and SR studies.

However, the resistivity still shows a nonmetallic T dependence even above 1.5 GPa. These mean that there exist many of the ferromagnetic metallic islands separated by the thin insulating layers in the mixed state. Moreover, we can fully expect that the magnetic tunnel junctions be naturally formed in the mixed state.

As shown in Fig 4.3, magnetic resistance under 1.3,1.9.2.1GPa, with pressurizing above 0.5 GPa the positive and giant magnetoresistance effect is initially enlarged, reaching a maximum value of +120% at 1.9 GPa, then reduces rapidly and vanishes in the metallic state above 2.3 GPa. Thus, the positive magnetoresistance effect is characteristic of in the mixed state. We, therefore, infer that the positive magnetoresistance is due to the tunnel magnetoresistance effect, namely the tunnel

junctions consisting of the ferromagnetic metallic islands L-*Pbca* isolated each other by the thin insulating layers S-*Pbca*.

The tunnel magnetoresistance effect is actually a strong candidate for the mechanism of the peculiar magnetoresistance in the mixed state, but it is not enough for full understanding of our observed magnetoresistance effect. As another factor enlarging magnetoresistance, we should discuss the [orbital physics], which is proposed to understand the peculiar properties of Ru214 in the vicinity of Mott transition, specially the [orbital-selective Mott transition]. We focus on two evidences indicating importance of strong coupling with spin, charge, and the orbital degrees of freedom.

First, we pay attention to the value of $H_A$, which is known as an indication of spin-orbit coupling. $H_A$ = 9.5 T is one of the largest values as a *d* electron ferromagnet. Even for a typical anisotropic ferromagnet of Co with $H_A$ = 1 T, the orbital angular momentum plays a key role to understand the strong magnetic anisotropy. Thus, importance of the orbital physics is demonstrated by the strongly anisotropic ferromagnetism of the pressurized $Ca_2RuO_4$.

Second, we note that the large negative magnetoresistance is not limited in the mixed state. The negative longitudinal-magnetoresistance reaching 50% have been observed in the paramagnetic region above $T_C$ and the metallic state above 2.3 GPa. It is known that magnetoresistance in 3*d* ferromagnetic metals shows the qualitatively similar temperature and magnetic-field dependences, especially negative dip in the vicinity of $T_C$ although the amplitude of magnetoresistance is a few percent at the most.

The amplitude of the magnetoresistance in $Ca_2RuO_4$ is too large to explain in terms of simple magnetic scattering as is the case with 3*d* ferromagnetic metals. We deduce that the orbital physics, namely strong spin-orbit coupling, amplifies the magnetoresistance due to magnetic scattering.

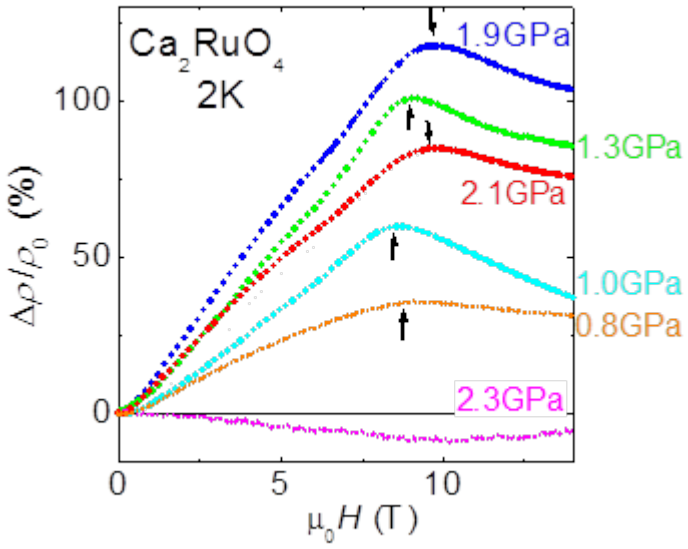


Figure 4.4 Transverse magneto resistance of each pressure in 2K

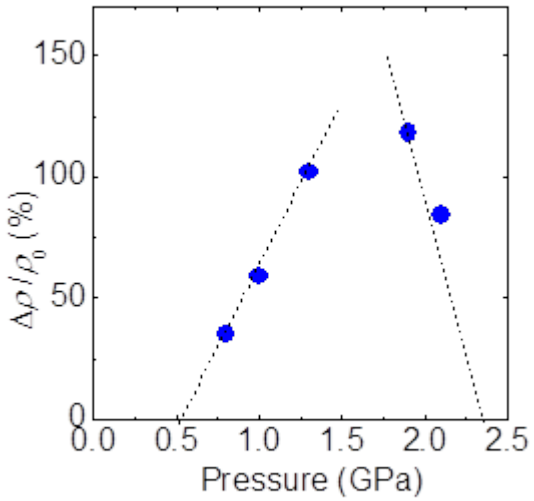


Fig 4.5 pressure dependence (MAX[2K,9.7T] of transverse magneto resistance)

I settled pressure dependence of the magneto resistance in Fig4.4,4.5. It is thought that a peak of the equilateral wide reluctance may become maximum in 1.7~1.8GPa.

### 4.2.2 Temperature dependence of magnetic resistance

It is shown the temperature dependence in each magnetic field such as 3, 5, 7.5, 10,14 $T$ under the pressure of 1.9 GPa in Fig4.6. When the value of the longitudinal magnetic-resistance lets temperature descend, it is decreases equally towards $T_C$. After having taken the minimum in $T_C$, it is increases immediately.

The change volume of transverse magneto-resistance is small wide temperature drop. I decline that a rise is $T_C$ afterwards and slightly from $T_C$ takes the minimum in a high temperature side and it is less than $T_C$ and suddenly rises. It rises in the slightly high temperature side from $T_C$, further declines afterwards to take the minimum in $T_C$. It is suddenly rises at less than $T_C$. In temperature dependence, as big difference with the measurement in magnetic field dependence, it makes a peak towards $T_C$ with the longitudinal and transverse magneto-resistance.

I show difference of the longitudinal and transverse magneto-resistance in Fig4.7. The sharp peak is disappear near $T_C$. Magnetic resistance is increases to go to low temperature. It shows the max value under 10 T at 2 K. Compare with magnetic field dependence, it is compatible with the transverse magneto resistance at 8 ~ 10 T.

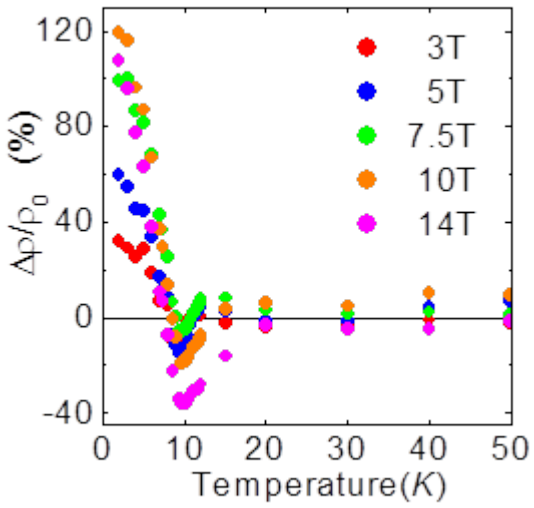


Figure 4.6 Temperature dependence in each magnetic field

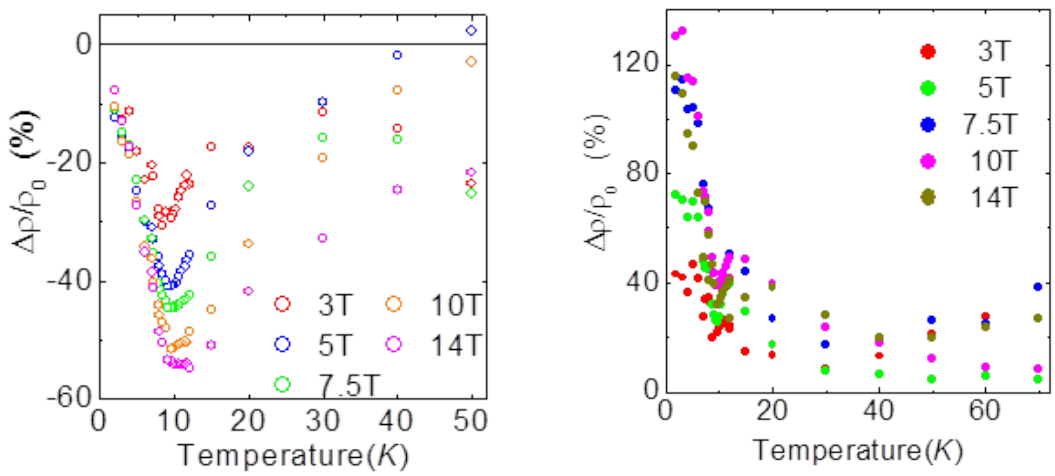


Fig 4.7 Magnetic resistance of temperature dependence at 1.9 GPa
(left) The transverse magneto resistance (right) The longitudinal magneto resistance (at 3, 5, 7.5, 10, 14 T)

### 4.2.3 Compare with magnetic resistance and magnetic susceptibility

In Fig4.8, (I) A magnetization curve to apply below magnetic field to *a* -axis and *c* -axis at 1.8 GPa in 2 K (II) Magnetic field dependence longitudinal and transverse magneto resistance at 1.9 GPa in 2 K. From magnetization curve (I), I made clear that *a* -axis is easy magnetization axis, *c* -axis is hard magnetization axis in $Ca_2RuO_4$. I determined the anisotropic magnetic field at 9.5 T by the point that accords of the magnetic susceptibility of easy magnetization axis and hard magnetization axis magnetic. A value of the anisotropic magnetic field (9.5 T) accords with the peak of transverse magneto resistance field (9.7 T).

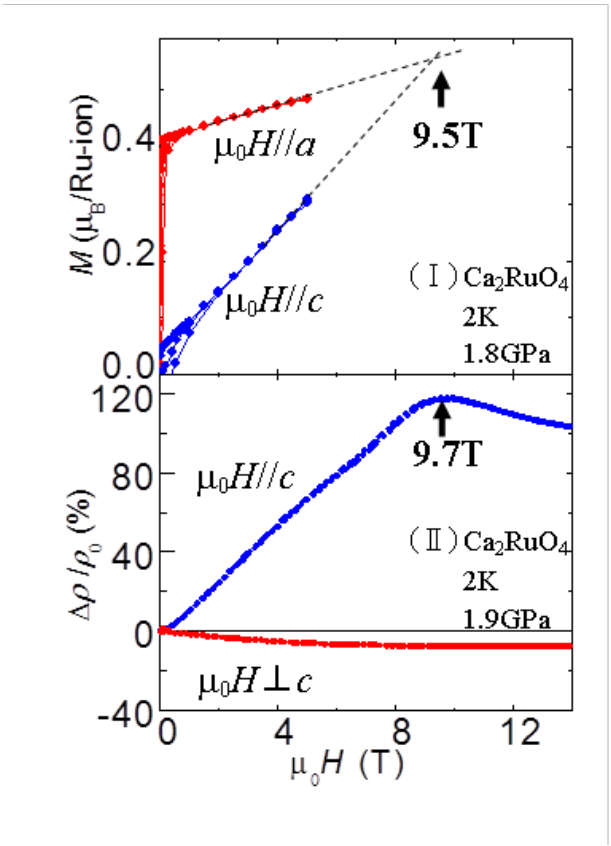


Fig 4.8（Ⅰ）Magnetic curve (at 2K)
（Ⅱ）Magnetic resistance (magnetic field dependence at 2K)

The anisotropic magnetic field under the pressure of 1.9 GPa of $Ca_2RuO_4$ was identified as 9.5 T as demanded. This anisotropic magnetic field understands the thing that is remarkably bigger than other materials in Table 4.1. The anisotropic energy can be demanded using this anisotropic magnetic field and value of the natural magnetization of the magnetization easy axis.

| Anisotropic magnetic field (T) | |
|---|---|
| $Ca_2RuO_4$ | 9.5 |
| Co | 1.04 |
| Fe | 0.049 |

Table 4.1　Anisotropic magnetic field

An anisotropic magnetic field showed 9.5T (a very big thing) and assumed anisotropic energy 100kJ/m$^3$ in 3-3 and 4. It is show the anisotropic energy of a representative material in Table4-1. The anisotropic energy has the enough size that it ignores in comparison with other materials. It is understood that there is magnetic anisotropy.

The Ru is 4*d* electron system, and it is reported to $Ca_2RuO_4$ oneself so far that a journey is ferromagnetic. Judging from these two points, there cannot be the magnetic anisotropy. We were able to show magnetic anisotropy with clear size in this study so much. It is very rare, the consideration is necessary that included the new concept such as the orbital effect, mott transition, strong correlation electron system. It has not yet understood it, but will be the fact that is interesting as understanding to a new material in future.

## 4.3 The effect under the electric field

Fig4.9 shows changes in Current at 295 K as a function of Voltage. With increasing Voltage along the *c* -axis, Current first rises linearly at a rate indicating nonmetallic conduction of ~60 Ωcm, but then jumps discontinuously from 18 to 700 mA at 0.8 V, indicating switching, and is followed by an increase at a rate indicating metallic conduction of ~0.4 Ωcm. Surprisingly, the threshold value $E_{th}$ ~ 40 V/cm for $E // c$ is far smaller than our expectation of ~ 4 MV/cm. We typically obtained $E_{th}$ ~ 50 V/cm for $E \perp c$. Thus, the value of the $E_{th}$ is almost independent of the electric field direction.

With reducing Voltage, Current decreases with the metallic slope. However, Current vanishes abruptly at ~ 10 V/cm because the sample breaks into pieces (single crystalline $Ca_2RuO_4$ disintegrates not in the process of the insulator-to-metal transition but in the metal-to-insulator transition. Thus, the electric field induced disintegration occurs only in the decreasing voltage process at $E < E_{th}$). Until this disintegration occurs, the Voltage-Current curves show a large hysteresis indicating a first order Mott transition [34,35] during voltage sweeps.

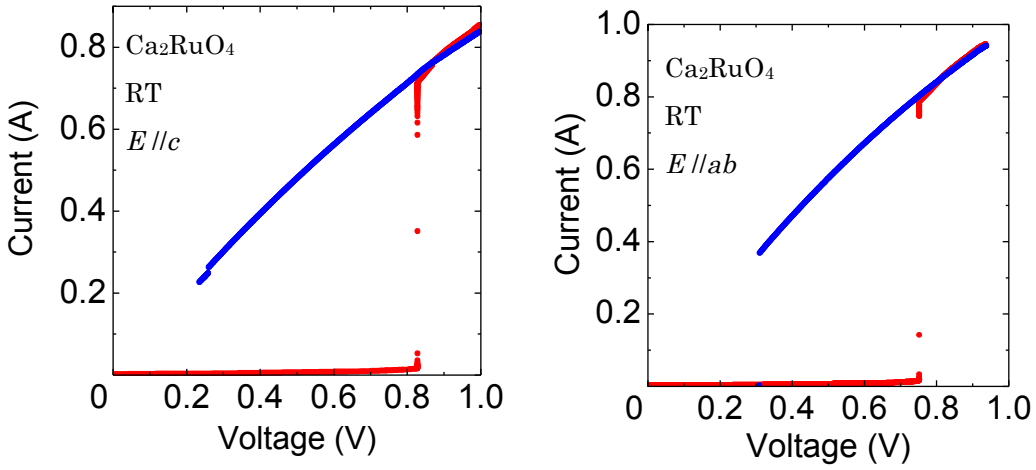


Figure 4.9 Voltage-Current characteristics were measured two-probe method and voltage-control. (left) *E*//*c* (right) *E*//*ab*

This value is very low number by comparison that other Mott insulators show $E_{th}$ is kV/cm~ MV/cm order. In addition, $V_{th}$ shows a dry-cell battery voltage, it mean that $Ca_2RuO_4$ could be applicable to a low power consumption device.

It should be noted that Joule heat generated at the sample is rather diminishing due to the rapid decrease of the sample resistance in $Ca_2RuO_4$. The sample temperature has to be stabilized at same temperature with the air. The electric field induced is slow enough to allow the sample temperature to become uniform yet fast enough to lose heat from the single crystal sample to the heat bath.

The Experiment reached in the helium gas and oil and air. As for the "dielectric breakdown" to happen in a low electric field, there are usually many "snow slide" phenomena to produce with non-homogeneity such as impurities or the surface. However, it is thought that there is not the "dielectric breakdown" (Insulator-Metal transition) of $Ca_2RuO_4$ by the electric discharge phenomenon by superficial "snow slide" and impurities, even if we think in conjunction with high purity in the sample evaluation.

The argument about the Joule heat performed by the experiment of the direct observation experiment using the radiation thermometer and to attach a thermometer to in the case of applying it went the electric field by the cooperation of the Yamagishi *et al.*[48]. As a result, it is reported that the "dielectric breakdown" (Insulator-Metal transition) by the electric field is not a thing due to a temperature rise (heat

phenomenon).

Voltage-current characteristics were measured with a four-probe method in Fig 4.10. As a result, where $V_{th}$ showed the value that was lower than the measurement of two-probe method in Fig 4.9. In addition, the voltage-current characteristic after the metal phase showed the linear nature. Next, we show voltage-current characteristic by current control method in Fig 4.11.

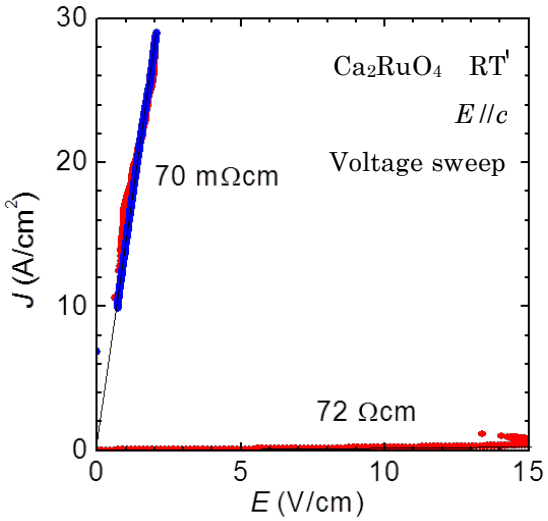


Figure 4.10 Voltage-current characteristics were measured with a four-probe method

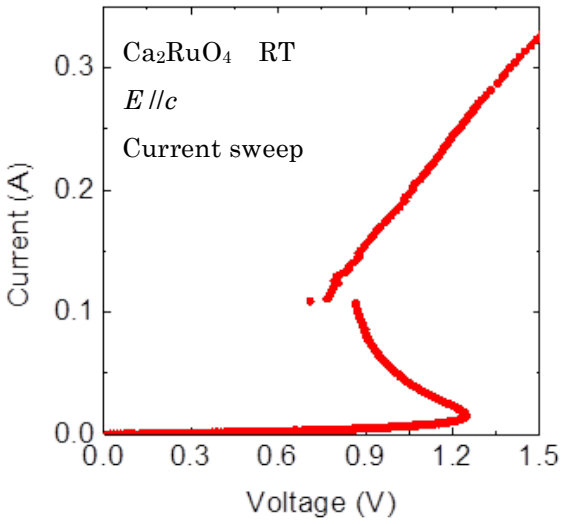


Figure 4.11 Voltage-Current characteristic by current sweep method

Current sweeps method shows a equivalent $V_{th}$ with Volatege sweeps method, it shows Negative Differential Resistance. Negative Differential Resistance is generally observed when a dielectric breakdown happened for an electrode perpendicularly (e.g., into a filament form).

Negative Differential Resistance could be observed when the electric field induced both of *ab* -plane and *c* -axis. This suggests that it is a characteristic as the whole $Ca_2RuO_4$, it is not the special phenomenon of the direction in the cleavage planes.

We show that simple Joule heating is negligible from the following three pieces of experimental evidence: Firstly, there was no appreciable change in temperature of the sample during voltage sweeps; secondly, the switching is also induced by applying only one tiny electric pulse such as $V_{th} \sim 6$ V and $I \sim 20$ mA for the duration of 100 ms. In this switching, the total power of ~12 mJ is fed into a sample in contact with a heat bath. Even if the sample absorbs all the heat, the possible temperature rise of the sample (2.5 mg) is less than ~ 7 K. Thus, the actual temperature should remain much less than $T_{MIT}$ = 357 K.

Lastly, the voltage current curves obtained for different duration time are shown in Fig 4.12(left) in order to characterize the amount of heat needed to induce switching. Total heating $Q_{th}$ at a threshold point is plotted as a function of the duration time in Fig 4.12(right). $Q_{th}$ rises almost linearly with the duration time, in sharp contrast to constant $Q_{th}$ expected for a heating-dominated case. Thus, our switching phenomena cannot be interpreted in terms of a Joule heating.

Total heating $Q_{th}$ at the switching threshold estimated by $Q_{th} = \oint V_{th}(t)\, I_{th}(t)\, dt$ in an adiabatic model plotted as a function of duration time. The almost linear increase of $Q_{th}$ with duration time gives clear evidence that the switching is not dominated by heating. The solid line is guide for the eye.

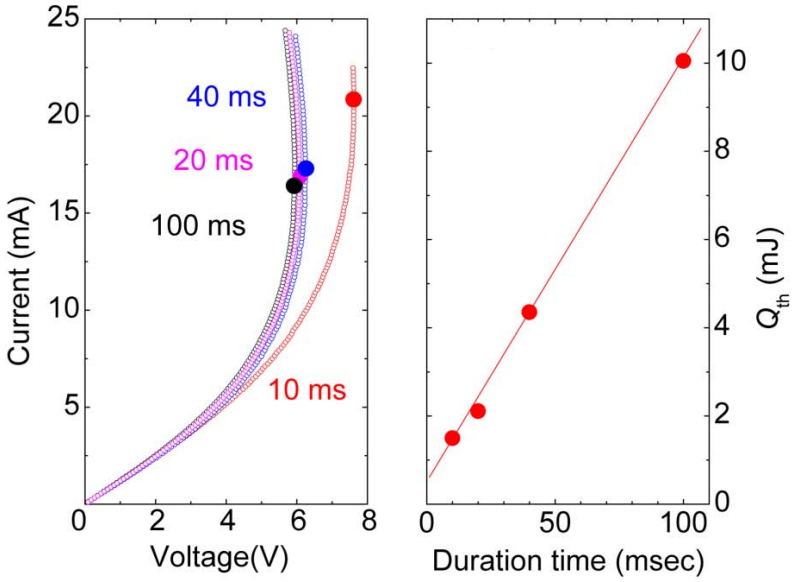


Figure 4.12 (left) The switching curves for pulse application EHc with a different duration time. The threshold $V_{th}$ and $I_{th}$ are defined from the maximum voltage in the IV curve. (right) Total heating $Q_{th}$ at the switching threshold estimated.

### 4.3.1 The model of insulator-metal transition under the electric field

We, next, consider whether the switching in $Ca_2RuO_4$ occurs in local or in bulk. As discussed in the development of switching into the resistance RAM, many of switching phenomena in insulating oxides have successfully been interpreted in terms of local switching. Two kinds of local-switching models have recently been proposed: one is due to formation of a filamentary path as seen in highly insulating oxides such as NiO[49], and the other is due to interface-resistance switching as seen in relatively conductive perovskite-oxide insulators[50]. In the case that switching occurs locally, the size effect on resistance and threshold voltage should be different from that in a bulk switching case. To inspect this point, we examine the voltage-current curves obtained by using a four-probe method for the samples with different sizes and shapes.

We show three models of the dielectric breakdown in solid,

1; Avalanche Breakdown (electric snow slide),

2; Zener Breakdown (electron emission field breakdown),
3; Joule heating (heating breakdown)
I argument to the threshold value of electric field ($E_{th}$ ~40 V/cm).

1, Avalanche Breakdown

Avalanche Breakdown is a breakdown by the multiplication of the electron density by the collision ionization in the solid. In addition, it is a model that the pass of the electric current appears in a solid material for a snow slide and produces conduction like another name. Therefore it remains in a small portion to a metal state in samples.

However, it was revealed that it was accompanied by a change of the x-ray diffraction in the breakdown of $Ca_2RuO_4$. It is clear that this breakdown (insulator-metal transition) is the bulk transition.

2, Zener Breakdown

Zener Breakdown is an electron goes through from valence band to a conduction band by tunneling effect (Zener effect) of the quantum mechanics and is the breakdown by conductive electron density doing multiplication. It is a judgment by Zener criterion.

The value of energy gap ($\varepsilon_{gap}$) which I estimated to be lowest under the atmosphere pressure and the difference of temperature ~60 K between room temperature and Mott transition temperature ($T_{MIT}$ = 357 K), and it is with $\varepsilon_{gap}$ ~5 meV in the case of $Ca_2RuO_4$. Using the value of $V_{th}$ ~40 V/cm at the atmosphere pressure and room temperature (when apply it to expression IV-1), fermi energy ($\varepsilon_F$) is $\varepsilon_F$ ~12 eV. Even if this value compares with biggest $\varepsilon_F$ ~ 0.2 eV of $Sr_2RuO_4$, which is the resemblance material which substituted Ca for Sr, it takes the double-figures big value. It is not thought to take big $\varepsilon_F$ in $Ca_2RuO_4$.

3, Joule heating

Joule heating is the so-called heating breakdown. It is a breakdown that a changes a state of material in itself by heating to occur by current flow.

The $T_{MI}$ decreases with pressurization in $Ca_2RuO_4$ is known ant take $T_{MI}$ ~300 K by pressurization in quite 0.5 GPa. Therefore a breakdown of $Ca_2RuO_4$ under a few pressurized was tried by Yamauchi [51]. However, $E_{th}$ of $Ca_2RuO_4$ did not almost move to the pressure and took the same value.

Furthermore in the x-ray diffraction measurement, the sharply peak of the metal phase after the insulator-metal transition can identify with the peak of the insulator phase before applying the voltage as showed by a structural change result. It is thought

that the contribution of the heating by applying electric field has little. Rather than these, I know that it is not the insulator-metal phase transition (breakdown) because of a sample run purely heating and beyond $T_{MI}$.

## 4.4 Measurement of x-ray diffraction

X-ray diffraction measurement at room temperature were measured with Cu-$K\alpha$ ($\lambda$ =0.1542 nm) radiation (40 kV, 30 mA) on a RINT2000 diffractometer (Rigaku). The data were collected in a step-scanning mode over the $2\theta/\theta$ range of 5-135° . The step width and step time are 0.02° and, respectively. I checked the lattice constant of the single crystal under the electric field and the impurities which I made $Ca_2RuO_4$.

The obtained crystals are plate-like cleaved with typical size of the crystals being $5\times10^{-3}$~10 $mm^3$. From cleaved $Ca_2RuO_4$ single crystals, x-ray diffraction patterns for (00l) reflections showed no impurity peaks as shown in Fig 4.13 . The x-ray incident angle is *c* -axis.

The single crystal of $Ca_2RuO_4$ is a plate-shaped crystal with a *c* -axis [(001)] plane was obtained by self-cleavage and is known that it has characteristic change in *c* -axis when insulator-metal transition. Estimated *c* parameter from the pattern is in the table. I show the (006) diffraction line that I measured under some voltage in Fig 4.13.

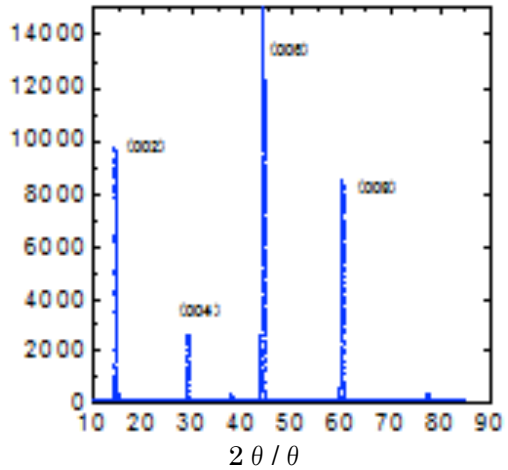

Figure 4.12 X-ray diffraction of single crystal

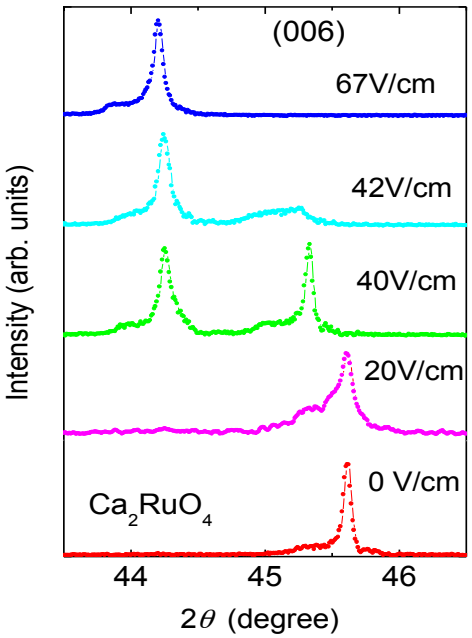


Figure 4.13 (006) diffraction line under electric-field

In *V*-control method, when an electric current has begun to flow metallically, a big black kite necessarily occurs in the current value. So, it is the problem to x-ray diffraction measurement near $V_{th}$. In current-control method, because I could control a current value, the x-ray diffraction measurement was enabled on a stable condition. In Fig 4.14, Voltage-Current characteristic and x-ray diffraction which I measured at the same time.

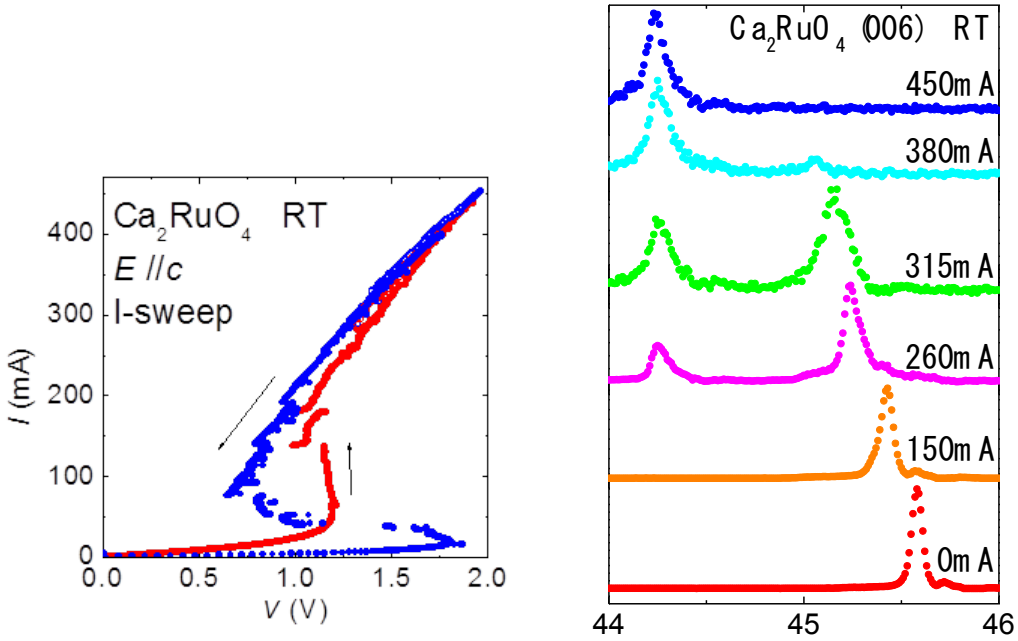

Figure 4.14 Voltage-Current characteristic (left) and x-ray diffraction (right) at the same time

Fig.4.13,4.14 shows x-ray diffraction measurement spectra (*E*// *c* by *V*-control). When there is zero electric field, a peak appears in $2\theta \sim 45.5^\circ$ . This means that short S-*Pbca* (insulator phase) of the *c* -axis head has crystal structure. Then, L-*Pbca* aspect (I make primary phase transition to metal aspect $2\theta \sim 44.2^\circ$ ) that I apply an electric field, and has a long *c* -axis head through 2 phase coexistence aspects from S-*Pbca* aspect in $E \sim 40$ V/cm. Furthermore, it becomes the single-phase alternating current of the L-*Pbca* aspect when I increase an electric field.

As a result, the breakdown of $Ca_2RuO_4$ is understood that it is the transition of "bulk" with the structure transition. Then, I compared the relations of the structure transition and the voltage-current properties. I compared the electric field dependence of the sample volume and the voltage-current properties.

The Fig.4.15 up shows the voltage-current properties with the insulator-metal transition (breakdown), Fig.4.15 down shows the volume fraction of the insulator-phase and the metal-phase in the electric field dependence. From the figures, after an electric current have begun to flow metallically, the *c* -axis constance head grew. I understood structure transition occurred after an electric current had begun to flow metallically.

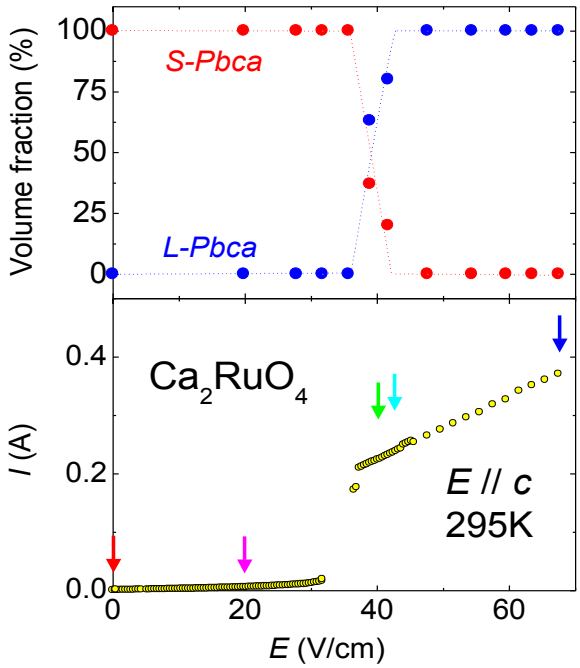


Figure 4.15 (up) The volume fraction of the Insulator-phase (S-*Pbca*) and the metal-phase (L-*Pbca*) in the electric field dependence. (down) The voltage-current properties.

We note that an isovalent substitution of Sr for Ca[50] or pressurisation[22] turns a Mott insulator to a quasi-two-dimensional Fermi- liquid metal without any carrier doping. In these cases, the Mott transition is interpreted in terms of a switching in the orbital occu- pation driven by the lattice flattening distortion[52]. In contrast, application of an E-field itself cannot directly act on the structural distortions, and in fact, the switching occurs prior to the structural transition as indicated by the comparison between Fig. 4.15.

### 4.4.1 Crystal structure under the electric field

Fig.4.16 is showed electric field dependence of lattice parameters of *c* -axis for 0-*V* -2 V (11.92Å under zero field). It is understood that the *c* -axis is gradually grows in the

insulator state with applying electric field. When the *c* -axis head reaches 12.01Å, $Ca_2RuO_4$ becomes insulator-metal coexistence phase, and it has long 12.20Å in a metal phase. Furthermore, a metal phase is made a single-phase to increase the induced voltage. The electric field (voltage) cause the structure transition with growth of the *c* -axis in $Ca_2RuO_4$. A change of the *c* -axis at the time of the insulator-metal phase transition is resemble at pressure and temperature.

I performed the x-ray diffraction measurement with fixed a sample to the glasswork. I put of the *ab* -plane side of the glass surface with the silver epoxy which it is I used to fix the gold wires. When the silver epoxy is dried and it hardens. Using the property, I fixed the *ab* -plane side of the sample and controlled in-plane distortion. I show the result in Fig.4.17.

Like a case not to fix a sample, I was able to confirm structure transition with a insulator-metal transition. However, the value of $E_{th}$ is increased and the coexistence phase of an insulator phase and the metal phase (slanted line part) is increased. It could be control the insulator-metal transition under the electric field by the control of the distortion in the *ab* -plane.

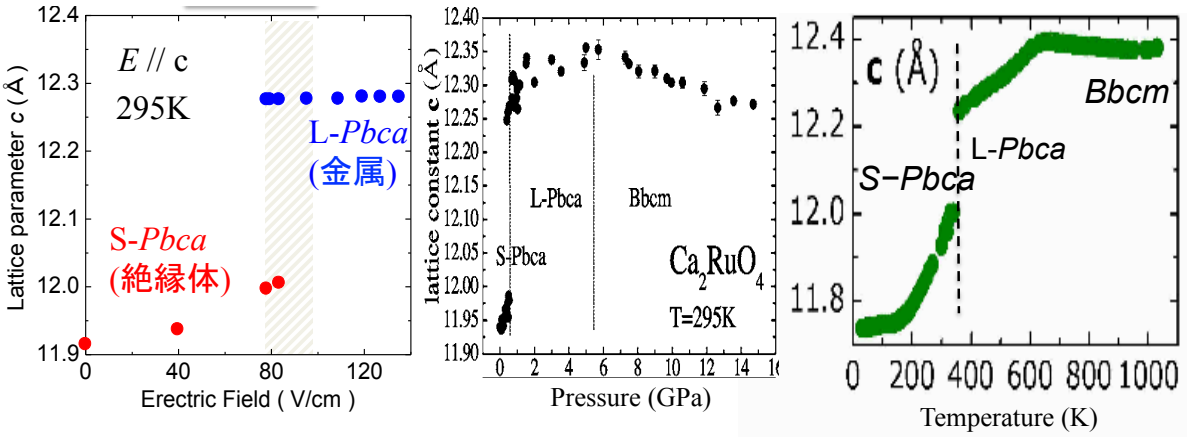


Fig 4.16 External field dependence of lattice parameters of *c* -axis
(left) Electric-field, (center) Pressure, (right) Temperature
In pure CRO, the high-T (T . 357 K) or high-P ( P . 0.5 GPa) metallic phase shows the structure called “L-Pbca”, with a weaker flattening and as well as a weaker tilt and smaller volume than the low-T (T , 357 K) or low-P (P , 0.5 GPa) insulating phase with the “S-Pbca” structure[48,49].

I compare with $Ca_2RuO_4$ and other Mott insulator. The value of $E_{th}$~40 V/cm of $Ca_2RuO_4$ is a small $E_{th}$ value as several columns declined in comparison with other Mott insulators. In addition, I have a very interesting characteristic in $Ca_2RuO_4$ that it is to be able to cause the breakdown of $Ca_2RuO_4$ under room temperature and atmosphere pressure whereas the breakdown experiment of other Mott insulators is mainly conducted at low temperature less than room temperature. When even an applied aspect thinks about electronic devices such as the storage medium, this characteristic is very interesting.

I compare the three fields (electric field, pressure and temperature) in $Ca_2RuO_4$ to investigate a cause why $Ca_2RuO_4$ is able to cause insulator-metal transition by low $E_{th}$. In Mott insulator $Ca_2RuO_4$, insulator-metal transition has been tried so far by changing pressure and temperature. The x-ray diffraction measurement had been measured with the pressure dependence and temperature dependence.

It is reported of the structural transition and structural parameters. The thing which behavior at the time of those metal-insulator transition shows, after the $c$ -axis head passed through growth from 11.92Å at insulator of room temperature and the atmosphere pressure to 12.01Å, and after having passed through double phase coexistence, it is apparent to 12.27Å of the metal phase.

This was very much similar to behavior that I reported in this study at the time of the electric field evocation insulator-metal phase transition. It is regarded the approach from two directions such as "filling control" as "band width control" about the metallization of the Mott insulator until now. However, the crystal structure is suggested the presentation of the way of thinking that is new as a key and control of the electronic state that it is if I can dealt with insulator-metal phase transition of $Ca_2RuO_4$ as unified behavior not to depend on the kind of the outside field.

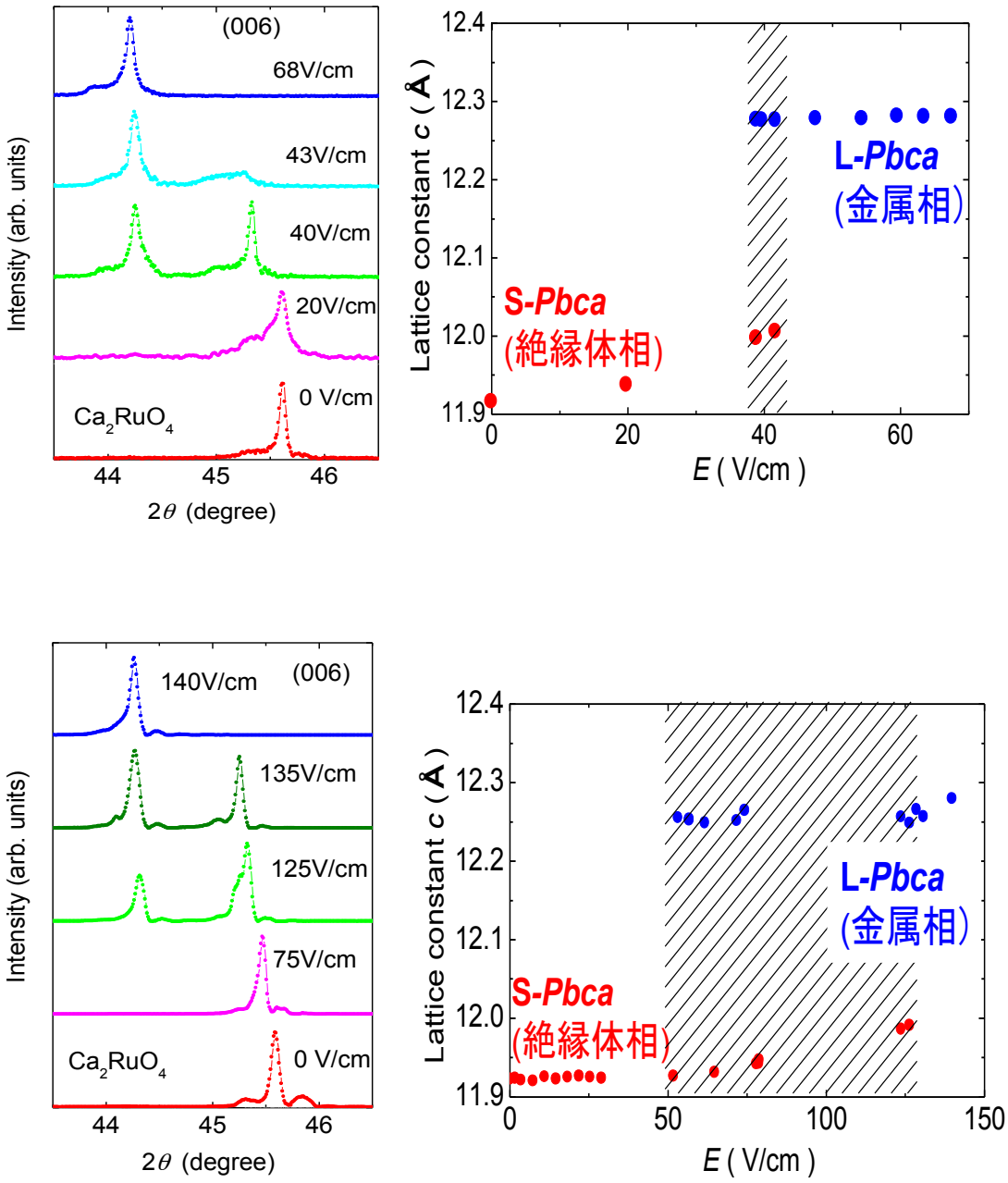


Figure 4.17 (up) The x-ray diffraction measurement with a sample of free distorsion
(under) The x-ray diffraction measurement with fixed a sample to the glasswork

## 4.5 Soft x-ray measurement

The sample dimensions used in this study were about 3×3×0.1 $mm^3$. Gold electrodes were sputtered on both ends of the sample, and twisted gold wires with diameter of 25 μm were attached to the electrodes using silver epoxy. We clarified a change of the crystal structure parameter at the time of the insulator-metal (breakdown) transition while adding an electric field to $Ca_2RuO_4$ by performing the x-ray diffraction measurement. We move a viewpoint of vision to the micro phenomenon in this chapter until now by discussing the electronic state from the macro phenomenon such as transport property and the crystal structure change. We finally compare these results and mention the details of the insulator-metal transition and the structural change.

We performed the soft x-ray measurement while an electric current. But all the lines for the soft x-ray measurement are kept by the high vacuum because it is strong in dispersion. The sample space is in vacuum equally, too. We must watch that the heat is difficult to escape in comparison with an experiment in the air atmosphere that we spoke so far.

Fig 4.18 shows the raw Voltage-Current characteristic of the whole circuit, which includes the voltage at the load resistance ($V_L$). To clarify the phase transition, the net Voltage-Current characteristic of the sample is displayed in Fig. 4.18(b) by subtracting $V_L$. Open squares denote the points at which the spectra were measured.

The Voltage-Current characteristic can be divided into three regimes: a high-resistive insulator state (phase 1), a transient insulator-metal coexisting state (phase 2), and a low-resistive metallic state (phase 3). The resistance of the sample was initially 500Ω at 0 V (0 mA), and it retained the order of magnitude in the phase 1.

After the first critical point (1.07 V, 10 mA), the sample resistance rapidly decreases down to several Ω indicating the so-called negative differential resistance in the phase 2. Voltage and current values at each measurement point were stable, however, extreme care was required during the operation between the points. It should be noted that joule heat generated at the sample is rather diminishing due to the rapid decrease in the sample resistance in this phase. This ensures that the spectral changes observed by us were electric-field induced ones.

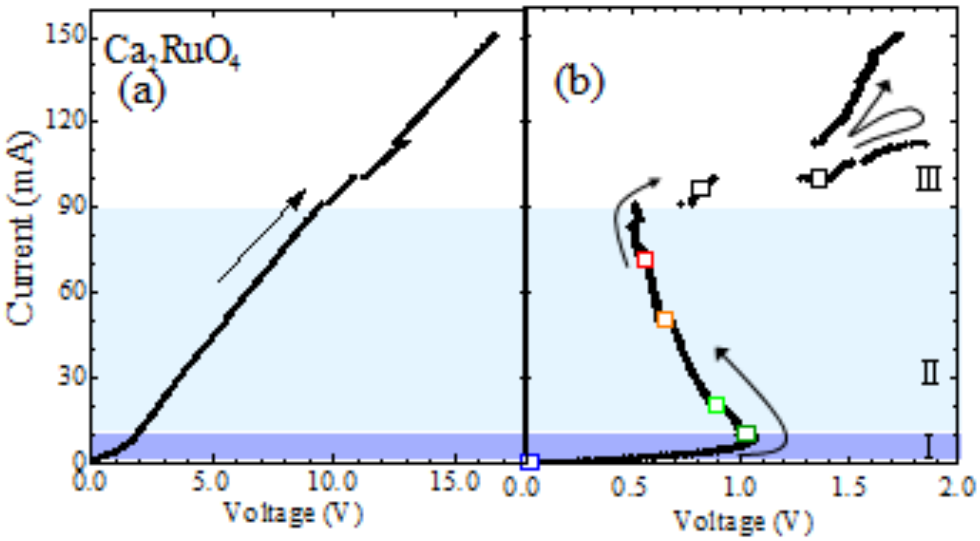


Figure 4.18 (left) The raw Voltage-Current characteristic
(right) The Voltage-Current characteristic of the sample

Above the threshold current of 90 mA, the sample undergoes several transitions with discontinuous jumps in the Voltage-Current characteristic. The sample resistance in the phase 3 was on the order of 10 Ω. The discontinuities in the graph are due to the cracks in the sample caused by sudden and irreversible elongation along the *c* -axis, which was check by x-ray diffraction measurements.

The apparent resistance of the sample seems to be slightly larger than that in the phase 2. This is mainly due to the contact resistance between fractured layers within the sample, even though each layer is metallic, a redistribution of the *d* electrons at the Insulator-Metal transition accompanied by the structural change, x-ray absorption spectroscopy (XAS) at the O *K*- edge.

Taking into account the difference in the angular dependence between the apical O 2*p*-Ru 4*d* $t_{2g}$ bonding and in-plane O 2*p*-Ru 4*d* $t_{2g}$ bonding. The total electron yield method commonly used for x-ray absorption spectroscopy measurements in the soft x-ray region is, however, inapplicable to an electric field-dependent x-ray absorption spectroscopy measurement because of the deflection of electrons. In this study, we therefore employed the partial fluorescence yield method for x-ray absorption spectroscopy measurements (PFY-XAS) using a soft x-ray spectrometer, which was also applied to observe O *K*-edge x-ray emission spectra (XES).

All the spectra taken in phases 1 and 2 are summarized in Fig 4.19. The rainbow-color represents the order of six current conditions from 0 mA, 0 V (blue) to 100 mA, 0.8 V (red). The O-*K* x-ray absorption spectroscopy are normalized to unity at the peak maximum of 533.4 eV, while the O-*K* $\alpha$ x-ray emission spectra are area-normalized to a comparable scale.

Firstly, we explain the x-ray absorption spectroscopy results. Overall features are the same as experimental, and theoretical data [53] reported previously by other researchers. The structures from 528 to 530 eV (labeled as A and B) and that from 531 to 534 eV (labeled as C and D) are assigned to transitions from the O 1*s* core level to the O 2*p* orbitals hybridized with the unoccupied Ru 4*d* $t_{2g}$ and $e_g$ state, respectively.

From a molecular orbital point of view, these hybridized states can be considered to be pd$\pi$* and pd$\sigma$* states[54]. Furthermore, Mozokawa *et al.* concluded from their angle-dependent x-ray absorption spectroscopy results that peaks A and B, and peaks C and D, are due to hybridization between the apical and planer oxygen sites, respectively. Clear electric-field dependence is found in the $t_{2g}$-derived region. The spectral weight gradually shifted from peaks A to B by increasing current amplitude. A similar spectral-weight shift was also observed by temperature variation from 90 K to 300 K, which is accompanied by 2.5% elongation of the *c*-axis similar to our results.

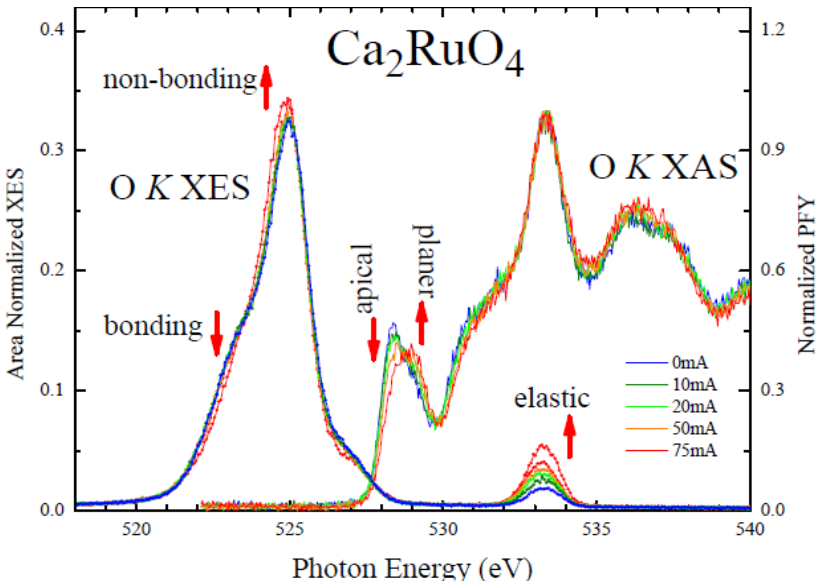

Figure 4.19 x-ray absorption spectroscopy and x-ray emission spectra

### 4.5.1 The incidence-angle dependence of x-ray absorption spectroscopy

The assignment of the peaks was also verified by us. Fig 4.20 shows the incidence-angle ( $\theta$ ) dependence of the O-*K* x-ray absorption spectroscopy observed in the (a) polarized and (b) depolarized configurations. In the former geometry, the unoccupied O 2*p* final state in the dipole-transition lies along the *a*-axis and is unchanged regardless of , therefore slight $\theta$ dependence is observed.

The polarization vector of the incident photon (e) lies in the *ac* -plane in this configuration: e//*a*-axis at $\theta$ =0° (normal incidence) and e//*c*-axis at $\theta$ =90° (grazing incidence). In the normal (grazing) incident regime, the planer (apical) oxygen sites are preferably detected in the pd $\sigma$ * region, which results in the enhancement of the D (C) peak as observed in our present study. This trend, together with the $\theta$ dependence of the peaks A and B, is the same as that previously reported by Mizokawa *et al.* [39]

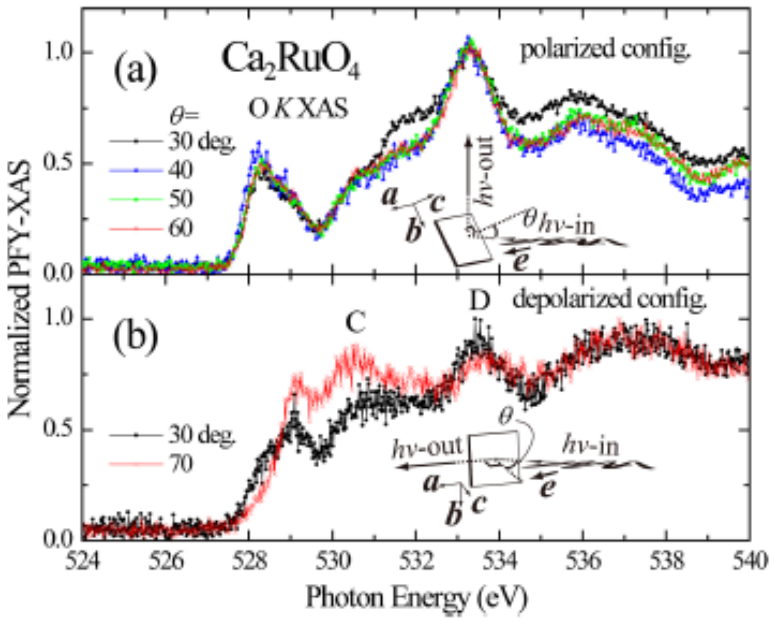


Fig 4.20 The incidence-angle ( $\theta$ ) dependence of the O-*K* x-ray absorption spectroscopy observed in the (a) polarized and (b) depolarized configurations.

### 4.5.2 X-ray emission spectra

In the next place, the field-dependent x-ray emission spectra result in Fig 4.19. The elastic peak energy of 536.1 eV corresponds to the 5th peak (D) in the x-ray absorption spectra. A broad fluorescence feature is common to other inorganic oxides[55,56]. The main intense peak at 526 eV can be assigned to the de-excitation from the non-bonding O 2*p* states, and the shoulder at 523 eV can be assigned to the bonding ones. Again, six spectra are displayed with colors corresponding to the current amplitude of the x-ray absorption spectra.

A gradual increase of the elastic peak by current is apparent, directly indicating the increase of reflectivity. This is consistent with the Voltage-Current characteristic in Fig 4.18 where the gradual increase of the metallic phase is evidenced. Even more important changes induced by current in the spectra are the decrease/increase of the bonding/non-bonding peaks, as well we a faint decrease of a bump structure at 527 eV.

A key factor for the changes in the spectral weight is the elongation of the *c* -axis, because the bonding between apical oxygen 2*p* states with Ru 4*d* states is weakened. It should be mentioned that the band-gap of $Ca_2RuO_4$ cannot be estimated from our results, since the final state of x-ray absorption spectra process contains a core hole and therefore its energy level is pulled down.

### 4.5.3 Discussion by soft x-ray measurement

Compared to the x-ray absorption spectra, the x-ray emission spectra spectral width is large due to the short lifetime of the O 1*s* core hole, therefore the contribution of the in-plane and apical oxygen is not separated, unlike the x-ray absorption spectra case. The presence of the core hole also prevents us from estimating the band-gap of $Ca_2RuO_4$, since the final state of the x-ray absorption spectra process contains a core hole and then its energy level is pulled down.

The electric-field induced spectral weight shifts in the spectra are considered with regard to the number of holes, $n_{xy}$ and $n_{yz}$ / $n_{zx}$. The shift from peaks A to B observed in x-ray absorption spectra corresponds to an increase of $n_{xy}$. Mizokawa *et al.*, roughly estimated the $n_{xy}$ / $n_{yz}$ / $n_{zx}$ ration increases from 1/3 to 1 from their temperature dependent experiment. The amount of the spectral weight shift is quite similar in both the temperature variation from 90 K to 300 K and the electric field application in the

present study. We can conclude that the electric field induces the structural transition followed by an induces of $n_{xy}$, or vice versa.

The drastic increase of $n_{xy}$ is nicely illustrated by the recent theoretical calculation based on the dynamical mean-field theory [57]. Figure 4.21 shows the energy dependence of the electronic densities of the (a) $d_{xy}$ state and (b) $d_{yz/zx}$ state. Each line is reproduced from the original figure 11 in Ref. 57.

The main peak of the $d_{xy}$ state locates below the Fermi level at the binding energy ($E_B$) of 0.5 eV in the insulator phase, while it shifts upward across the Fermi level in the metallic phase, leading to an increase in $n_{xy}$. The majority peak of $d_{xy}$ state located below the Fermi level in the insulator phase moves upward across the Fermi level in the metallic phase as shown in the figure 4.21 in the reference.

Also presented in this figure is the decrease of the occupied density of the $d_{xy}$ state at binding energies ($E_B$) ranging from 1 to 3 eV through the Insulator-Metal transition. Besides, the occupied density of $d_{yz/zx}$ states are broadened, which have peaks at $E_B = 3$ eV in the insulator phase in Fig 4.21. The decrease of the Ru 4*d* occupied states results in the increase of the O 2*p* occupied states, if the number of valence electrons is conserved. This corresponds to the increase of the non-bonding peak in x-ray emission spectroscopy through the Insulator-Metal transition.

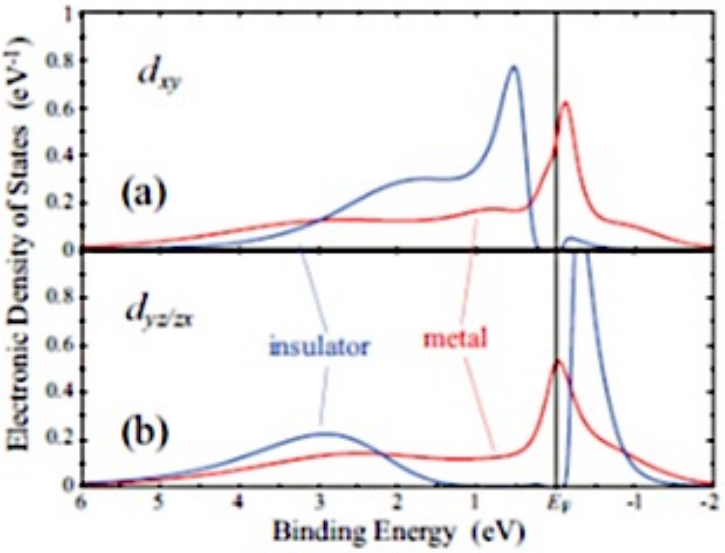


Figure 4.21 The energy dependence of the electronic densities of the (a) $d_{xy}$ state and (b) $d_{yz/zx}$ state

The decrease of the bonding peak in x-ray emission spectroscopy can also be explained by the decrease in the occupied density the of $d_{yz\,/\,zx}$ states. The orbital character of the valence band, as concluded from the x-ray emission spectroscopy results, is consistent with that deduced from the valence band photoemission spectra [39].

## 4.6 Model of the metal-insulator transition in $Ca_2RuO_4$

In the $Ca_3Ru_2O_7$, it was found that the metal-insulator transition at $T_{MI.}$ It is accompanied by a softening and broadening of the out-of-phase oxygen phonon mode. It is certainly an important system that provides a precious opportunity for studying the strongly correlated interaction which is the central feature of the transition metal oxides.

In this study, the negative differential resistance was confirmed by current induced in Voltage-Current properties in current sweep method. It is understood that the insulator phase and the metal phase are vertically-ordered for an electrode. It is expected that the pass of the electric current such as the filament occurs because of "insulator phase" and "metal phase" is showing vertical to electrode not parallelism. However, the structural phase transition was confirmed by the x-ray diffraction measurement. It is concurrently the form of locally filament add it and the pass of the electric current appearing and know the insulator-metal phase transition as bulk.

In addition, by coincident measurement of Voltage-Current characteristic and x-ray diffraction, a metal phase in the x-ray diffraction is confirmed after pass through negative differential resistance is disappearance to differential calculus resistance right by Voltage-Current properties. While negative differential resistance state, bulk state is insulator phase. We can do the whole sample with a metal state afterwards by increasing the current value. There are not the reported cases from the local change to transition of the bulk so far. It is thought that a structural change may become the key as a thing to connect this local change and the bulk change .

The structural transition with the insulator-metal transition of $Ca_2RuO_4$ changes the *c*-axis head ~3%, and the volume amount of change extends to ~2%. This change is a large change as it leads to destruction of sample oneself. The coexistence of the "local" element and the "bulk" element in $Ca_2RuO_4$ is special phenomena which assumes a

change of the structure transition intermediation.

Though $Ca_2RuO_4$ has the number of the carriers same as $Sr_2RuO_4$ which substituted Ca for Sr. Ground state is Mott insulator whereas $Sr_2RuO_4$ is spin triplet superconductor. This characteristic is a high-temperature superconductor of the same perovskite type. But electric charges collect to top oxygen of the $RuO_6$ octahedron in $Ca_2RuO_4$ so that it is reported. It is thought that this is because there are few electronic numbers of the conduction side.

We think about that an electric charge of top oxygen that the insulator-metal phase transition was saved to this limit. The electric field that we took up in this study occurs because of applying it. It was thought that I woke up insulator-metal phase transition only in an electric charge added by outside electric field to apply in the model of the Zener breakdown that we proposed so far.

However, which is guessed when it may cause insulator-metal phase transition if originally there are many electric charges contained by material oneself even if the quantity of the electric charge. As the outside electric field is a whit. If it is dropped in a conduction side by an electric field, and the electric charge that collected to top oxygen made it metal, we think from the size of the electric charge that $Ca_2RuO_4$ originally has, and there is the thing which can nod in the littleness of the threshold electric field.

There remains an absorbing question. What is happening in the electric field induced metallic phase at low temperatures. To the best of our knowledge, there has been no previous example of cooling a volatile switching-system while keeping the metallic state. With the parameters found, it would reach quite a large value, over 100 kV/cm at 4.2 K. In reality, it is extremely difficult to induce a Mott transition by the electric field at low temperatures.

Keeping this in mind, let us now present the results of current biased experiments. Figure 4.22 (a) shows in-plane resistance measured with a constant current of 420 mA by a two-probe method as a function of temperature. Surprisingly, the temperature-variation shows a positive slope ( $\Delta \rho_{ab}/dT > 0$) indicating metallic conduction in the temperature range from 300 to 4.2 K. That is, once the switching has occurred, the electric-field-induced metallic state becomes stable with flowing current even in electric fields much less than $E_{th}$. A heuristic analogy may be drawn with a well-known phenomenon that “flowing” suppresses the freezing point of water.

Figure 4.22 (b) shows the same data as (a) but for temperatures below 30 K. An abrupt change in the metallic slope at ~15 K is reminiscent of the resistivity change associated with a ferromagnetic transition in the pressure induced metallic $Ca_2RuO_4$ in

Fig. 4.22 (c). Thus, we naturally anticipate that a ferromagnetic ordered state appears also in this current-driven metal as a stationary but nonequilibrium state. Indeed, we have observed a change in the local magnetic field with magnetic probes. Although such measurements are technically not easy, they are in progress.

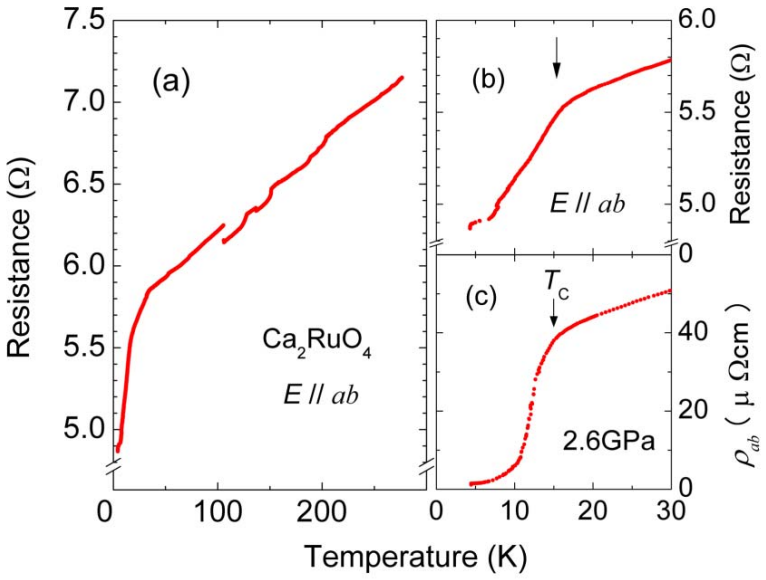


Figure 4.22 Temperature variations of in-plane resistance. (a) With constant current 420 mA. (b) Same data as (a) but for T~30 K: The slope of the in-plane resistance in the electric field changes abruptly at ~15 K as indicated by an arrow. (c) In plane resistivity under P ~2.6 GPa, for which a similar variation to the electric field induced case is seen at a temperature corresponding to ferromagnetic $T_C$.

We have experimentally shown that a number of unusual phenomena emerge in the Mott insulator $Ca_2RuO_4$ by applications of electric fields and currents. First, the switching is induced by application of such low fields as $E_{th}$ ~ 40 V/cm, which is$10^2$,$10^3$ times lower than that reported in other Mott insulators. Second, the switching is accompanied by a bulk structural phase transition. Third, the induced metallic phase becomes stable to low temperatures if the flowing bias current is maintained.

To add, we also show that under bias current the antiferromagnetic transition, characteristic of the Mott insulating state of $Ca_2RuO_4$, disappears and moreover ferromagnetic ordering emerges below 15 K as indicated by the resistance drop as well as the spontaneous magnetization at low temperature.

It should be emphasized that the “flowing current” plays a key role in maintaining the induced metallic state, although the switching itself is induced not by the application of current but voltage. This phenomenon is truly unexpected and most probably requires a mechanism of stabilising a steady but nonequilibrium state (current maintained metal) over an equilibrium state (Mott insulator). Thus, application of electric fields and/or flowing currents has a great potential as a new tool to induce novel quantum phenomena in a variety of materials. Utilising such nonequilibrium states will cer- tainly help expanding our knowledge of material science [58-60].

# Chapter5 Conclusion

- Colossal magneto-resistance under the pressured $Ca_2RuO_4$

We summarize several attractive findings in an anisotropic and colossal magneto-resistance effect in the pressure induced Mott transition system of $Ca_2RuO_4$ as follows: first, the temperature variation in both he transversal magneto-resistance (J $\perp$ $\mu_0$ H) and the longitudinal magneto-resistance (J// $\mu_0$H) show a negative dip near $T_C$. The dip nature is qualitatively understood as a change in magnetic fluctuation as is also seen in typical ferromagnetic metals. Second, attention has been paid to the positive transversal magneto-resistance peaking at $H_A$ ~9.5 T and reaching +120%. Such a giant positive effect, which is actually rare in bulk system, is characteristic of the mixed state; therefore, this is due to the magnetic tunnelling between the ferromagnetic islands isolated by the thin insulating layers. Lastly, we propose the importance of the orbital physics as another key factor for amplifying the magneto-resistance effect. Indeed, this is clearly indicated by the largeness of the anisotropy magnetic field of 9.5 T.

- Insulator-Metal transition under the Electric-field

In this study, we succeeded in Insulator-Metal transition by a view of electric resistance for an emergency called threshold electric field $E_{th}$~40V/cm at room temperature in a low electric field in Mott insulator $Ca_2RuO_4$. *E*-field induced superconductivity has recently been reported in the surface layer of a band insulator $SrTiO_3$ by the *E*-field application of 20 kV/cm. The other is a Mott transition induced by applying *E*-fields, namely, "switching". Some transition-metal oxides in strongly correlated electron systems have gained attention as a candidate for the switching to practical use as an electronic device such as resistance RAM. Most of these previously reported switching phenomena have been achieved only at low temperatures and/or high voltage (typically 1–100 kV/cm).

Surprisingly, the threshold value $E_{th}$ ~40 V/cm for $E$ //$c$ is far smaller than our expectation of ~4 MV/cm. We typically obtained $E_{th}$ ~50 V/cm for $E \perp c$. Thus, the value of the $E_{th}$ is almost independent of the electric field direction.

- Crystal structure change under the Electric-field

We confirmed that the structure transition (the lattice change) was taking place by performing the x-ray diffraction measurement at the same time. At the time of the electric field evocation Insulator-Metal phase transition, $Ca_2RuO_4$ shows a structural

change (a lattice change) like with the other outside ground such as pressure and the temperature. Therefore it is assumed that the effect that $Ca_2RuO_4$ itself has inherent and may act essentially more effectively. In other words, as for the dielectric breakdown of $Ca_2RuO_4$, it became clear the current thing was not able to pass for a simple filament.

At the time of the Insulator-Metal phase transition by the electric field, the *c*-axis constant gradually extended it from 11.92Å to 12.01Å, and jump to 12.20Å, having reached a structural change it becoming clear of the metal aspect. The electric field evocation Insulator-Metal phase transition is the primary phase transition with the change of the structure. However, about the low threshold electric field as is unique elsewhere, still theoretical explanation without being able to elucidate it.

・ By x-ray absorption spectroscopy and x-ray emission spectroscopy with electric field induced $Ca_2RuO_4$

The O *K*-edge x-ray absorption spectroscopy and x-ray emission spectroscopy of $Ca_2RuO_4$ were measured under an *E*-field applied field in order to investigate the changes in the valence and conduction bands through the Insulator-Metal transition. Spectral weight shifts were observed in both series of spectra. The changes in x-ray absorption spectroscopy can be comprehended as an increase in $d_{xy}$ holes ($n_{xy}$) though metallization, which is consistently understood by the model used to explain the temperature dependence in x-ray absorption spectroscopy.

We have measured O 1*s* the partial fluorescence yield method for x-ray absorption spectroscopy and x-ray emission spectroscopy spectra of $Ca_2RuO_4$ to check the change of a valence electron band and the conduction band with the insulator-metal transition under an electric field. Movement of the spectrum strength was seen with both x-ray absorption spectroscopy and x-ray emission spectroscopy. This change of x-ray absorption spectroscopy was the same trend explained in temperature dependence. The under with $n_{xy}$ increasing with metallization.

The enhancement in the non-bonding peak in x-ray emission spectroscopy can be simply understood by the weakening of the O 2*p*-Ru 4*d* hybridization caused by the elongation of the *c*-axis through the Insulator-Metal transition. In addition, not only the enhancement of the non-bonding peak but also the increase of $n_{xy}$ is nicely elucidated by the recent theoretical band calculation.

The increase in nonbonding state with metallization seen in x-ray emission spectroscopy knew could be understood it that the O 2*p*-Ru 4*d* combination brought weakened by the spread of the *c*-axis with the structural transition. While it showed the agreement that was good with the change of the valence electron band based on the

recent DMFT calculation.

This change in x-ray absorption spectroscopy and XES was consistent with temperature dependence data with the $n_{xy}$ increasing with metalize.

We can consider these changes to be a characteristic (= PROPERTY) of $Ca_2RuO_4$ itself and not due to a kind of outside field (=FACTOR,VARIABLE). It is very interesting that the role of top Oxygen (in particular *c* - axis length) structural changes in the crystal the characteristic (Metal versus Insulator). Future research will be needed to examine the effect that the E-field brings by using a new pulse *E*-field approach. Also, neutron measurement could be used to more accurately measure data.

We //=the

In addition, to measure the magnetization and the transport property at the low temperature in the electric field, and act for elucidation of the ground state of $Ca_2RuO_4$ in the electric field state to apply. And in cooperation with a coworker, it is new the studies such as the metal-insulator transition of $Ca_2RuO_4$ by the optical pumping want to reach as an effect of the places, too. We deepen unified understanding in Mott insulator Ca2RuO4.

# Bibliography


1. Imada, M., Fujimori, A. & Tokura, Y. Metal-insulator transitions. Rev. Mod. Phys. 70, 1039 (1998).
2. G. G. Lonzarich, Nat. Phys. **1**, 11 (2005)
3. Y. Maeno, H. Hashimoto, K. Yoshida, S. Nishizaki, T. Fujita, J. G. Bednorz,and F. Lichtenberg, Nature **372** (1994) 532.
4. A. P. Mackenzie, R. K. Haselwimmer, A. W. Tyler, G. G. Lonzarich, Y.Mori, S. Nishizaki, and Y. Maeno, Phys. Rev. Lett. **80** (1998) 161.
5. S. Nakatsuji, S. Ikeda, and Y. Maeno, Phys. Soc. Jpn. **66** (1997) 1868.
6. S. Nakatsuji and Y. Maeno, J. Solid State Chem. **156** (2001) 26.
7. M. Braden, G. Andre, S. Nakatsuji, and Y. Maeno, Phys. Rev. B **58**(1998) 847.
8. C. S. Alexander, G. Cao, V. Dobrosavljevic, S. McCall, J. E. Crow, E.Lochner, and R. P. Guertin. Phys. Rev. B **60** (1999) R8422.
9. H.Adachi and M.Sigrist Phys.Rev.B80,155123(2009).
10. S.A.Grigera, et.,al. Science 294,329(2001).
11. Rozenberg, M. J., Inoue, I. H. & Sanchez, M. J. Phys. Rev. Lett. 92, 178302 (2004).
12. Inoue, I. H. & Rozenberg, M. J. T Adv. Funct. Mater. 18, 2289 (2008).
13. Reyren, N. et al. Science 317, 1196 (2007).
14. Ueno, K. et al. Nature Materials 7, 855–858 (2008).
15. Meijer, G. I. Science, 319, 1625 (2008).
16. Waser, R. & Aono, M.. NatureMaterials 6, 833 (2007).
17. Kanki, T., Kawatani, K., Takami, H. & Tanaka, H. D Appl. Phys. Lett. 101, 243118 (2012).
18. Iwasa, Y. et al. Appl.Phys. Lett. 55, 2111 (1989).
19. Yamanouchi, S., Taguchi, Y. & Tokura, Y. Phys. Rev. Lett. 83, 5555 (1999).
20. Taguchi, Y., Matsumoto, T. & Tokura, Y. Phys. Rev. B 62, 7015(2000).
21. Hatsuda, K., Kimura, T. & Tokura, Y. Appl. Phys. Lett. 83, 3329 (2003).
22. Nakamura, F. et al. Phys. Rev. B 65, 220402(R) (2002).
23. Nakamura, F. et al. Phys. Rev. B 80, 193103 (2009).
24. Alireza, P. L. et al. Journal of Physics: CondensedMatter 22, 052202 (2010).
25. Anisimov, V. I., Nekrasov, I. A., Kondakov, D. E., Rice, T. M. & Sigrist, M. Eur. Phys. J. B 25, 191 (2002).
26. Koga, A., Kawakami, N., Rice, T. M. & Sigrist, M. Orbital-selective Phys. Rev. Lett. 92, 216402(2004).
27.

28. F. Nakamura, T. Goto, M. Ito, T. Fujita, S. Nakatsuji, H. Fukazawa, Y.Maeno, P. Alireza, D. Forsythe, and S. R. Julian, Phys. Rev. B **65** (2002)220402(R).
29. Fukazawa, H. & Maeno, Y. Phys.Soc. Jpn. 70, 460–467 (2001).
30. Zener, C. Proc. Roy. Soc. London. Ser. A137, 696 (1932).
31. Mackenzie, A. P. & Maeno, Y. Rev. Mod. Phys. 75, 657 (2003).
32. F.Nakamura, et al., J. Phys. Soc. Jpn. 76 (2007) Suppl.A, 96-99.
33. T.Takemoto, Hiroshima University H20 Master's thesis .
34. Friedt, O. et al. Phys. Rev. B 63, 174432 (2001).
35. Steffens, P. et al. Phys. Rev. B 72,094104 (2005).
36. Kim, D. C. et al.. Appl. Phys. Lett. 88, 202102 (2006).
37. E. Gorelov, M. Karolak, T. O. Wehling, F. Lechermann, A. I. Lichtenstein,and E. Pavarini, Phys. Rev. Lett. **104** (2010) 226401.
38. L. M. Woods, Phys. Rev. B **62** (2000) 7833.
39. T. Mizokawa, L. H. Tjeng, G. A. Sawatzky, G. Ghiringhelli, O. Tjernberg,N. B. Brookes, H. Fukazawa, S. Nakatsuji, and Y. Maeno, Phys.Rev. Lett. **87** (2001) 077202.
40. T. Mizokawa. New J. Phys. **6** (2004) 169.
41. T. Mizokawa, L. H. Tjeng, H.-J. Lin, C. T. Chen, S. Schuppler, S. Nakatsuji,H. Fukazawa, and Y. Maeno, Phys. Rev. B **69** (2004) 132410.
42. Y.Senoo, Hiroshima University H16 Master's thesis .
43. S.Nakatsuji and Y.Maeno, Physical Review Lett.84, (2000)2666.
44. R.Nakai, Hiroshima University H18 Master's thesis .
45. M. Watanabe, A. Toyoshima, Y. Azuma, T. Hayashi, Y. Yan, and A.Yagishita, Proc. SPIE **3150** (1997) 58.
46. Y. Harada, H. Ishii, M. Fujisawa, Y. Tezuka, S. Shin, M. Watanabe, Y.Kitajima, and A. Yagishita, J. Synch. Rad. **5** (1998) 1013.
47. Concerning the configuration of the polarization vectors of the incidentand emitted photons, see also the figure 1 in Ref. 16.
48. T.Negishi, Kyoto University H20 Graduation thesis .
49. . Sawa, A., Fujii, T., Kawasaki, M. & Tokura, Y. Interface resistance switching at afew nanometer thick perovskite manganite active layers. Appl. Phys. Lett. 88, 232112 (2006).
50. Nakatsuji, S. & Maeno, Y. Quasi-two-dimensional Mott transition systemCa2-xSrxRuO4. Phys. Rev. Lett. 84, 2666 (2000).
51. Y.Yamauchi Hiroshima University H21 Master's thesis .
52. Gorelov, E. et al. Nature of the Mott transition in Ca2RuO4. Phys. Rev. Lett. 104,

226401 (2010).

53. H.-J. Noh, S.-J. Oh, B.-G. Park, J.-H. Park, J.-Y. Kim, T. Mizokawa, L.H. Tjeng, H.-J. Lin, C.T. Chen, S. Schuppler, S. Nakatsuji, H. Fukazawa,and Y.Maeno, Phys. Rev. B **72** (2005) 052411.

54 J. H. Jung, Z. Fang, J. P. He, Y. Kaneko, Y. Okimoto, and Y. Tokura,Phys. Rev. Lett. **91** (2003) 056403

55. N. Nakajima, M. Deguchi, H. Maruyama, K. Ishiji, and Y. Tezuka, Jpn.J. Appl. Phys. **49** (2010) 09ME04.

56. E. Z.Kurmaev, R. G,Wilks, A.Moewes, L. D. Finkelstein, S. N. Shamin,and J. Kuneˇs, Phys. Rev. B **77** (2008) 165127.

57. M. Karolak, T. O. Wehling, F. Lechermann, and A. I. Lichtenstein, J.Phys. Condens. Matter. **23** (2011) 085601.

58 R. Okazaki (private communication); see also R. Okazaki, Y. Nishina,Y.Yasui, I. Terasaki, F. Nakamura, Y. Kimura, M. Sakaki, and T. Suzuki,Am. Phys. Soc., APS March Meeting 2012, abstract H9.001.

59. Sawano, F. et al. An organic thyristor. Nature 437, 522–524 (2005).

60. Ajisaka, S., Nishimura, H., Tasaki, S. & Terasaki, I. Nonequilibrium Peierls Transition. Progress of Theoretical Physics 121, 1289–1319 (2009).

# Acknowlegement

The author would like to express his gratitude to Prof. T.Suzuki for basic knowledge, an experiment technology, how to write scientific article, various advice including the way of the announcement though this work. I would like to express his sincere thanks to Dr. N Nakajima for useful advice and discussion for the measurement soft x-ray at Photon Factory. I acknowledge Dr. F Nakamura and T. Takemoto, Y.Yamauchi Y. Kimura, Y.Yamanaka, S.Tamaru for their experimental helps. They also confirmed that heating is insignificant at $E_{th}$. I thank to all the colleagues, senior and junior co-works of Suzuki laboratory for various assistance through this work. The staffs of the Photon Factory are acknowledged for their assistance with machine operation. Benefits were received from the Natural Science Center for Basic Research and Development (N-BARD), Dr. K.Umeo and K.Hagioka, Hiroshima university for supplying the liquid-helium. I thank "monodukuri-puraza" to spare time many times and provide a new idea in response to consultation, which they met without doing one unpleasant face in the demand that it is impossible.

Finally, I appreciate helps from my friends and family.

# 公表論文

(1) Electric-field induced insulator-metal transition in $Ca_2RuO_4$ probed by x-ray absorption and emission spectroscopy
Mariko Sakaki, Nobuo Nakajima, Fumihiko Nakamura, Yasuhisa Tezuka, and Takashi Suzuki
Journal of Physical Society of Japan **82** (2013) 093707.

(2) Electric-field-induced metal maintained by current of the Mott insulator $Ca_2RuO_4$.
Fumihiko Nakamura, Mariko Sakaki, Yuya Yamanaka, Sho Tamaru, Takashi Suzuki and Yoshiteru Maeno
Scientific Reports 3 (2013) 205106.

# Electric-field induced insulator-metal transition in $Ca_2RuO_4$ probed by x-ray absorption and emission spectroscopy

Mariko SAKAKI[1], Nobuo NAKAJIMA[2]*, Fumihiko NAKAMURA[1], Yasuhisa TEZUKA[3], and Takashi SUZUKI[1,4,5]

[1]*Department of Quantum Matter, ADSM, Hiroshima University, Higashi-Hiroshima 739-8530, Japan*
[2]*Graduate School of Science, Hiroshima University, Higashi-Hiroshima 739-8526, Japan*
[3]*Graduate School of Science and Technology, Hirosaki University, Hirosaki 036-8561, Japan*
[4]*Institute for Advanced Materials Research, Hiroshima University, Higashi-Hiroshima 739-8530, Japan*
[5]*Cryogenics and Instrumental Analysis Division, N-BARD, Hiroshima University, Higashi-Hiroshima 739-8526, Japan*

A novel insulator-metal transition induced by an applied electric field in the 4*d*-electron Mott insulator $Ca_2RuO_4$ was investigated by oxygen 1*s* absorption and emission spectroscopy using synchrotron radiation x-ray. The field-dependent spectra were measured by taking full advantage of the fluorescence method. The spectral weight shifts caused by the field were observed both in the first two peaks of the absorption spectra and in the emission spectra. These results can be attributed to changes in the bonding between the Ru 4*d* and the surrounding O 2*p* orbitals, which was also confirmed consistently by recent theoretical band calculations.

KEYWORDS: $Ca_2RuO_4$, I-M transition, x-ray absorption and emission spectroscopy

The transport properties of strongly correlated electron systems have attracted much interest, such as for exotic superconductivity in $Sr_2RuO_4$[1,2] and the insulator-metal (I-M) transition in $Ca_2RuO_4$.[3,4] The latter is induced by increasing temperature[5,6] or by applying pressure,[7] and is accompanied by an isomorphic transition from *S-Pbca* to *L-Pbca*.[8] Recently, the electric field was found to be another driving force for the same I-M transition.[9,10] Okazaki *et al*. confirmed that the I-M transition was induced by a change in the current, even though there was Joule heating from the temperature dependence of the resistivity as determined using a non-contact infrared thermometer.[10] A dry-cell battery voltage of 1 V is sufficient to induce this transition, which could be applicable to a low power consumption device.

From an electronic point of view, the I-M transition of $Ca_2RuO_4$ is the change in the occupation and energy levels of the three nearly degenerate Ru 4*d* $t_{2g}$ orbitals ($d_{xy}$, $d_{yz}$, and $d_{zx}$). In the insulator phase, two of the four 4*d* electrons occupy the lowest lying $d_{xy}$ orbital due to the rather short *c*-axis in the *S-Pbca* phase within the framework of a crystal field model.[11,12] On the other hand, in the metallic phase, the energy level of $d_{xy}$ to $d_{yz}/d_{zx}$ is inverted because of the elongation of the *c*-axis in the *L-Pbca* phase. As a result, a hole is created in the $d_{xy}$ state, which leads to two-dimensional conductivity.

A redistribution of the *d* electrons at the I-M transition accompanied by the structural change is nicely demonstrated by Mizokawa *et al*. on the basis of temperature- and angular-dependent x-ray absorption spectroscopy (XAS) at the O *K*-edge.[13–15] Taking into account the difference in the angular dependence between the apical O 2*p*-Ru 4*d* $t_{2g}$ bonding and in-plane O 2*p*-Ru 4*d* $t_{2g}$ bonding, the spectral weight-transfer within the two $pd\pi^*$ states can be elucidated by the change in the number of *holes* in the $d_{xy}$ and $d_{yz/zx}$ states, which are denoted as $n_{xy}$ and $n_{yz/zx}$, respectively, from here on.

Similar changes in $n_{xy}$ and $n_{yz/zx}$ are expected for the electric field-induced I-M transition. The total electron yield method commonly used for XAS measurements in the soft x-ray region is, however, inapplicable to an electric field-dependent XAS measurement because of the deflection of electrons. In this study, we therefore employed the partial fluorescence yield method for XAS measurements (PFY-XAS) using a soft x-ray spectrometer, which was also applied to observe O *K*-edge x-ray emission spectra (XES).[16] The O *K*-XES provides information about the $pd\pi$ states which are the counterparts of the $pd\pi^*$ states. The complementary XAS and XES measurements can give insights into the electronic transport properties of $Ca_2RuO_4$.

A single crystal of $Ca_2RuO_4$ was grown by the floating-zone method with the $RuO_2$ self-flux using a commercial infrared furnace (Canon Machinery, SC-M15HD). A plate-shaped crystal with a (001) plane was obtained by self-cleavage during the cooling procedure, since self-cleavage occurs due to the first order structural transition accompanied by a large distortion at around 350 K. The quality of the sample was checked by x-ray powder diffraction (XRD) and magnetization measurements. No magnetic foreign phase, such as $Ca_3Ru_2O_7$, was detected within the experimental accuracy. The sample dimensions used in this study were about $3\times3\times0.1$ mm$^3$. Gold electrodes were sputtered on both ends of the sample, and twisted gold wires with diameter of 25 $\mu$m were attached to the electrodes using silver epoxy.

Both XAS and XES at the O *K*-edge were measured on the linear undulator beamline 2C at the Photon Factory of the High Energy Accelerator Research Organization (KEK-PF). Here, a varied line spacing plane grating with an averaged groove density of 1000 lines/mm is used to monochromatize the soft x-ray beam.[17] The beam spot size on the sample was 1 mm in diameter and the energy resolution of the incident photon was ca. 0.1 eV. The spectrometer used for the PFY-XAS and XES measurements was installed at the end of the beamline. The base pressure of the chamber was on the order of $10^{-6}$ Pa. The angle between the incident and emitted x-rays (scattering angle) was fixed at 90°. The x-ray incident angle during the electric field-dependent measurements was 45°

*E-mail: nobuo@hiroshima-u.ac.jp

with the polarization vector lying in the *ab* plane. This is the polarized configuration in which the emitted photon contains the same polarization vector as that of incident photons.[18] The scattered x-rays were monochromatized with a grating that had a groove density of 1200 lines/mm and their energy resolution was ca. 0.5 eV. The O $2p$-$1s$ fluorescence (O $K\alpha$) was then collected using a 2-dimensional multichannel detector. PFY-XAS spectra were obtained by changing the incident photon energy $h\nu$ from 522 to 565 eV, while the XES spectra were obtained with $h\nu$ fixed at 536.1 eV. The incident angle-dependent XAS spectra were measured both in the polarized and depolarized configurations as shown in the insets of Fig. 3.[18] It should be noted that the relation between the polarization vector of the incident photon and the crystal axes is more important rather than the configuration of the polarization in our study.

The voltage-current (V-I) characteristics were measured *in situ* during the spectroscopic measurements with a two-probe method using a DC voltage-current source/monitor (ADVANTEST, TR6143). A 100 Ω load resistance was connected in series to prevent short-circuit damage at the I-M transition. The electric field was applied parallel to the *ab* plane. For each V-I condition, approximately 1.5 hours were required to obtain one set of XAS and XES spectra, and therefore, the current-control mode was used to ensure long-term stabilization.

Figure 1 shows the *in situ* V-I characteristics of the sample. The open squares denote the points at which the spectra were measured. The V-I characteristics can be divided into three regimes: a high-resistive insulator state (phase I), a transient insulator-metal coexisting state (phase II), and a low-resistive metallic state (phase III). The resistance of the sample was initially 500 Ω at 0 V (0 mA), and it retained the order of the magnitude in phase I.

After the first transition point (1.07 V, 10 mA), the sample resistance rapidly decreased down to several Ω indicating the so-called negative differential resistance in phase II. Voltage and current values at each measurement point were stable, however, extreme care was required during the operation between the points. It should be noted that the joule heat generated at the sample is rather diminishing due to the rapid decrease in the sample resistance in this phase. This ensures that the spectral changes observed by us were electric-field induced ones.

Above the threshold current of 90 mA, the sample undergoes several transitions with discontinuous jumps in the V-I characteristics. The sample resistance in phase III was on the order of 10 Ω. The discontinuities in the graph are due to the cracks in the sample caused by sudden and irreversible elongation along the *c*-axis, which was checked by XRD measurements. The apparent resistance of the sample seems to be slightly larger than that in phase II. This is mainly due to the contact resistance between the fractured layers within the sample, even though each layer is metallic.

All the spectra are shown in Fig. 2. The rainbow-color represents the order of six current conditions from 0 mA, 0 V (black) to 100 mA, 0.8 V (red). The O *K* XAS are normalized to unity at the peak maximum of 533.4 eV, while the O $K\alpha$ XES are area-normalized to a comparable scale. We first explain the XAS results. The overall features are the same as in the experimental[14,15] and theoretical data[19] reported previously by other researchers. The structures from 528 to 530 eV (labeled as A and B) and that from 531 to 534 eV (labeled as C and D) are assigned to transitions from the O $1s$ core level to the O $2p$ orbitals hybridized with the unoccupied Ru $4d$ $t_{2g}$ and $e_g$ states, respectively. From a molecular orbital point of view, these hybridized states can be considered to be $pd\pi^*$ and $pd\sigma^*$ states.[20] Furthermore, Mizokawa *et al*. concluded from their angle-dependent XAS results that the peaks A, B and the peaks C, D are due to hybridization between the apical and planer oxygen sites, respectively. Clear electric-field dependence is found in the $t_{2g}$-derived region. The spectral weight gradually shifted from peak A to B with increasing current amplitude. A similar spectral-weight shift was also observed by temperature variation from 90 to 300 K, accompanied by 2.5% elongation of the *c*-axis[13] similar to our results.

The assignment of the peaks was also verified by us. Figure 3 shows the incidence-angle ($\theta$) dependence of the O *K* XAS observed in the (a) polarized and (b) depolarized configura-

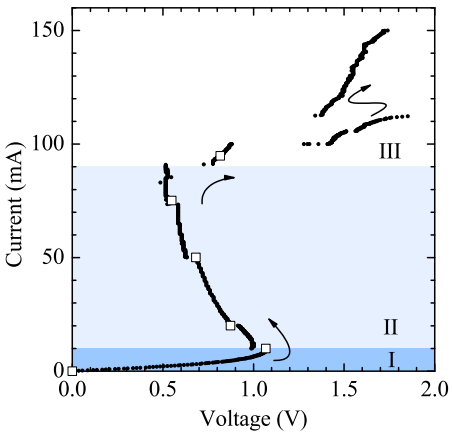


**Fig. 1.** *In situ* V-I characteristics of the sample. The open squares denote the points at which XAS and XES spectra were measured. The characteristic curve is divided into three regimes: an insulator phase I, a transient phase II, and a metallic phase III.

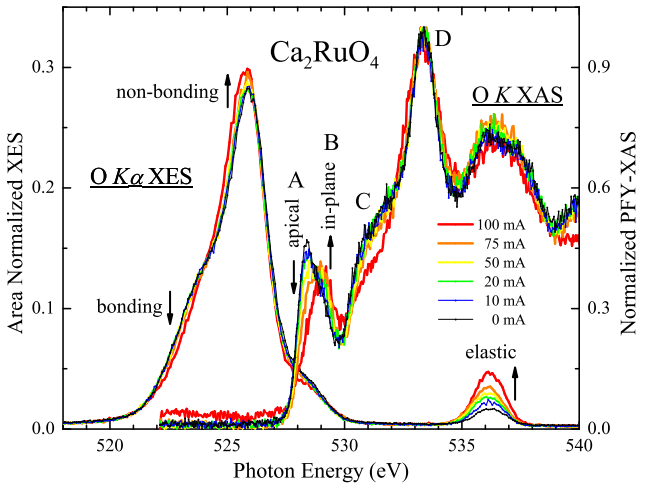


**Fig. 2.** O $1s$ x-ray absorption and emission spectra of $Ca_2RuO_4$ under various current conditions from 0 mA (black) to 100 mA (red). The resonant photon energy of the XES spectra is tuned to 536.1 eV, as evidenced by the elastic-peak energy. The arrows indicate the current-induced variations of each peak.

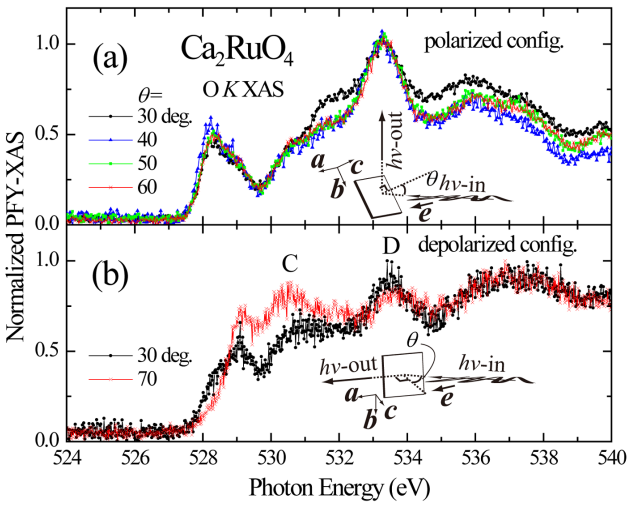


**Fig. 3.** Incident angle ($\theta$) dependence of the O 1$s$ XAS spectra of $Ca_2RuO_4$ taken in the (a) polarized and (b) depolarized configurations. In the former (latter) configuration, the polarization vector $\boldsymbol{e}$ lies in the $ab$ ($ac$) plane, as shown in the illustrations. The labels C and D are identical to those in Fig. 2.

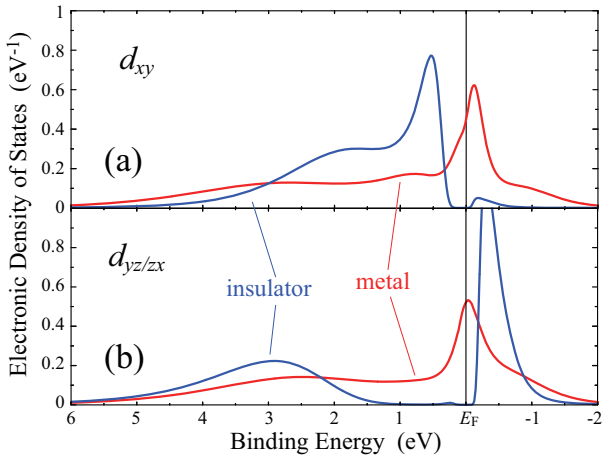


**Fig. 4.** Electronic densities of the (a) $d_{xy}$ state and (b) $d_{yz/zx}$ state obtained from the dynamical mean-field theory by Karolak *et al*. The red (blue) lines are for the metallic (insulator) phase. The origin of the energy is the Fermi level ($E_F$). The original data are presented in Fig. 11 in Ref. 23.

tions. In the former configuration, the unoccupied O 2$p$ final state in the dipole-transition lies along the $a$-axis and is unchanged regardless of $\theta$, therefore slight $\theta$ dependence is observed. On the other hand, in the latter configuration, a clear $\theta$ dependence is observed. The polarization vector of the incident photon ($\boldsymbol{e}$) lies in the $ac$-plane in this configuration: $\boldsymbol{e} \parallel a$-axis at $\theta = 0°$ (normal incidence) and $\boldsymbol{e} \parallel c$-axis at $\theta = 90°$ (grazing incidence). In the normal (grazing) incidence regime, the in-plane (apical) oxygen sites are preferably detected in the $pd\sigma^*$ region, which results in the enhancement of the relative intensity of the D (C) peak as observed in the present study. This trend, together with the $\theta$ dependence of peaks A and B, is the same as that previously reported by Mizokawa *et al*.[13)]

We next discuss the field-dependent XES results in Fig. 2. The elastic peak energy of 536.1 eV corresponds to the 5th peak in the XAS spectra. A broad fluorescence feature is common to other inorganic oxides.[21,22)] The main intense peak at 526 eV can be assigned to the de-excitation from the non-bonding O 2$p$ states, and the shoulder at 523 eV can be assigned to the bonding ones. Again, six spectra are displayed with colors corresponding to the current amplitude of the XAS spectra. A gradual increase in the elastic peak by current is apparent, directly indicating the increase in reflectivity. This is consistent with the V-I characteristics in Fig. 1 wherein a gradual increase of the metallic phase is evident. Even more important changes induced by current in the spectra are the decrease/increase of the bonding/non-bonding peaks, as well as a faint decrease of the bump structure at 527 eV. A key factor for the changes in the spectral weight is the elongation of the $c$-axis, because the bonding between apical O 2$p$ states with the Ru 4$d$ states is weakened. Compared to the XAS spectra, the XES spectral width is large due to the short lifetime of the O 1$s$ core hole, therefore the contribution of the in-plane and apical oxygen is not separated, unlike the XAS case. The presence of the core hole also prevents us from estimating the band-gap of $Ca_2RuO_4$, since the final state of the XAS process contains a core hole and then its energy level is pulled down.

Finally, the electric-field induced spectral weight shifts in the spectra are considered with regard to the number of holes, $n_{xy}$ and $n_{yz/zx}$. The shift from peak A to B observed in the XAS corresponds to an increase of $n_{xy}$. Mizokawa *et al*. roughly estimated that the $n_{xy}/n_{yz/zx}$ ratio increases from 1/3 to 1 from their temperature dependence experiment.[13)] The amount of the spectral weight shift is quite similar in both the temperature variation from 90°C to 300°C and the electric field application in the present study. We can conclude that the electric field induces the structural phase transition followed by an increase in $n_{xy}$, or vice versa.

The drastic increase in $n_{xy}$ is nicely illustrated by the recent theoretical calculation based on the dynamical mean-field theory.[23)] Figure 4 shows the energy dependence of the electronic densities of the (a) $d_{xy}$ state and (b) $d_{yz/zx}$ state. Each line is reproduced from the original figure 11 in Ref. 23. The main peak of the $d_{xy}$ state locates below the Fermi level at the binding energy ($E_B$) of 0.5 eV in the insulator phase, while it shifts upward across the Fermi level in the metallic phase, leading to an increase in $n_{xy}$.

Also presented in this figure is the decrease in the occupied density of the $d_{xy}$ state at binding eneries ranging from 1 to 3 eV through the I-M transition. Besides, the occupied density of the $d_{yz/zx}$ state is broadened, which have peaks at $E_B$=3 eV in the insulator phase (Fig. 4(b)). The decrease and broadening of the Ru 4$d$ occupied states results in an increase of the O 2$p$ occupied states, if the number of valence electrons is conserved. This corresponds to an increase in the non-bonding peak in XES through the I-M transition. The decrease of the bonding peak in XES can also be explained by the decrease in the occupied density of the $d_{yz/zx}$ states. The orbital character of the valence band, as concluded from the XES results, is consistent with that deduced from the valence band photoemission spectra.[13)]

The O $K$-edge XAS and XES of $Ca_2RuO_4$ were measured under a DC applied field in order to investigate the changes in the valence and conduction bands through the I-M transition. Spectral weight shifts were observed in both series of spec-

tra. The changes in XAS can be comprehended as an increase in $d_{xy}$ holes ($n_{xy}$) though metallization, which is consistently understood by the model used to explain the temperature-dependence in XAS. The enhancement in the non-bonding peak in XES can be simply understood by the weakening of the O 2*p*-Ru 4*d* hybridization caused by the elongation of the *c*-axis through the I-M transition. In addition, not only the enhancement of the non-bonding peak but also the increase of $n_{xy}$ is nicely elucidated by the recent theoretical band calculation.

**Acknowledgments** We thank Dr. A. Tanaka of Hiroshima University for his valuable comments and suggestions. The staff of the Photon Factory are acknowledged for their assistance with machine operation. This work was performed under the approval of the Photon Factory Program Advisory Committee (PF-PAC; Contract Nos. 2008G626 and 2010G535). A part of this work was financially supported by JSPS KAKENHI Grant Number 22540368.

1) Y. Maeno, H. Hashimoto, K. Yoshida, S. Nishizaki, T. Fujita, J. G. Bednorz, and F. Lichtenberg, Nature **372** (1994) 532.
2) A. P. Mackenzie, R. K. Haselwimmer, A. W. Tyler, G. G. Lonzarich, Y. Mori, S. Nishizaki, and Y. Maeno, Phys. Rev. Lett. **80** (1998) 161.
3) S. Nakatsuji, S. Ikeda, and Y. Maeno, Phys. Soc. Jpn. **66** (1997) 1868.
4) S. Nakatsuji and Y. Maeno, J. Solid State Chem. **156** (2001) 26.
5) M. Braden, G. Andre, S. Nakatsuji, and Y. Maeno, Phys. Rev. B **58** (1998) 847.
6) C. S. Alexander, G. Cao, V. Dobrosavljevic, S. McCall, J. E. Crow, E. Lochner, and R. P. Guertin. Phys. Rev. B **60** (1999) R8422.
7) F. Nakamura, T. Goto, M. Ito, T. Fujita, S. Nakatsuji, H. Fukazawa, Y. Maeno, P. Alireza, D. Forsythe, and S. R. Julian, Phys. Rev. B **65** (2002) 220402(R).
8) P. Steffens, O. Friedt, P. Alireza, W. G. Marshall, W. Schmidt, F. Nakamura, S. Nakatsuji, Y. Maeno, R. Lengsdorf, M. M. Abd-Elmeguid, and M. Braden. Phys. Rev. B **72** (2005) 094104.
9) F. Nakamura, T. Takemoto, M. Sakaki, and Y. Yamauchi, Japan Patent Kokai P2010-166039A (2010.07.29).
10) R. Okazaki (private communication); see also R. Okazaki, Y. Nishina, Y. Yasui, I. Terasaki, F. Nakamura, Y. Kimura, M. Sakaki, and T. Suzuki, Am. Phys. Soc., APS March Meeting 2012, abstract H9.001.
11) E. Gorelov, M. Karolak, T. O. Wehling, F. Lechermann, A. I. Lichtenstein, and E. Pavarini, Phys. Rev. Lett. **104** (2010) 226401.
12) L. M. Woods, Phys. Rev. B **62** (2000) 7833.
13) T. Mizokawa, L. H. Tjeng, G. A. Sawatzky, G. Ghiringhelli, O. Tjernberg, N. B. Brookes, H. Fukazawa, S. Nakatsuji, and Y. Maeno, Phys. Rev. Lett. **87** (2001) 077202.
14) T. Mizokawa. New J. Phys. **6** (2004) 169.
15) T. Mizokawa, L. H. Tjeng, H.-J. Lin, C. T. Chen, S. Schuppler, S. Nakatsuji, H. Fukazawa, and Y. Maeno, Phys. Rev. B **69** (2004) 132410.
16) Y. Harada, H. Ishii, M. Fujisawa, Y. Tezuka, S. Shin, M. Watanabe, Y. Kitajima, and A. Yagishita, J. Synch. Rad. **5** (1998) 1013.
17) M. Watanabe, A. Toyoshima, Y. Azuma, T. Hayashi, Y. Yan, and A. Yagishita, Proc. SPIE **3150** (1997) 58.
18) Concerning the configuration of the polarization vectors of the incident and emitted photons, see also the figure 1 in Ref. 16.
19) H.-J. Noh, S.-J. Oh, B.-G. Park, J.-H. Park, J.-Y. Kim, T. Mizokawa, L. H. Tjeng, H.-J. Lin, C. T. Chen, S. Schuppler, S. Nakatsuji, H. Fukazawa, and Y.Maeno, Phys. Rev. B **72** (2005) 052411.
20) J. H. Jung, Z. Fang, J. P. He, Y. Kaneko, Y. Okimoto, and Y. Tokura, Phys. Rev. Lett. **91** (2003) 056403.
21) N. Nakajima, M. Deguchi, H. Maruyama, K. Ishiji, and Y. Tezuka, Jpn. J. Appl. Phys. **49** (2010) 09ME04.
22) E. Z. Kurmaev, R. G, Wilks, A. Moewes, L. D. Finkelstein, S. N. Shamin, and J. Kuneš, Phys. Rev. B **77** (2008) 165127.
23) M. Karolak, T. O. Wehling, F. Lechermann, and A. I. Lichtenstein, J. Phys. Condens. Matter. **23** (2011) 085601.

SCIENTIFIC REPORTS

OPEN

SUBJECT AREAS:
APPLIED PHYSICS
ELECTRONIC PROPERTIES AND MATERIALS
ELECTRONIC AND SPINTRONIC DEVICES
ELECTRONIC DEVICES

Received
6 March 2013

Accepted
14 August 2013

Published
29 August 2013

Correspondence and requests for materials should be addressed to F.N. (fumihiko@hiroshima-u.ac.jp)

# Electric-field-induced metal maintained by current of the Mott insulator $Ca_2RuO_4$

Fumihiko Nakamura[1], Mariko Sakaki[1], Yuya Yamanaka[1], Sho Tamaru[1], Takashi Suzuki[1] & Yoshiteru Maeno[2]

[1]ADSM, Hiroshima University, Higashi-Hiroshima 739–8530, Japan, [2]Department of Physics, Kyoto University, Kyoto 606–8502, Japan.

**Recently, "application of electric field (*E*-field)" has received considerable attention as a new method to induce novel quantum phenomena since application of *E*-field can tune the electronic states directly with obvious scientific and industrial advantages over other turning methods. However, *E*-field-induced Mott transitions are rare and typically require high *E*-field and low temperature. Here we report that the multiband Mott insulator $Ca_2RuO_4$ shows unique insulator-metal switching induced by applying a dry-battery level voltage at room temperature. The threshold field $E_{th}$ ~40 V/cm is much weaker than the Mott gap energy. Moreover, the switching is accompanied by a bulk structural transition. Perhaps the most peculiar of the present findings is that the induced metal can be maintained to low temperature by a weak current.**

In the last few decades, there has been growing interest in developing energy-saving devices based on novel quantum phenomena. In particular, the Mott transition is one of the most attractive many-body effects[1]. Pressure (*P*) is a suitable tuning method to explore such novel phenomena; however, high-*P* conditions are generally achieved in a complicated apparatus requiring sophisticated skills. In contrast, there has been growing recognition of applying *E*-field as a complementary method to *P*, since an insulator-metal switching, namely controlling *E*-field, has many advantages for practical use, especially for electronic devices. Moreover, application of *E*-fields can govern the electronic states directly whereas *P* tunes the electronic states indirectly via the change of lattice parameters.

Let us mention two well-known examples of *E*-field-induced phenomena. One is "electrostatic carrier doping" (ESD)[2,3], which controls carrier density in a surface region of an insulator by an extremely large electric field. Indeed, *E*-field-induced superconductivity has recently been reported in the surface layer of a band insulator $SrTiO_3$ by the *E*-field application of 20 kV/cm[4,5]. The other is a Mott transition induced by applying *E*-fields, namely, "switching". Some transition-metal oxides in strongly correlated electron systems have gained attention as a candidate for the switching to practical use as an electronic device such as resistance RAM[6,7]. Most of these previously reported switching phenomena have been achieved only at low temperatures and/or high voltage (typically 1–100 kV/cm)[8–12]. In order to develop energy saving devices, it is essential to find a switching system driven at room temperature (RT) and by weak *E*-fields. An example is the metal-insulator-transition (MIT) induced above room temperature in films of a Mott insulator $VO_2$[8]. It would be desirable to find a system in which bulk metallic state is induced by electric switching with low *E*-field.

As another challenge, it is desirable to maintain the *E*-field-induced metallic state in a "volatile" switching system on cooling and identify interesting ground states, since there have been few such reports in a system stabilising a steady but nonequilibrium state.

We have devoted considerable efforts on the Mott insulator $Ca_2RuO_4$ (CRO) to induce switching and explore its ground state because CRO has the following versatile properties. Firstly, pressurised CRO displays a variety of quantum states, ranging from an antiferromagnetic (AFM) Mott insulator to superconductivity via a ferromagnetic (FM) quasi-two-dimensional metal[13–15]. Secondly, the magnetic and electronic properties of CRO are known to be quite sensitive to coupling of spin, charge and the orbital degrees of freedom[16,17]. Lastly, the metalisation of the Mott insulator CRO can be achieved by heating above $T_{MIT}$ = 357 K[18].

The gap energy in CRO is 0.2 eV determined from the activation energy based on the temperature (*T*) dependence of resistivity[19]. On the basis of a simple Zener breakdown model[20] we estimate $E_{th}$ for CRO to be ~4 MV/cm (we use here the in-plane lattice spacing of $a$ = 5.45 Å. Since $E_F$ has been unknown for CRO, the Fermi energy of $E_F$ ~0.2 eV for the $\gamma$ band of $Sr_2RuO_4$ from ref. 21).

## Results

To investigate the switching phenomena, voltage-current (*V-I*) curves have been measured by using a two-probe method for CRO single crystals. Let us first present the results of *V*-biased experiments. Figure 1 (a) shows changes in *I* at 295 K as a function of *V*. With increasing *V* along the *c* axis, *I* first rises linearly at a rate indicating nonmetallic conduction of ~60 Ωcm, but then jumps discontinuously from 18 to 700 mA at 0.8 V, indicating switching, and is followed by an increase at a rate indicating metallic conduction of ~0.4 Ωcm. Surprisingly, the threshold value $E_{th} \sim 40$ V/cm for $E_{||c}$ is far smaller than our expectation of ~4 MV/cm. We typically obtained $E_{th} \sim 50$ V/cm for $E_{\perp c}$. Thus, the value of the $E_{th}$ is almost independent of the *E*-field direction.

With reducing *V*, *I* decreases with the metallic slope. However, *I* vanishes abruptly at ~10 V/cm because the sample breaks into pieces (single crystalline CRO disintegrates not in the process of the insulator-to-metal transition but in the metal-to-insulator transition. Thus, the *E*-field induced disintegration occurs only in the decreasing *V* process at $E < E_{th}$). Until this disintegration occurs, the *V-I* curves show a large hysteresis indicating a first order Mott transition[22,23] during *V* sweeps.

We show that simple Joule heating is negligible from the following three pieces of experimental evidence: Firstly, there was no appreciable change in *T* of the sample during *V* sweeps; secondly, the switching is also induced by applying only one tiny electric pulse such as $V_{th} \sim 6$ V and $I \sim 20$ mA for the duration of 100 ms. In this switching, the total power of ~12 mJ is fed into a sample in contact with a heat bath. Even if the sample absorbs all the heat, the possible *T* rise of the sample (2.5 mg) is less than ~7 K. Thus, the actual *T* should remain much less than $T_{MIT} = 357$ K. Lastly, the *IV* curves obtained for different duration time are shown in Fig. 1(b) in order to characterize the amount of heat needed to induce switching. Total heating $Q_{th}$ at a threshold point is plotted as a function of the duration time in Fig. 1(c). $Q_{th}$ rises almost linearly with the duration time, in sharp contrast to constant $Q_{th}$ expected for a heating-dominated case. Thus, our switching phenomena cannot be interpreted in terms of a Joule heating.

From the *V-I* curves, we obtained the threshold values $E_{th}$ at several temperatures below 320 K. Figure 1(d) shows the $E_{th}$ divided by $E_0$, the extrapolated value of the $E_{th}$ to absolute zero, plotted as a function *T*. The $E_{th}$ rises on cooling. The linear relation in a logarithmic scale is characteristic of *T* variation of the $E_{th}$. The linear line is a fit with a formula of $E_{th}(T)/E_0 = \exp(-T/T_0)$, using the characteristic values $E_0 = 80$ kV/cm and $T_0 = 39.2$ K.

We, next, consider whether the switching in CRO occurs in local or in bulk. As discussed in the development of switching into the

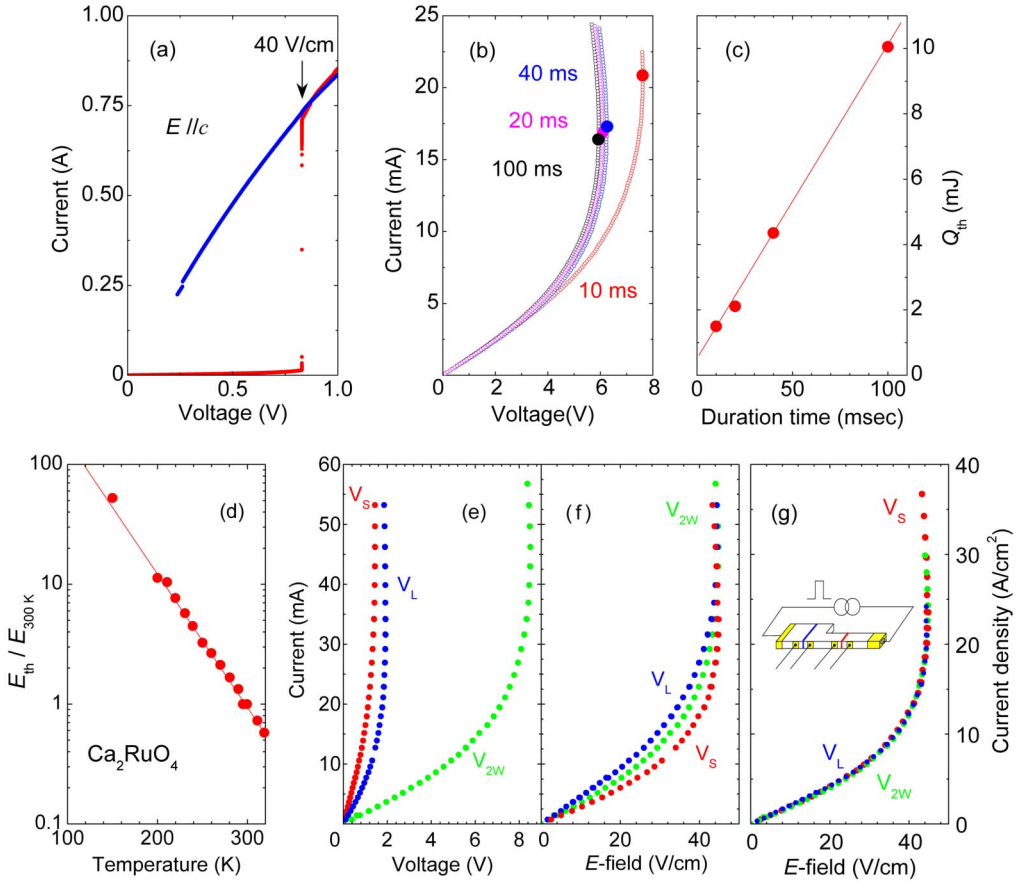


**Figure 1 | Switching in voltage-current curves for $Ca_2RuO_4$.** (a) The voltage-current curves obtained by a two terminal method with continuous $E_{||}c$ at 295 K. There exists a large hysteresis during the voltage sweeps. (b) The switching curves for pulse application $E_{\perp}c$ with a different duration time. The threshold $V_{th}$ and $I_{th}$ are defined from the maximum voltage in the *IV* curve. (c) Total heating $Q_{th}$ at the switching threshold estimated by $Q_{th} = \int V_{th}(t)\, I_{th}(t)\, dt$ in an adiabatic model plotted as a function of duration time. The almost linear increase of $Q_{th}$ with duration time gives clear evidence that the switching is not dominated by heating. The solid line is guide for the eye. (d) $E_{th}$ below 320 K plotted as a function of *T*. The solid line is a fit with $E_{th}(T)/E_0 = \exp(-T/T_0)$, using the characteristic values $E_0 = 80$ kV/cm and $T_0 = 39.2$ K. (e, f, g) The voltage-current curves measured by using a four-probe method for a step-shaped sample consisting of different cross-sectional areas. The schematic view of the step-shape sample is shown in the inset. The current are plotted against (e) voltage and (f) *E*-field. (g) The current density plotted as a function of *E*-field, showing that all the switching curves agree with each other.

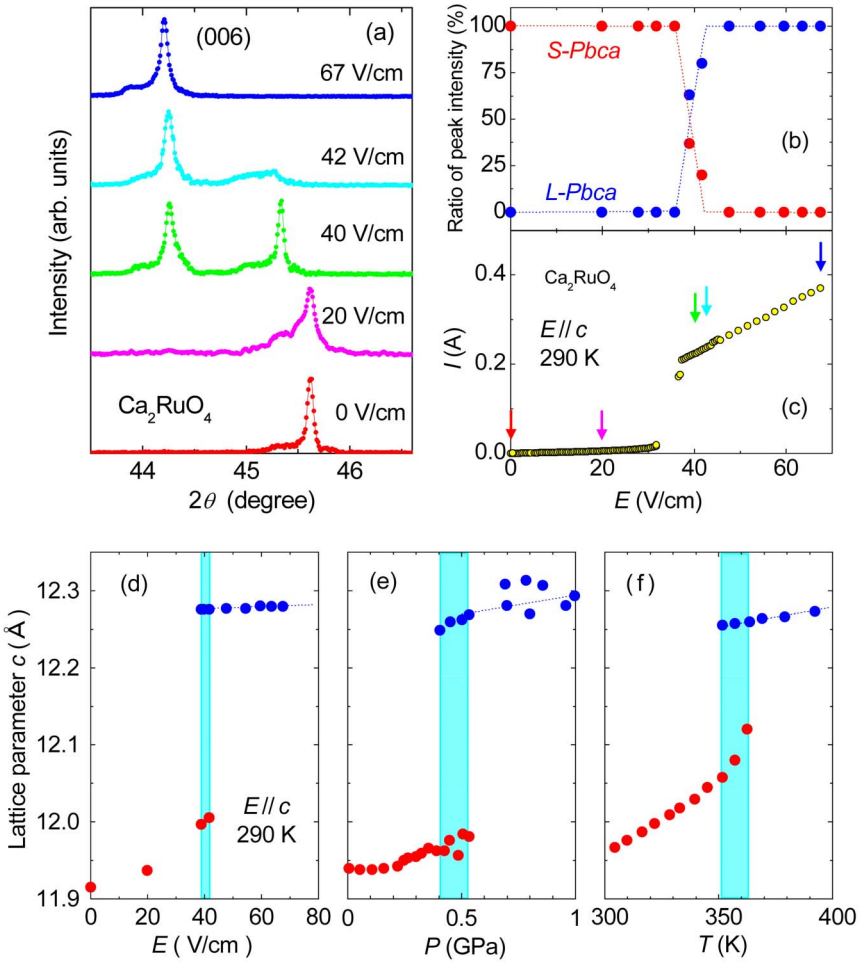


**Figure 2 | An x-ray diffraction study on single-crystalline $Ca_2RuO_4$ in electric fields applied along the *c* axis at 290 K.** (a) Comparison of the diffraction patterns, showing the (006) reflections at representative electric fields. (b) Volume fraction of S and L-Pbca phases plotted as a function of *E*. (c) Switching transition measured simultaneously with the x-ray diffraction. Comparing Fig. 2 (b) with 2 (c), we see that switching occurs prior to the structural transition. (d) Electric-field variation of the lattice parameter *c*. The phase transition from S to L-Pbca phase occurs at $E_{th}$ via the mixed phases (hatched region). (e) Pressure variation of lattice parameter *c*, from P. Stefen *et al.* (ref. 23). (f) Temperature variation of the lattice parameter *c*, from O. Friedt *et al.* (ref. 22).

resistance RAM, many of switching phenomena in insulating oxides have successfully been interpreted in terms of local switching. Two kinds of local-switching models have recently been proposed: one is due to formation of a filamentary path as seen in highly insulating oxides such as NiO[24], and the other is due to interface-resistance switching as seen in relatively conductive perovskite-oxide insulators[25]. In the case that switching occurs locally, the size effect on resistance and threshold voltage should be different from that in a bulk switching case. To inspect this point, we examine the *V-I* curves obtained by using a four-probe method for the samples with different sizes and shapes.

To clarify whether the switching is due to a filamentary path or not, we used single-crystals of CRO formed into a shape with a step with different cross-sectional area. Current is plotted as a function of voltage and *E*-field in Fig. 1 (e) and (f), respectively. In both plots, a difference is visible between large and small cross-sectional area. In contrast, the plots of current density, *J*, against *E*-fields in Fig. 1(g) are universal behavior of the switching in a wide range of *E*-field. From the initial linear slope in the *J-E* curve the resistivity of ~4.7 Ωcm is obtained and agrees well with the resistivity obtained by an ac measurement. Moreover, the value of 4.7 Ωcm indicates that the system is weakly conductive in bulk at RT. Thus, we conclude that the switching in CRO is not due to a filamentary path.

Next, we examine another possibility due to the interface resistance switching. In this case, the switching probability should increase with the area of electrodes because the switching occurs on the interface between a sample and an electrode. We have, however, observed that the resistance and the threshold voltage are almost independent of the area of electrodes. Moreover, the threshold voltage rises linearly with the distance of the electrodes. These clearly indicate that the switching in CRO is not due to interface resistance switching (many of switching phenomena in oxides can successfully be interpreted in terms of diffusion of oxygen defects; however, this model is not suitable for the switching in CRO because CRO does not prefer to produce the oxygen defects).

Now we examine the relation between structure and electronic properties in single-layered ruthenates. It has been known that the electronic phase stability of CRO are governed not simply by the effective correlation energy *U*/*W*, but also by the orbital degeneracy of the $Ru^{4+}$ $t_{2g}$ levels, both of which may abruptly change due to the $RuO_6$-octahedral distortions of flattening, tilt and rotation[22,23]. In particular, the Mott transition is mainly due to the Jahn-Teller effect which produces a change in the orbital occupation associated with the flattening distortion[16].

In pure CRO, the high-*T* ($T > 357$ K) or high-*P* ($P > 0.5$ GPa) metallic phase shows the structure called "L-Pbca", with a weaker

flattening and as well as a weaker tilt and smaller volume than the low-$T$ ($T < 357$ K) or low-$P$ ($P < 0.5$ GPa) insulating phase with the "S-Pbca" structure[22,23]. Thus, it is anticipated that the application of $E$-fields to CRO is accompanied by the structural distortion to release the "flattening" (by the $c$-axis expansion).

To confirm the $E$-field-induced structural transition, we performed x-ray diffraction measurements for single-crystalline CRO in $E_{\|c}$ at 290 K. Figure 2 (a) shows comparison of the diffraction patterns, showing the (006) reflection at representative $E$-fields. The (006) peak at $E = 0$ V/cm observed at 45.62 degree (11.915 Å) indicates that the system is in the stoichiometric S-Pbca insulating phase. In contrast, the application of $E$ turns the system from the S-Pbca phase with the short $c$-axis to the L-Pbca metallic phase with long $c$ (12.276 Å) via a mixed state where the metallic phase coexists with the insulating phase. Since the L-Pbca (006) peak becomes visible at $\sim E_{th}$, the switching is accompanied by a bulk first-order structural transition.

It should be noted that this structural transition is actually visible under a microscope. As evident in the supplemental video, contraction and expansion of a CRO crystal (showing its $ab$ plane) is induced by repeatedly applying "tiny electric pulses" of 25 mJ (100 ms, 8.5 V and 30 mA) at 290 K. This phenomenon may remind us of the piezoelectric effect in ferroelectric crystals but is actually due to the $I$-$M$ switching accompanied by a structural transition. We note that a large current often destroys the samples. However, the switching phenomenon driven by the tiny electric pulses can be stably repeated at least three thousand times. The $E$-field-induced Mott transition thus occurs in the bulk of the sample, not just on the surface or in a filamentary region.

As shown in Fig. 2 (b) and (c), the detailed process of the switching accompanied by a structural transition is obtained by a simultaneous measurement of volume fraction (b) and $I$ (c) as functions of $E$. As seen in this comparison, with increasing $V$ the switching precedes the structural transition. Moreover, the mixed phase persists in the field range from 36 to 48 V/cm. We can, thus, deduce that the bulk metallic region is initially formed along the $E$ direction and then spreads through the whole crystal.

We note that an isovalent substitution of Sr for Ca[26] or pressurisation[13] turns a Mott insulator to a quasi-two-dimensional Fermi-liquid metal without any carrier doping. In these cases, the Mott transition is interpreted in terms of a switching in the orbital occupation driven by the lattice flattening distortion[27]. In contrast, application of an $E$-field itself cannot directly act on the structural distortions, and in fact, the switching occurs prior to the structural transition as indicated by the comparison between Fig. 2(b) and (c).

Let us next compare the lattice parameter $c$ among the $E$-field, $P$, and heating induced structural transitions. Figures 2 (d–f) show the lattice parameter $c$ as functions of $E$-field, $P$, and $T$, respectively. With increasing $E$-field, the lattice parameter $c \sim 11.92$ Å (S-Pbca) gradually increases, and reaches $\sim$12.01 Å at $E_{th} \sim 40$ V/cm, where it abruptly changes to $c \sim 12.28$ Å of the L-Pbca phase in a narrow mixed-phase region. Clearly, there are quantitative similarities among the $E$-field, $P$, and $T$ variations of the $c$ parameter in the vicinity of the Mott transitions.

However, we note here an important difference between the $E$-field and heating induced metallic states. Once the switching occurs, the lattice parameter $c \sim 12.28$ Å remains almost constant in the $E$-field range from 40 to 70 V/cm. In contrast, heating makes the $c$-parameter increase linearly at a rate of $\sim 5 \times 10^{-4}$ Å/K up to $\sim$640 K. This adds further evidence that the $c$-parameter variation in the $E$-field cannot be identified as due to heating.

There remains an absorbing question: what is happening in the $E$-field-induced metallic phase at low temperatures? To the best of our knowledge, there has been no previous example of cooling a volatile switching-system while keeping the metallic state. With the parameters found, it would reach quite a large value, over 100 kV/cm at 4.2 K. In reality, it is extremely difficult to induce a Mott transition by the $E$-field at low temperatures.

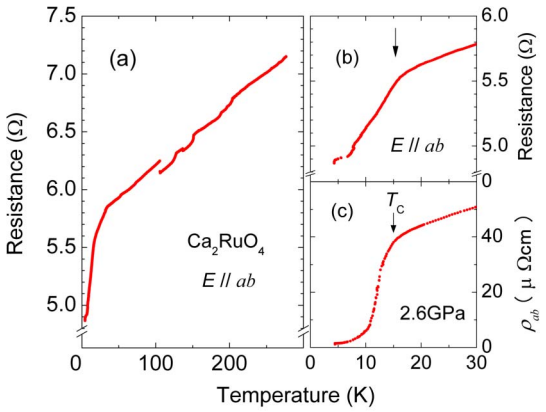


**Figure 3 | Temperature variations of in-plane resistance.** (a) With constant current $I = 420$ mA. (b) Same data as (a) but for $T < 30$ K: The slope of the in-plane resistance in the electric field changes abruptly at $\sim$15 K as indicated by an arrow. (c) In-plane resistivity under $P \sim 2.6$ GPa, for which a similar variation to the $E$-field-induced case is seen at a temperature corresponding to ferromagnetic $T_C$.

Keeping this in mind, let us now present the results of $I$-biased experiments. Figure 3 (a) shows in-plane resistance measured with a constant current of 420 mA by a two-probe method as a function of $T$. Surprisingly, the $T$-variation shows a positive slope ( $d\rho_{ab}/dT > 0$ ) indicating metallic conduction in the $T$ range from 300 to 4.2 K. That is, once the switching has occurred, the $E$-field-induced metallic state becomes stable with flowing current even in $E$-fields much less than $E_{th}$. A heuristic analogy may be drawn with a well-known phenomenon that "flowing" suppresses the freezing point of water.

Figure 3 (b) shows the same data as (a) but for temperatures below 30 K. An abrupt change in the metallic slope at $\sim$15 K is reminiscent of the resistivity change associated with a FM transition in the $P$-induced metallic CRO in Fig. 3 (c). Thus, we naturally anticipate that a FM ordered state appears also in this current-driven metal as a stationary but nonequilibrium state. Indeed, we have observed a change in the local magnetic field with magnetic probes. Although such measurements are technically not easy, they are in progress.

We have experimentally shown that a number of unusual phenomena emerge in the Mott insulator CRO by applications of electric fields and currents. First, the switching is induced by application of such low fields as $E_{th} \sim 40$ V/cm, which is $10^2 \sim 10^3$ times lower than that reported in other Mott insulators. Second, the switching is accompanied by a bulk structural phase transition. Third, the induced metallic phase becomes stable to low temperatures if the flowing bias current is maintained. To add, we also show that under bias current the AFM transition, characteristic of the Mott insulating state of CRO, disappears and moreover FM ordering emerges below 15 K as indicated by the resistance drop as well as the spontaneous magnetization at low temperature.

## Discussion

Now, let us start with a discussion of why CRO shows switching with a structural change. It might seem that switching at a low field is connected with "avalanche breakdown", a dielectric breakdown propagating from a small region of a sample associated with an impurity or surface effect. However, the switching in CRO cannot be understood as such an avalanche breakdown for the following reasons: first, the values of $E_{th}$ indicate good reproducibility, second, the switching characteristics are nearly independent of environmental atmosphere, and last, the switching is accompanied by a bulk structural change.

Among the intrinsic mechanisms, the observed $E_{th} \sim 40$ V/cm is too small to be accounted for by a conventional Zener breakdown model. We should note that in a Mott insulator like CRO, for which conduction is frozen by Coulomb repulsion, unconventional mechanism of dielectric breakdown based on "the many-body Zener effect" is expected to be essential. In fact recent theoretical studies in terms of nonequilibrium processes in highly-correlated electron systems predict that a metallic state is induced at a threshold voltage much smaller than the Mott gap[28]. Such unconventional mechanism may explain relatively small threshold voltage of switching in some Mott insulators even without active orbital degeneracy[8–12].

In addition, orbital depolarization characteristic of a multiband system such as CRO may well be important in further reducing $E_{th}$. Specifically, it is known that in the insulating phase the lower orbital, Ru-$d_{xy}$, is fully occupied and the other bands, derived from the $d_{xz}$ and $d_{yz}$ orbitals, are half-filled, whereas in the metallic phase more electrons in the $d_{xz}$ and $d_{yz}$ lead to full orbital depolarisation. Such orbital depolarisation is strongly coupled to the structural transition. Due to the availability of this self-doping mechanism associated with spatial charge redistribution, the application of $E$-field may further enhance the electronic instability driven by the many-body Zener effect.

Here, we should also mention that the formula which describes the observed threshold energy to induce the metallic state, $E_{th}(T)/E_0 = \exp(-T/T_0)$, is often used for CDW systems and interpreted in terms of weakening of the pinning potential[11,29]. This formula is importantly different from that for a thermal activation process, $E_{th}(T)/E_0 = \exp(T_0/T)$ and explains why $E_{th}$ is much smaller than the Mott gap at RT and why the $E$-field induced metal is maintained by current, in terms of delocalisation of carriers. A charge depinning process deduced from the observed behaviour suggests that the switching phenomena may be related to a ferro-type orbital ordering in the insulating phase[30], expected to be accompanied by charge localisation.

Lastly, it should be emphasized that the "flowing current" plays a key role in maintaining the induced metallic state, although the switching itself is induced not by the application of current but voltage. This phenomenon is truly unexpected and most probably requires a mechanism of stabilising a steady but nonequilibrium state (current maintained metal) over an equilibrium state (Mott insulator). Thus, application of $E$-fields and/or flowing currents has a great potential as a new tool to induce novel quantum phenomena in a variety of materials. Utilising such nonequilibrium states will certainly help expanding our knowledge of material science[31,32].

## Methods

Single crystals of CRO were grown by a floating-zone method with $RuO_2$ self-flux. We used high quality samples[13–15] with essentially stoichiometric oxygen content judging from the $c$-axis lattice parameter of ~11.92 Å at 290 K and the AFM transition at 113 K. Judging from the $c$-axis lattice parameter before and after switching, there is little change in the oxygen content during our switching experiments. Voltage-current ($V$-$I$) curves have been obtained with a load resistor ($0 \sim 1$ kΩ) connected in series and a dc voltage and current source/monitor (ADVANTEST, model TR6143 and ADCMT, model 6241A). The electrodes were made by gold evaporation on a freshly cleaved surface. The distance between the electrodes is typically 0.2 mm. We monitored a change in $T$ at the sample during voltage sweeps. There exists little evidence for $T$ rise in the $E$ range below $E_{th}$. The resistance have often been measured by using a two-terminal method when there is negligible deference between a two- and a four-terminal one as shown in Fig. 1(e–g).

The x-ray diffraction study was performed for single-crystalline CRO in $E$ applied along the $c$ axis at 295 K. We irradiate the cleaved (001) surface with a ring-shaped electrode with x-ray. The contribution from $CuK\alpha_2$ radiation was analytically subtracted.

We have tried to examine a change in the local magnetic field directly using a superconducting quantum interference device (SQUID) magnetometer as well as a Hall probe. Detailed study is underway to determine the magnetic properties as a function of temperature.


1. Imada, M., Fujimori, A. & Tokura, Y. Metal-insulator transitions. *Rev. Mod. Phys.* **70**, 1039 (1998).
2. Rozenberg, M. J., Inoue, I. H. & Sanchez, M. J. Nonvolatile memory with multilevel switching: A basic model. *Phys. Rev. Lett.* **92**, 178302 (2004).
3. Inoue, I. H. & Rozenberg, M. J. Taming the Mott transition for a novel Mott transistor. *Adv. Funct. Mater.* **18**, 2289 (2008).
4. Reyren, N. *et al.* Superconducting interfaces between insulating oxides. *Science* **317**, 1196 (2007).
5. Ueno, K. *et al.* Electric-field-induced superconductivity in an insulator. *Nature Materials* **7**, 855–858 (2008).
6. Meijer, G. I. Who wins the nonvolatile memory race. *Science,* **319**, 1625 (2008).
7. Waser, R. & Aono, M. Nanoionics-based resistive switching memoriesa. *Nature Materials* **6**, 833 (2007).
8. Kanki, T., Kawatani, K., Takami, H. & Tanaka, H. Direct observation of giant metallic domain evolution driven by electric bias in VO2 thin films on TiO2(001) substrate. *Appl. Phys. Lett.* **101**, 243118 (2012).
9. Iwasa, Y. *et al.* Switching effect in organic charge transfer complex crystals. *Appl. Phys. Lett.* **55**, 2111 (1989).
10. Yamanouchi, S., Taguchi, Y. & Tokura, Y. Dielectric breakdown of the insulating charge-ordered state in $La_{2-x}Sr_xNiO_4$. *Phys. Rev. Lett.* **83**, 5555 (1999).
11. Taguchi, Y., Matsumoto, T. & Tokura, Y. Dielectric breakdown of one-dimensional Mott insulators $Sr_2CuO_3$ and $SrCuO_2$. *Phys. Rev. B* **62**, 7015 (2000).
12. Hatsuda, K., Kimura, T. & Tokura, Y. Electric-field switching of orbital order in layered manganites. *Appl. Phys. Lett.* **83**, 3329 (2003).
13. Nakamura, F. *et al.* From Mott insulator to ferromagnetic metal. a pressure study of $Ca_2RuO_4$. *Phys. Rev. B* **65**, 220402(R) (2002).
14. Nakamura, F. *et al.* Anisotropic giant magnetoresistance near the Mott transition in pressurized $Ca_2RuO_4$. *Phys. Rev. B* **80**, 193103 (2009).
15. Alireza, P. L. *et al.* Evidence of superconductivity on the border of quasi-2D ferromagnetism in $Ca_2RuO_4$ at high pressure. *Journal of Physics: Condensed Matter* **22**, 052202 (2010).
16. Anisimov, V. I., Nekrasov, I. A., Kondakov, D. E., Rice, T. M. & Sigrist, M. Orbital-selective Mott-insulator transition in $Ca_{2-x}Sr_xRuO_4$. *Eur. Phys. J. B* **25**, 191 (2002).
17. Koga, A., Kawakami, N., Rice, T. M. & Sigrist, M. Orbital-selective Mott transitions in the degenerate Hubbard model. *Phys. Rev. Lett.* **92**, 216402 (2004).
18. Alexander, C. S. *et al.* Destruction of the Mott insulating ground state of $Ca_2RuO_4$ by a structural transition. *Phys. Rev. B* **60**, R8422 (1999).
19. Fukazawa, H. & Maeno, Y. Filling control of the Mott insulator $Ca_2RuO_4$. *J. Phys. Soc. Jpn.* **70**, 460–467 (2001).
20. Zener, C. Non-adiabatic crossing of energy levels. *Proc. Roy. Soc. London. Ser. A* **137**, 696 (1932).
21. Mackenzie, A. P. & Maeno, Y. The superconductivity of $Sr_2RuO_4$ and the physics of spin-triplet pairing. *Rev. Mod. Phys.* **75**, 657 (2003).
22. Friedt, O. *et al.* Structural and magnetic aspects of the metal-insulator transition in $Ca_{2-x}Sr_xRuO_4$. *Phys. Rev. B* **63**, 174432 (2001).
23. Steffens, P. *et al.* High-pressure diffraction studies on $Ca_2RuO_4$. *Phys. Rev. B* **72**, 094104 (2005).
24. Kim, D. C. *et al.* Electrical observations of filamentary conductions for the resistive memory switching in NiO films. *Appl. Phys. Lett.* **88**, 202102 (2006).
25. Sawa, A., Fujii, T., Kawasaki, M. & Tokura, Y. Interface resistance switching at a few nanometer thick perovskite manganite active layers. *Appl. Phys. Lett.* **88**, 232112 (2006).
26. Nakatsuji, S. & Maeno, Y. Quasi-two-dimensional Mott transition system $Ca_{2-x}Sr_xRuO_4$. *Phys. Rev. Lett.* **84**, 2666 (2000).
27. Gorelov, E. *et al.* Nature of the Mott transition in $Ca_2RuO_4$. *Phys. Rev. Lett.* **104**, 226401 (2010).
28. Oka, T. & Aoki, H. Dielectric breakdown in a Mott insulator: Many-body Schwinger-Landau-Zener mechanism studied with a generalized Bethe ansatz. *Phys. Rev. B* **81**, 033103 (2010).
29. Monceau, P., Renard, M., Richard, J., Saint-Lager, M. C. & Wangin, Z. Z. Charge Density Wave in Solids, edited by Hutiray, G. Y. & Solyom, J. (Springer-Verlag, Berlin, 1985).
30. Kubota, M. *et al.* Ferro-Type Orbital State in the Mott Transition System $Ca_{2-x}Sr_xRuO_4$ Studied by the Resonant X-Ray Scattering Interference Technique. *Phys. Rev. Lett.* **95**, 026401 (2005).
31. Sawano, F. *et al.* An organic thyristor. *Nature* **437**, 522–524 (2005).
32. Ajisaka, S., Nishimura, H., Tasaki, S. & Terasaki, I. Nonequilibrium Peierls Transition. *Progress of Theoretical Physics* **121**, 1289–1319 (2009).


## Acknowledgements

We acknowledge T. Takemoto and Y. Kimura for their experimental helps, I. Terasaki and I. H. Inoue for fruitful discussions, and T. Yamagishi, S. Yonezawa at Kyoto University and R. Okazaki at Nagoya University for reproducing the result. They also confirmed that heating is insignificant at $E_{th}$. We also acknowledge S. R. Julian for careful reading of the manuscript. A part of this work has been supported by a Grant-in-Aid for Scientific Research on Priority Areas (Grant No. 20029017 and 22540368) and by a Global COE grant "the Next Generation of Physics, spun from Universality and Emergence" from the MEXT of Japan.

## Author contributions

F.N. planned the experiment and grew the samples. F.N., Y.M., S.T. and Y.Y. measured the electrical transport properties. M.S. and T.S. carried out the X-ray diffraction experiment. F.N. and Y.M. wrote the manuscript with contributions from the other authors.

## Additional information

**Supplementary information** accompanies this paper at http://www.nature.com/scientificreports

**Competing financial interests:** The authors declare no competing financial interests.

**How to cite this article:** Nakamura, F. *et al.* Electric-field-induced metal maintained by current of the Mott insulator $Ca_2RuO_4$. *Sci. Rep.* **3**, 2536; DOI:10.1038/srep02536 (2013).

# 参考論文

(1) Anisotropic giant magnetoresistance near the Mott transition in Pressurized $Ca_2RuO_4$
Fumihiko Nakamura, Ryuji Nakai, Tetsuo Takemoto, Mariko Sakaki, and Takashi Suzuki, Patricia Lebre Alireza, Satoru Nakatsuji, Yoshiteru Maeno
PHYSICAL REVIEW B **80**, 193103 (2009).

(2) Pressure induced novel-phenomena in Mott insulator $Ca_2RuO_4$
Y.Yamauchi, F.Nakamura, M.Sakaki, T.Takemoto, T.Suzuki, P.L.Alireza and Y.Maeno
Physica C**470** (2010) S877

(3) 公開特許 ペロブスカイト型酸化物の相転移誘起方法、電子機能素子材料として用いられているペロブスカイト型酸化物、ペロブスカイト型酸化物を用いた電子機能素子及び電子装置
中村　文彦、竹本　哲雄、坂木　麻里子、山内　洋平
JP 2010-166039 A 2010.7.29

# Anisotropic giant magnetoresistance near the Mott transition in pressurized $Ca_2RuO_4$

Fumihiko Nakamura, Ryuji Nakai, Tetsuo Takemoto, Mariko Sakaki, and Takashi Suzuki
*Department of Quantum Matter, ADSM, Hiroshima University, Higashi-Hiroshima 739-8530, Japan*

Patricia Lebre Alireza
*Cavendish Laboratory, University of Cambridge, JJ Thomson Avenue, CB3 OHE Cambridge, United Kingdom*

Satoru Nakatsuji
*Institute for Solid State Physics, University of Tokyo, Kashiwa 277-8581, Japan*

Yoshiteru Maeno
*Department of Physics, Kyoto University, Kyoto 606-8502, Japan*
(Received 22 June 2009; published 11 November 2009)

We have observed an anisotropic and giant magnetoresistance (MR) in the 4*d*-electron Mott transition system of $Ca_2RuO_4$. On the border of the Mott transition (~2 GPa), the MR effect at ~10 T reaches ~ −55% at $T_C$ for longitudinal and ~+120% at low temperatures for the transverse effects. The negative MR is most likely interpreted as a reduction in a ferromagnetic (FM) fluctuation at $T_C$. In contrast, the large positive effect is actually rare and is characteristic of the mixed state where the FM metallic islands are flecked with the insulating phases. We discuss the reason of the peculiar MR from the viewpoint of the "anisotropic magnetism," the "tunnel MR," and the "orbital physics."

DOI: 10.1103/PhysRevB.80.193103 PACS number(s): 71.30.+h, 75.30.Kz, 74.70.Pq, 74.62.Fj

To explore novel quantum phenomena such as unconventional superconductivity (SC), itinerant magnetism, and large magnetoresistance (MR) effect, is one of the most important and interesting subjects in condensed matter physics.[1] It is known that transition-metal compounds in the vicinity of a Mott transition exhibit a rich variety of quantum phenomena caused by strong coupling with orbital degrees of freedom, charge and spin.[2] As seen in the discovery of anomalous metal such as the high-$T_C$ cuprates and the manganites, there has been a growing interest in the Mott transition, which is known as a dramatic and fundamental many-body effect in itself. Most of the previous work on the Mott transition has been confined to 3*d* transition-metal systems. In particular, there has been growing recognition of a large decrease of MR so-called the colossal magnetoresistance.[3]

In contrast, 4*d* metal-nonmetal systems are actually rare since 4*d* orbitals are generally more extended than 3*d* ones, giving rise naturally to wide bandwidths *W*. Moreover, the orbital angular momentum of 4*d* electron is not entirely quenched.[4] That is, the magnetic and electronic properties are more sensitive to coupling with spin, charge and the orbital degrees of freedom. We thus expect a peculiar Mott transition in 4*d* transition-metal systems. Much attention has been paid for a Mott transition system in ruthenates with perovskite-type structure. In particular, single-layered ruthenates ($Ru^{4+}$ $4d^4$) display versatile quantum phenomena, ranging from an antiferromagnetic (AFM) Mott insulator to a ferromagnetic (FM) metal, as well as SC. As well known, $Sr_2RuO_4$ shows the spin-triplet SC.[5] In contrast, $Ca_2RuO_4$ (CRO), which has a larger $U/W$ than $Sr_2RuO_4$, is a Mott insulator with an AFM ground state.[6] The solid solution system $Ca_{2-x}Sr_xRuO_4$ shows a complex phase diagram with a peculiar Mott transition.[7] Isoelectric substitution of Sr by Ca is, thus, an effective and convenient method to control $U/W$ over a wide range through tuning the $RuO_6$-octahedral distortions of flattening, tilt and rotation.[8] In particular, the Mott-type nonmetal-metal transition is accompanied by a first-order structural transition from S-Pbca with flatted octahedron (Ru-O distance along *c* is shorter than that perpendicular to *c*) into L-Pbca with nonflatted one (Ru-O distance perpendicular to *c* is longer than that along *c*). That is, the nonmetal-metal transition is strongly related to expanding the Ru-O distance along *c*.

In contrast, pressure, *P*, phase diagram is quite unique and different from that of the substituted system. We reported that pressurization of CRO transforms it from an AFM insulator to a quasi-two-dimensional metal with a FM ground state.[9,10] The intrinsic FM ground state thus appears only in the pressurized system. Our magnetization measurements[10] indicate that the FM has several features of an itinerant magnetism:[11] first, $M_{rem} \sim 0.35\mu_B$ at 1.5 GPa is much smaller than the saturated moment of 2 $\mu_B$ of localized $Ru^{4+}$ ion, second, magnetization is not easily saturated with applied magnetic fields up to 5 T, and lastly, a ratio of $p_{eff}/M_{rem} \sim 5$ is much larger than the 1 of localized systems.

Here, noteworthy is that there exists a mixed state in the pressure range $0.5 < P < \sim 2$ GPa where the FM shows itinerant nature in spite of nonmetallic *T* dependence of resistivity.[10] Indeed, two characteristic changes in $\rho_{ab}(T)$ were observed in CRO pressurized from 0.8 to ~2 GPa. First, the metallic $\rho_{ab}$ ($d\rho_{ab}/dT > 0$) jumps discontinuously and then turns into nonmetallic one ($d\rho_{ab}/dT < 0$). With pressurization, the metal-nonmetal transition temperature ($T_{MIT}$) is suppressed, and is killed above ~2 GPa. Second, CRO pressurized above 0.8 GPa shows a drop in $\rho_{ab}(T)$ at around $T_C$ determined by magnetization measurement. Such a drop in $\rho_{ab}(T)$ at $T_C$ is most likely understood as magnetic scattering reduced by a FM ordering. Moreover, our high-*P* diffraction study[12] indicates that the structural phase separa-

 

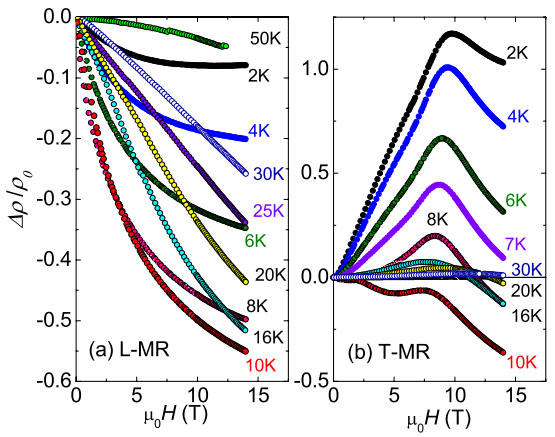


FIG. 1. (Color online) The longitudinal (a) and the transverse (b) MR up to 14 T at 1.9 GPa and several fixed $T$. The L-MR is negative in the whole temperature and field ranges we measured. The T-MR shows a positive MR reaching ~+120% at ~9.5 T and 2 K.

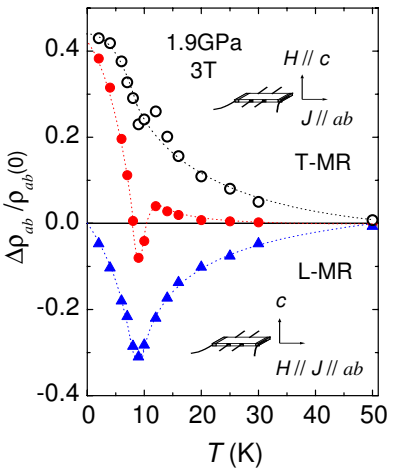


FIG. 2. (Color online) Anisotropic MR at 3 T and 1.9 GPa plotted against $T$, where (blue) triangle is the L-MR, (red) closed circle is the T-MR, open circle is reminder of subtraction of L-MR from T-MR. The dotted lines are guides to the eyes.

tion of L- and S-Pbca has been observed in the vicinity of the Mott transition at ~0.5 GPa.

Single-crystals $Ca_2RuO_4$ with an essentially stoichiometric oxygen content[6] were grown by a floating-zone method. Resistivity was measured by a standard four-probe method under $P$ up to 4 GPa and fields up to 14 T by using a physical properties measurement system (Quantum Design, model PPMS) equipped with a homemade nonmagnetic clamp-piston-cylinder cell. Our $P$ cell uses a compound design with the MP35N alloy inner cylinder and outer sleeve. Pressures were generated with Daphne oil 7243 (Idemitsu Kosan Co., Ltd.) as a $P$-transmitting medium.[13]

We have measured in-plane magnetoresistance MR $\{\Delta\rho_{ab}/\rho_{ab}=[\rho_{ab}(\mu_0 H)-\rho_{ab}(0)]/\rho_{ab}(0)\}$ up to 14 T for CRO pressurized at 1.9 GPa. The longitudinal (L-MR: $J\|\mu_0 H\perp c$) and the transverse MR (T-MR: $J\perp\mu_0 H\|c$) at several fixed temperatures between 50 and 2 K are plotted against magnetic fields in Figs. 1(a) and 1(b), respectively. Application of $\mu_0 H$ up to 14 T enlarges the L-MR negatively and monotonically over the whole $T$ range we measured. On heating from 2 K, the amplitude of the negative L-MR continues to rise from −7% at 2 K and 14 T, reaching a maximum of −55% at 10 K of $T_C$, then it turns to decrease. Moreover, the negative L-MR curve turns from concave to convex one in the vicinity of $T_C\sim 10$ K. It can, thus, be seen that the negative MR effect becomes remarkable at $T_C$.

On the contrary, the $\mu_0 H$ variation in the T-MR is mainly positive but relatively complicated $\mu_0 H$ and $T$ variations. At 2 K, the T-MR rises positively and monotonically, peaking at the maximum of ~+120% in 9.7 T, and then it turns to reduce. We note that the value of ~+120% at 2 K and 1.9 GPa is the largest effect in the $T$ and $P$ ranges we measured. Such a large MR is actually rare among positive than negative effect. With $T$, however, the amplitude of the positive T-MR reduces, and then the sign turns from positive to negative in the vicinity of $T_C$. Above 30 K the amplitude becomes quite small, similar to the L-MR. The characteristic peaks were observed at fields of 9.7, 9.4, 8.9, 8.6, 8.4, and 7.4 T for $T$=2, 4, 6, 7, 8, and 10 K, respectively. Thus, the peak decreases gradually and vanishes suddenly above 10 K of $T_C$. Thus, the peak nature is most probably related to the FM ordering.

In order to display the complicated MR nature intelligibly, the changes of L- and T-MR at 3 T are plotted as a function of $T$ in Fig. 2. With reducing $T$ from 50 K, the L-MR enlarges negatively, reaching a peak of ~−30% in the vicinity of $T_C\sim 10$ K, then it decreases rapidly toward zero at absolute zero. Qualitatively similar $\mu_0 H$ and $T$ variations in L-MR can be seen in a typical FM metal such as nickel in the vicinity of $T_C$.[14,15] This behavior is interpreted in terms of a change in the FM spin fluctuation, which is suppressed in the vicinity of $T_C$ with magnetic fields. We can, therefore, understand the observed nature of L-MR as a typical FM behavior near $T_C$.

In contrast, the T-MR nature, especially $T$ dependence, remains puzzling. On cooling from 50 K, the T-MR increasing positively and weakly dips suddenly into the negative value of ~−8% on the border of $T_C$. Below $T_C$ it rises again toward ~−40% at 2 K.

On the analogy of MR of nickel, the negative dip at $\sim T_C$ appears naturally in both T- and L-MR.[14,15] That is, the dip in the T-MR is most likely due to the same origin as seen in the L-MR. It is generally known that a resistance caused by magnetic scattering obeys the Matthiessen rule; therefore, the T-MR excluding the FM fluctuation effect is obtained after subtraction of the L-MR from the observed T-MR as is shown in Fig. 2 (open circle). We can understand the transverse effect is composed of two independent contributions: the one due to magnetic scattering near $T_C$ and intrinsically positive one.

To obtain further information of the positive effect, we examined the influence of $\mu_0 H\|c$ on the $\rho_{ab}(T)$. Figure 3 shows $\rho_{ab}(T)$ curves in several fixed $\mu_0 H\|c$ at 0.8 GPa. The $\rho_{ab}(T)$ curves show nonmetallic increase below $T_{MIT}$ ~230 K. The zero field $\rho_{ab}(T)$ curve peaks at $T_C\sim 10$ K, then it decreases monotonically as indicating a metal-like dependence. On the contrary, application of $\mu_0 H\|c$ induces a low-$T$ upturn (10 T), and then it kills the metallic decrease (14 T).

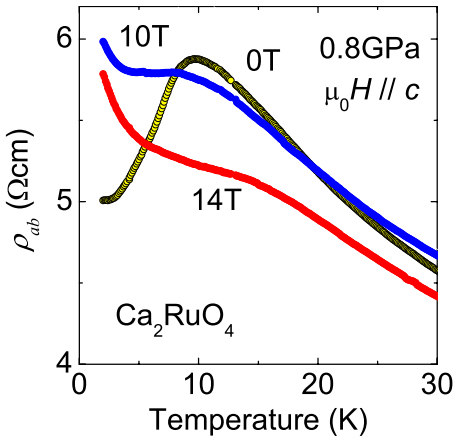


FIG. 3. (Color online) $T$-variation of $\rho_{ab}$ at 0.8 GPa in several fixed $\mu_0 H$ along $c$. The low-$T$ drop in $\rho_{ab}(T)$ is suppressed by applying $\mu_0 H \| c \geq 10$ T.

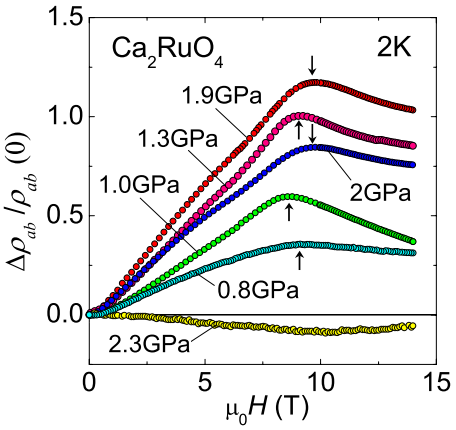


FIG. 4. (Color online) At 2 K the $\rho_{ab}(\mu_0 H \| c)$ (T-MR) measured in several fixed pressures. The T-MR curves below 2.3 GPa peaks at the characteristic fields, which are indicated by allows, are 9.1, 8.7, 9.2, 9.6, and 9.7 T at 0.8, 1, 1.3, 1.8, and 2 GPa, respectively.

Let us consider the reason why application of $\mu_0 H \| c$ only causes the characteristic changes in the resistivity. We infer that the characteristic MR nature is due to a change in the magnetization, namely, the magnetic scattering. Indeed, the characteristic MR has mainly been observed in the FM state only.

Recently we show that the FM moment is strongly anisotropic; that is, the $c$ axis is the hard direction.[11] A comparison of the anisotropic magnetization processes at 2 K and 1.8 GPa gives us $\mu_0 H_A \sim 9.5$ T of the anisotropy field, at which the direction of the spin orientation is forced from the $a$ to the $c$ axis by applying $\mu_0 H \| c$.[16] Here we note that $\mu_0 H_A \sim 9.5$ T corresponds to the peak field of the T-MR. Indeed, a change in MR at $\mu_0 H_A$ has often been reported as a characteristic nature of a ferromagnet. That is, a rotation of FM moment is known as a factor for a change in MR.[17]

In our T-MR case, the current and fields are applied perpendicular and parallel to the hard direction of the $c$ axis, respectively. With applying $\mu_0 H \| c$, the angle between the magnetized and the current directions initially increases, then it becomes a right angle above $\mu_0 H_A$. At $\mu_0 H_A$, such a change in magnetization is naturally reflected in the T-MR. In contrast, the L-MR shows no characteristic change because the application of $\mu_0 H \perp c$ induces no characteristic change in the FM moment. It, thus, can be seen that the anisotropic MR is interpreted in terms of anisotropic magnetization, namely, spin flop induced by fields applied to the hard direction of $c$.

However, there remains a question why the T-MR shows positive and giant MR effect. We can fully expect that our finding of the positive and giant MR effect is interpreted in terms of the tunnel MR effect although there is no direct evidence to confirm this so far. It is known that the tunnel MR effect, which can often cause a large and positive MR, occurs in magnetic tunnel junctions consisting of ferromagnet isolated by thin insulators. Electron tunnelling between the isolated FM islands can occur in the case that the insulating layer is thin enough. Moreover, an angle dependence of MR is known as a characteristic behavior of the tunnel MR.

In the pressurized CRO, the FM metallic phase is induced and enlarged by pressurizing above 0.5 GPa, then it is dominant above 1.5 GPa. Indeed, the linear extrapolation of pressuring the S-Pbca volume fraction vs $P$ suggests that the S-Pbca insulating phase is almost killed by $P \gtrsim 1.5$ GPa. Moreover, pressurization above $\sim$1.5 GPa kills $T_N$ and makes it possible to reach the remnant FM moment as a bulk system (the FM moment is almost constant above $\sim$1.6 GPa), as indicated by our magnetization[10] and $\mu$SR studies.[18] However, the resistivity still shows a nonmetallic $T$ dependence even above $\sim$1.5 GPa. These mean that there exist many of the FM metallic islands separated by the thin insulating layers in the mixed state. Moreover, we can fully expect that the magnetic tunnel junctions are naturally formed in the mixed state.

As shown in Fig. 4, with pressurizing above 0.5 GPa the positive and giant MR effect is initially enlarged, reaching a maximum value of $\sim$+120% at 1.9 GPa, then reduces rapidly and vanishes in the metallic state above $\sim$2.3 GPa. Thus, the positive MR effect is characteristic of in the mixed state. We, therefore, infer that the positive MR is due to the tunnel MR effect, namely the tunnel junctions consisting of the FM metallic islands (L-Pbca) isolated each other by the thin insulating layers (S-Pbca). The tunnel MR effect is actually a strong candidate for the mechanism of the peculiar MR in the mixed state, but it is not enough for full understanding of our observed MR effect.

As another factor enlarging MR, we should discuss the "orbital physics," which is proposed to understand the peculiar properties of Ru214 in the vicinity of Mott transition, specially the "orbital-selective Mott transition."[4,7,19] We focus on two evidences indicating importance of strong coupling with spin, charge, and the orbital degrees of freedom. First, we pay attention to the value of $\mu_0 H_A$, which is known as an indication of spin-orbit coupling. $\mu_0 H_A \sim 9.5$ T is one of the largest values as a $d$ electron ferromagnet. Even for a typical anisotropic ferromagnet of Co with $\mu_0 H_A \sim 1$ T, the orbital angular momentum plays a key role to understand the strong magnetic anisotropy. Thus, importance of the "orbital physics" is demonstrated by the strongly anisotropic ferromagnetism of the pressurized CRO.

Second, we note that the large negative MR is not limited in the mixed state. The negative L-MR reaching $\gtrsim -50\%$ have been observed in the paramagnetic region above $T_C$ and the metallic state above 2.3 GPa. It is known that MR in 3*d* FM metals shows the qualitatively similar $T$ and $\mu_0 H$ dependences, especially negative dip in the vicinity of $T_C$ although the amplitude of MR is a few percent at the most.[14] The amplitude of the MR in CRO is too large to explain in terms of simple magnetic scattering as is the case with 3*d* FM metals. We deduce that the orbital physics, namely strong spin-orbit coupling, amplifies the MR due to magnetic scattering.

We summarize several attractive findings in an anisotropic and giant MR effect in the $P$ induced Mott transition system of CRO as follows: first, the $T$ variation in both T-MR and L-MR shows a negative dip near $T_C$. The dip nature is qualitatively understood as a change in magnetic fluctuation as is also seen in typical FM metals. Second, concern has been paid to the positive T-MR peaking at $\mu_0 H_A \sim 9.5$ T and reaching $\sim +120\%$. Such a giant positive effect, which is actually rare in bulk system, is characteristic of the mixed state; therefore, this is due to the magnetic tunnelling between the FM islands isolated by the thin insulating layers. Lastly, we propose the importance of the orbital physics as another key factor for amplifying the MR effect. Indeed, this is clearly indicated by the largeness of the anisotropy field of 9.5 T.

A part of this work has been supported by a Grant-in-Aid for Scientific Research on Priority Areas (Grant No. 20029017) from the MEXT of Japan.

[1] G. G. Lonzarich, Nat. Phys. **1**, 11 (2005).
[2] For a review, see M. Imada, A. Fujimori, and Y. Tokura, Rev. Mod. Phys. **70**, 1039 (1998).
[3] Y. Tomioka and Y. Tokura, Phys. Rev. B **66**, 104416 (2002).
[4] T. Mizokawa, L. H. Tjeng, G. A. Sawatzky, G. Ghiringhelli, O. Tjernberg, N. B. Brookes, H. Fukazawa, S. Nakatsuji, and Y. Maeno, Phys. Rev. Lett. **87**, 077202 (2001).
[5] Y. Maeno, H. Hashimoto, K. Yoshida, S. Nishizaki, T. Fujita, J. G. Bednorz, and F. Lichtenberg, Nature (London) **372**, 532 (1994); A. P. Mackenzie and, Y. Maeno, Rev. Mod. Phys. **75**, 657 (2003).
[6] S. Nakatsuji, S. Ikeda, and Y. Maeno, J. Phys. Soc. Jpn. **66**, 1868 (1997).
[7] S. Nakatsuji and Y. Maeno, Phys. Rev. Lett. **84**, 2666 (2000); Phys. Rev. B **62**, 6458 (2000); S. Nakatsuji, D. Hall, L. Balicas, Z. Fisk, K. Sugahara, M. Yoshioka, and Y. Maeno, Phys. Rev. Lett. **90**, 137202 (2003); S. Nakatsuji, V. Dobrosavljevic, D. Tanaskovic, M. Minakata, H. Fukazawa, and Y. Maeno, *ibid.* **93**, 146401 (2004).
[8] M. Braden, G. Andre, S. Nakatsuji, and Y. Maeno, Phys. Rev. B **58**, 847 (1998).
[9] F. Nakamura, T. Goko, M. Ito, T. Fujita, S. Nakatsuji, H. Fukazawa, Y. Maeno, P. Alireza, D. Forsythe, and S. R. Julian, Phys. Rev. B **65**, 220402(R) (2002).
[10] F. Nakamura, J. Phys. Soc. Jpn. **76** Suppl. A, 96 (2007).
[11] Y. Takahashi, J. Phys. Soc. Jpn. **55**, 3553 (1986).
[12] P. Steffens, O. Friedt, P. Alireza, W. G. Marshall, W. Schmidt, F. Nakamura, S. Nakatsuji, Y. Maeno, R. Lengsdorf, M. M. Abd-Elmeguid, and M. Braden, Phys. Rev. B **72**, 094104 (2005).
[13] K. Murata, H. Yoshino, H. Yadav, Y. Honda, and N. Shirakawa, Rev. Sci. Instrum. **68**, 2490 (1997).
[14] H. H. Potter, Proc. R. Soc. London **A132**, 560 (1931).
[15] N. F. Mott and H. Jones, *The Theory of the Properties of Metals and Alloys* (Cambridge University Press, Cambridge, 1936), pp. 270–271.
[16] F. Nakamura (unpublished).
[17] T. Miyazaki and T. Ajima, J. Magn. Magn. Mater. **81**, 91 (1989).
[18] T. Goko *et al.* (unpublished).
[19] A. Koga, N. Kawakami, T. M. Rice, and M. Sigrist, Phys. Rev. Lett. **92**, 216402 (2004).

Physica C 470 (2010) S740–S741

Contents lists available at ScienceDirect

Physica C

journal homepage: www.elsevier.com/locate/physc

# Pressure induced novel-phenomena in Mott insulator $Ca_2RuO_4$

Yohei Yamauchi [a], Fumihiko Nakamura [a,*], Mariko Sakaki [a], Tetsuo Takemoto [a], Takashi Suzuki [a], Patricia L. Alireza [b], Yoshiteru Maeno [c]

[a] ADSM, Hiroshima University, Higashi-Hiroshima 739-8530, Japan
[b] Department of Physics, Cavendish Laboratory, University of Cambridge, Cambridge CB3 0HE, UK
[c] Department of Physics, Kyoto University, Kyoto 606-8052, Japan

ARTICLE INFO

*Article history:*
Accepted 21 December 2009
Available online 29 December 2009

*Keywords:*
$Ca_2RuO_4$
Mott transition
Pressure
Itinerant ferromagnetism
Quantum phase transition

ABSTRACT

In order to explore unconventional superconductivity, we have studied pressure effect on a 4*d*-electron Mott insulator $Ca_2RuO_4$. Pressurisation to $Ca_2RuO_4$ above 0.5 GPa transforms it from a Mott insulator to a metal with a ferromagnetic ground state. The itinerancy of the ferromagnetic state at 2 GPa is quantitatively evidenced by the magnetisation process at 2 K. Moreover, the pressure phase diagram of this system suggests the existence of a ferromagnetic quantum phase transition at ~10 GPa.



Recently, there has been growing interest in pressure effect on quantum phenomena such as unconventional superconductivity (SC) in strongly correlated electron systems. This is because pressurisation is generally known as a powerful tool to tune the properties of materials without introducing randomness, which can be extremely hostile to unconventional SC states.

It is known that a 4*d*-electron single-layered ruthenates $Sr_2RuO_4$ shows spin-triplet SC below 1.5 K [1]. Moreover, an isovalent replacement of Sr with Ca changes quasi-2D metal ($Sr_2RuO_4$) into Mott insulator ($Ca_2RuO_4$). To bridge this gap without introducing disorder, we have pressurised the Mott insulator $Ca_2RuO_4$.

So far, we have reported that pressurisation to $Ca_2RuO_4$ above 0.5 GPa transforms it from Mott insulator with Antiferromagnetism ground state to a metal with a ferromagnetic ground state [2,3]. We thus have strong interest in measurements at higher pressure as a crucial test of the connection between the unconventional SC and the pressure-induced ferromagnetism. However, many of the ferromagnetic properties remain to be veiled because of a luck of a nonmagnetic pressure cell allowing us to achieve pressure over 2 GPa at low temperatures. We have recently developed a piston-cylinder pressure cell for a commercial SQUID magnetometer (Quantum Design, model MPMS) allowing us to achieve pressure of 2.1 GPa at low temperature [4].

In the beginning of this paper, we show the magnetisation process of the pressure-induced ferromagnetic state in $Ca_2RuO_4$ at 2 GPa and discuss the itinerancy. The itinerancy of the ferromagnetism in the pressurised $Ca_2RuO_4$ is evidenced by following reasons: Firstly, the ferromagnetism was observed in the metallic phase. Secondly, the susceptibility obeys the Curie–Weiss law above $T_C \sim 10$ K, however, the effective paramagnetic moment of $p_{eff}$ 1.9 $\mu_B$/Ru-ion is too small to interpret a localised case (2.73 $\mu_B$/for $S = 1$). Thirdly, the magnetisation $M$ is not easily saturated with $\mu_0 H$. Moreover, the remnant $M$ along the $a$ axis of $M_{rem} \sim 0.4\ \mu_B$ is quite smaller than the saturated moment of 2 $\mu_B$ of localised system. A ratio of $p_{eff}/M_{rem} \sim 4.2$ is much larger than 1 of localised spins systems. Thus, it can be seen that the pressure-induced ferromagnetic nature is well interpreted as itinerant ferromagnetism.

Next we quantitatively evaluate the itinerant parameters according to the SCR spin fluctuation theory [5]. As shown in Fig. 1, the magnetisation process at the lowest $T$ of 2 K exhibits a good linearity in an Arrott plot ($M^2_{rem}$ vs. $H/M$ plot).

The characteristic temperature due to spin fluctuation is estimated to be $T_0 \sim 80$ K, namely $T_C/T_0 \sim 0.13$. Fig. 2 is based on the generalized Rhodes–Wohlfarth plot for itinerant ferromagnetism by Takahashi [6] where $p_{eff}/M_{rem}$ is plotted as a function of $T_C/T_0$. The itinerant parameters of $Ca_2RuO_4$ at 2 GPa are well located on the theoretical curve. Thus, it can be seen that the pressurised $Ca_2RuO_4$ is an itinerant ferromagnetism in a Q2D metal, which is theoretically predicted [7].

Let us next mention the pressure phase diagram of $Ca_2RuO_4$, especially in the vicinity of 10 GPa. In our previous report, the pressure variation of ferromagnetic transition was obtained from a peak in the $T$ dependence of out-of-plane resistivity at $T^*$ [2]. We show here the pressure variation of $T_C$ obtained by the $T$

* Corresponding author. Tel./fax: +81 824 7042.
*E-mail address:* fumihiko@hiroshima-u.ac.jp (F. Nakamura).

0921-4534/$ - see front matter © 2009 Elsevier B.V. All rights reserved.
doi:10.1016/j.physc.2009.12.049

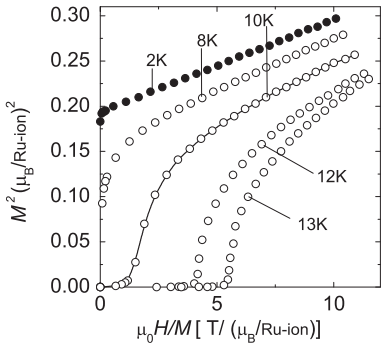


**Fig. 1.** $M^2_{rem}$ is plotted against as a function of $H/M$ plot.

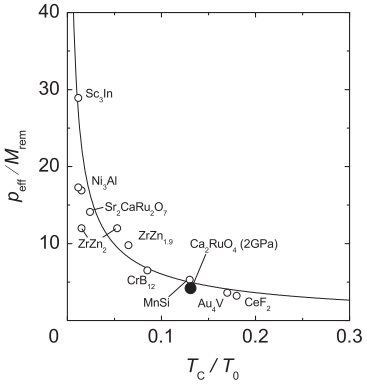


**Fig. 2.** The generalized Rhodes–Wohlfarth plot for itinerant ferromagnetism [6]. The parameter of the pressure-induced ferromagnetism in $Ca_2RuO_4$ is indicated by a closed circle.

dependence of magnetic measurements. The dc magnetisation was measured under pressure generated by two types of clump-type cells (piston-cylinder and diamond anvil). Furthermore, ac susceptibility was measured in a constant-pressure condition achieved by a cubic-anvil apparatus.

Fig. 3 summarises the $T_C$ obtained by the clump-type cells (open square) and the constant-pressure type apparatus (closed circle) as a function of pressure up to ~10 GPa. With pressurising, $T_C$ increases from ~10 K at 0.5 GPa reaching maximum of ~25 K at ~6 GPa, and then it starts to decrease. The $T_C$ obtained by the constant-pressure type cubic-anvil apparatus decreases gradually with pressurising up to ~10 GPa. This variation agrees well with the pressure dependence of $T^*$ [2].

In contrast, the pressure variation of $T_C$ obtained by the clump-type diamond-anvil cell shows an evident difference above 7 GPa. That is, any evidence of ferromagnetic ordering could not identified in our measurement with further pressurisation above $P \sim 6.5$ GPa. Indeed, a drastic reduction of the ferromagnetic moment at ~9 GPa has also been reported in the measurement using the clump-type

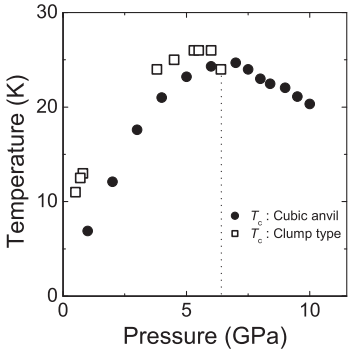


**Fig. 3.** Pressure phase diagram of $Ca_2RuO_4$. The data obtained by using clump-type cells and cubic anvil type is shown by an open square and a closed circle, respectively. The evidence of ferromagnetic ordering in the $T$ dependence of magnetisation is killed by pressurising above 6.5 GPa. The phase transition is marked by a dotted line.

Moissanite-anvil cell [8]. Moreover, absence of the FM-$T_C$ and evidence of pressure-induced superconductivity above ~8 GPa has also been reported recently [9]. Thus, it can be seen that the $T_C$ abruptly vanishes in the case of the pressurisation using a clump-type cell.

We deduce that this difference is due to the deviation from hydrostaticity. It is known that a significant difference in pressure effect on a quasi-2D system is often caused by the deviation from hydrostaticity [10]. Indeed, the pressurised $Ca_2RuO_4$ is strongly anisotropic in not only metallic nature but also magnetism [2,3].

In summary, pressurisation to a 4*d*-electron Mott insulator $Ca_2RuO_4$ transforms to a quasi-2D metal with a ferromagnetic ground state. We have evaluated that the magnetic properties is quantitatively interpreted as an itinerant ferromagnetism, which is predicted based on the SCR theory. Moreover, pressure variation of $T_C$ at ~10 GPa indicates the existence of quantum phase transition, which is most likely sensitive to hydrostaticity. We thus have strong interest in measurements at higher pressure as a crucial test of the bridge between the *p*-wave SC and the itinerant ferromagnetism.

## References

[1] Y. Maeno, H. Hashimoto, K. Yoshida, S. Nakanishi, T. Fujita, J.G. Bendnorz, F. Lichtenberg, Nature 372 (1994) 532.
[2] F. Nakamura, T. Goko, M. Ito, T. Fujita, Phys. Rev. B 65 (2002) 220402(R).
[3] F. Nakamura, J. Phys. Soc. Jpn. 76 (Suppl. A) (2007) 96.
[4] R. Nakai, F. Nakamura, T. Suzuki, J. Phys. Soc. Jpn. 76 (Suppl. A) (2007) 219.
[5] Y. Takahashi, J. Phys: Condens. Matter 11 (1999) 6439.
[6] S. Ikeda, Y. Maeno, T. Fujita, Phys. Rev. B 57 (1998) 978.
[7] M. Hatatani, T. Moriya, J. Phys. Soc. Jpn. 64 (1995) 3434.
[8] P.L. Alireza, S. Barakat, A.M. Cumberlidge, G. Lonzarich, F. Nakamura, Y. Maeno, J. Phys. Soc. Jpn. 76 (Suppl. A) (2007) 216.
[9] Patricia L. Alireza, Fumihiko Nakamura, Swee K. Goh, Yoshiteru Maeno, Satoru Nakatsuji, Y.T. Chris Ko, Michael Sutherland, Stephen Julian, Gilbert G. Lonzarich, J. Phys.: Condens. Matter (in press). (see also arXiv:0912.1513 [cond-mat.supr-con] ).
[10] F. Nakamura, T. Goko, J. Hori, Y. Uno, N. Kikugawa, T. Fujita, Phys. Rev. B 61 (2000) 107.

(19)日本国特許庁(JP)　(12)公開特許公報(A)　(11)特許出願公開番号
特開2010-166039
(P2010-166039A)
(43)公開日　平成22年7月29日(2010.7.29)

| (51)Int.Cl. | | F I | | | テーマコード（参考） |
|---|---|---|---|---|---|
| H01L 27/10 | (2006.01) | H01L | 27/10 | 451 | 4G048 |
| H01L 21/8246 | (2006.01) | H01L | 27/10 | 447 | 4M112 |
| H01L 27/105 | (2006.01) | H01L | 27/10 | 448 | 4M119 |
| H01L 43/08 | (2006.01) | H01L | 43/08 | M | 5F083 |
| H01L 45/00 | (2006.01) | H01L | 45/00 | Z | 5F092 |

審査請求 未請求　請求項の数 14　ＯＬ　（全 25 頁）　最終頁に続く

(21)出願番号　特願2009-283474 (P2009-283474)
(22)出願日　平成21年12月14日 (2009.12.14)
(31)優先権主張番号　特願2008-322131 (P2008-322131)
(32)優先日　平成20年12月18日 (2008.12.18)
(33)優先権主張国　日本国 (JP)

(71)出願人　504136568
国立大学法人広島大学
広島県東広島市鏡山１丁目３番２号
(74)代理人　100095407
弁理士　木村　満
(74)代理人　100138955
弁理士　末次　渉
(74)代理人　100151873
弁理士　鶴　寛
(74)代理人　100109449
弁理士　毛受　隆典
(72)発明者　中村　文彦
広島県東広島市鏡山一丁目３番１号　国立大学法人広島大学大学院先端物質科学研究科内

最終頁に続く

(54)【発明の名称】ペロブスカイト型酸化物の相転移誘起方法、電子機能素子材料として用いられるペロブスカイト型酸化物、ペロブスカイト型酸化物を用いた電子機能素子及び電子装置

(57)【要約】
【課題】モット絶縁体であるペロブスカイト型酸化物の絶縁体相－金属相間の相転移を容易に誘起することができるペロブスカイト型酸化物の相転移誘起方法を提供する。
【解決手段】本発明のペロブスカイト型酸化物の相転移を誘起するための相転移誘起方法は、絶縁体相にあるペロブスカイト型酸化物に、これまでの数ｋＶ／ｃｍよりも２桁低い４０Ｖ／ｃｍ～８０Ｖ／ｃｍ程度の電場を印加することで、絶縁体相にあるペロブスカイト型酸化物を金属相に相転移させると共に、電場の印加により金属相に相転移したペロブスカイト型酸化物を冷却させることで、常磁性金属相にあるペロブスカイト型酸化物を強磁性金属相に相転移させる。
【選択図】図１

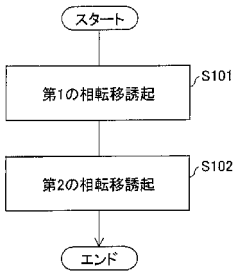

【特許請求の範囲】
【請求項１】
ペロブスカイト型酸化物の相転移を誘起するための相転移誘起方法であって、
前記ペロブスカイト型酸化物は、組成式$A_xB_yO_z$で表されるペロブスカイト型結晶構造を有し、前記組成式$A_xB_yO_z$において、前記元素Ａは、アルカリ土類金属から選ばれる少なくとも１種の元素であり、前記元素Ｂは、遷移元素から選ばれる少なくとも１種の元素のうち、４ｄ軌道または５ｄ軌道に存在する電子が１０個未満である元素である場合において、
絶縁体相にあるペロブスカイト型酸化物に所定の電圧を与えることにより、前記ペロブスカイト型酸化物に所定の電場を印加する電場印加ステップと、
前記電場印加ステップにおいて前記ペロブスカイト型酸化物に印加される前記電場を用いて、前記絶縁体相にある前記ペロブスカイト型酸化物を金属相に相転移させる第１の相転移誘起ステップと
を含むことを特徴とするペロブスカイト型酸化物の相転移誘起方法。
【請求項２】
前記第１の相転移誘起ステップにおいて前記金属相に相転移した前記ペロブスカイト型酸化物の雰囲気中の温度を降温する降温ステップと、
前記降温ステップにおいて前記ペロブスカイト型酸化物を冷却させて、前記金属相にある前記ペロブスカイト型酸化物を強磁性金属相に相転移させる第２の相転移誘起ステップとをさらに含むことを特徴とする請求項１に記載のペロブスカイト型酸化物の相転移誘起方法。
【請求項３】
前記ペロブスカイト型酸化物を前記金属相に相転移させるときの雰囲気中の温度は、３５６Ｋ以下であることを特徴とする請求項１または２に記載のペロブスカイト型酸化物の相転移誘起方法。
【請求項４】
前記ペロブスカイト型酸化物を前記金属相に相転移させるために印加すべき前記電場のしきい値の設定範囲は、雰囲気中が常温であるときに４０Ｖ／ｃｍ以上８０Ｖ／ｃｍ以下であることを特徴とする請求項１乃至３のいずれか１項に記載のペロブスカイト型酸化物の相転移誘起方法。
【請求項５】
前記ペロブスカイト型酸化物が前記金属相に相転移した後においては、前記ペロブスカイト型酸化物に印加される前記電場が２５Ｖ／ｃｍ以下になるまでは前記金属相が維持されることを特徴とする請求項１乃至４のいずれか１項に記載のペロブスカイト型酸化物の相転移誘起方法。
【請求項６】
前記ペロブスカイト型酸化物を前記強磁性金属相に相転移させるときの雰囲気中の温度は、２５Ｋ以下であることを特徴とする請求項２に記載のペロブスカイト型酸化物の相転移誘起方法。
【請求項７】
前記ペロブスカイト型酸化物の組成式は、$A_3Ru_2O_7$、$A_2RuO_4$、$ARuO_3$、$A_4Ru_3O_{10}$、$A_2IrO_4$、$A_3Ir_2O_7$及び$A_2RhO_4$のうちのいずれかであって、且つ、前記元素Ａは、Ｃａ、Ｓｒ、Ｂａ、Ｌａのうちのいずれかであることを特徴とする請求項１乃至６のいずれか１項に記載のペロブスカイト型酸化物の相転移誘起方法。
【請求項８】
電子機能素子の材料として用いられるペロブスカイト型酸化物であって、
前記ペロブスカイト型酸化物は、組成式$A_xB_yO_z$で表されるペロブスカイト型結晶構造を有し、前記組成式$A_xB_yO_z$において、前記元素Ａは、アルカリ土類金属から選ばれる少なくとも１種の元素であり、前記元素Ｂは、遷移元素から選ばれる少なくとも１種の元素のうち、４ｄ軌道または５ｄ軌道に存在する電子が１０個未満である元素である場合

において、
前記ペロブスカイト型酸化物は、自身に印加される電場を用いて、絶縁体相と金属相との間を相転移することにより、前記電子機能素子の機能を実現することを特徴とするペロブスカイト型酸化物。
【請求項９】
前記ペロブスカイト型酸化物は、前記絶縁体相から前記金属相に相転移した後において、自身の温度の昇降を用いて、常磁性金属相と強磁性金属相との間を相転移することにより、前記電子機能素子の機能を実現することを特徴とする請求項８に記載のペロブスカイト型酸化物。
【請求項１０】
請求項８または９に記載のペロブスカイト型酸化物を用いて所定の機能を実現することを特徴とする電子機能素子。
【請求項１１】
請求項８に記載のペロブスカイト型酸化物より成る可変抵抗部を有する電子機能素子と、
前記可変抵抗部に印加する電圧を調整する電圧調整手段と、
前記電子機能素子周辺の雰囲気温度を調整する温度調整手段と、
を備える電子装置。
【請求項１２】
前記温度調整手段は、
前記雰囲気温度を、前記ペロブスカイト型酸化物が金属体から絶縁体に相転移する温度より低い温度に維持し、
前記電圧調整手段は、前記ペロブスカイト型酸化物が前記絶縁体から前記金属体に相転移する第１の電圧より高い電圧を、前記可変抵抗部に印加するか、前記ペロブスカイト型酸化物が前記絶縁体から前記金属体に相転移する第２の電圧より低い電圧を、前記可変抵抗部に印加することにより、前記可変抵抗部の抵抗値を変更する、
ことを特徴とする請求項１１に記載の電子装置。
【請求項１３】
前記温度調整手段は、
前記雰囲気温度を、前記ペロブスカイト型酸化物が絶縁体から金属体に相転移する第１の温度より低く、前記ペロブスカイト型酸化物が前記金属体から前記絶縁体に相転移する第２の温度より高い温度に維持し、
前記電圧調整手段は、前記ペロブスカイト型酸化物が前記絶縁体から前記金属体に相転移する第１の電圧より高い電圧を、前記可変抵抗部に印加することにより、前記可変抵抗部の抵抗値を変更する、
ことを特徴とする請求項１１に記載の電子装置。
【請求項１４】
前記可変抵抗部に加える圧力を調整する圧力調整手段をさらに備える、
ことを特徴とする請求項１１乃至１３のいずれか１項に記載の電子装置。
【発明の詳細な説明】
【技術分野】
【０００１】
本発明は、$Ca_2RuO_4$等のモット絶縁体であるペロブスカイト型酸化物の相転移を誘起するための相転移誘起方法、電子機能素子材料として用いられるペロブスカイト型酸化物、ペロブスカイト型酸化物を用いた電子機能素子及び電子装置に関する。
【背景技術】
【０００２】
新奇の量子相転移現象の探索は、現在の物理学の重要なテーマの１つである。また、量子相転移現象には、磁気記録媒体等の電子デバイスへの応用が期待されている。
【０００３】

ところで、超伝導、強磁性、モット転移等の量子相転移現象を実現するためには、高圧力や高磁気等といった特殊な設備環境を作り出さなければならない。このため、このような量子相転移現象の実現には大型の圧力装置や磁気装置、高度に熟練した圧力技術や磁気技術が必要とされている。

【０００４】

また、そのように作り出される極限環境の下で量子相転移現象を測定可能な実験手段は、現在、非常に限られている。

【０００５】

このため、高圧力、高磁気等の極限環境の下で現れる量子相転移現象を実用化することは、現実には、非常に困難な状況になってしまっている。

【０００６】

このような状況を考慮して、近年、光や電場を物質に印加することにより、物質のキャリア数や電子相関を制御しようという試みが盛んに研究されている（例えば、非特許文献１を参照）。

【０００７】

光や電場を物質に印加することで量子相転移現象を誘起することができれば、上述したような、高度な圧力技術や特別な実験環境を必要としなくても、その量子相転移現象を測定するための実験が可能となる。さらに、光や電場の制御は圧力や磁気の制御と比較して容易であり、このため、電子デバイス応用の可能性が飛躍的に増加する。

【０００８】

ところが、現実には、電場で電荷注入し、超伝導、強磁性、モット転移等の量子相転移を誘起することは容易なことではない。もちろん、電場で量子相転移現象を誘起することに成功できれば、電場が圧力に変わる外部パラメータとして有力な実験手法になることは間違いない。

【０００９】

一方、電場で物質の磁性（強磁性）を制御すること、すなわち、Ｅｌｅｃｔｒｏｍａｇｎｅｔｓが様々な物質で報告されている。そして、近年、強誘電体に電場を印加することで強磁性が発生する、いわゆるマルチフェロイクスが熱く研究されている。しかし、これまで発見されてきた物質は絶縁体であり、しかも強磁性の誘起には強電場を必要とするものであった。

【００１０】

例えば、特許文献１には、金属元素Ｍと６つの酸素Ｏからなる$MO_6$八面体から構成されるペロブスカイト型酸化物またはその類縁の酸化物における$MO_6$八面体同士の相対的な配置を、圧力印加により調節することによって、電気伝導性や磁性等の電子状態を制御することができる、結晶構造歪による固体電子物性の制御方法が記載されている。

【００１１】

この結晶構造歪による固体電子物性の制御方法では、ペロブスカイト型酸化物の結晶構造の構成要素である$MO_6$八面体が相対的にどのようにネットワークを作っているかに着目し、その相対位置によって、電気伝導性や磁性を制御している。

【００１２】

そして、この制御方法では、その$MO_6$八面体同士の相対的な配置を調節するための具体的手法として、圧力を印加する手法が具体的に記載されている。

【先行技術文献】

【特許文献】

【００１３】

【特許文献１】特開２００４－７５４１５号公報（平成１６年３月１１日公開）

【非特許文献】

【００１４】

【非特許文献１】井上公、「遷移金属酸化物単結晶への電界効果ドーピング」、応用物理、社団法人応用物理学会、2005年7月、74巻、7号、p. 944-949

【発明の概要】
【発明が解決しようとする課題】
【００１５】
ところで、電場誘起のモット転移も、それだけでも興味あるテーマである。それは、モット転移近傍では様々な量子臨界現象が起こるからである。また、何桁もの急激な抵抗変化はスイッチング素子として最適である。
【００１６】
上述したように、モット転移等の量子相転移現象は、元素置換による電荷注入、あるいは、圧力印加による電子相関の制御によって行なわれてきた。
【００１７】
しかし、圧力印加は、技術的困難さと共に、圧力下で測定できる手段が限られてしまうといった課題があった。
【００１８】
また、元素置換は、同時に電子の乱れも物質に導入してしまうので、低温での本質的量子現象が隠されてしまうといった課題もあった。
【００１９】
これに対し、電場によるキャリアの制御ができれば、量子臨界現象を容易に探索できるだけでなく、電子デバイス等への応用の面でも波及効果が大きい。
【００２０】
これまで、電場誘起のモット転移は、Ｎｉ酸化物や有機物では報告されている。しかし、しきい電場は酸化物で数ｋＶ／ｃｍ、有機物で４ｋＶ／ｃｍと、金属化するにはかなりの高電圧が必要である。さらに、電場誘起した金属相で超伝導や強磁性等の量子化相転移現象（基底状態）を観測した例は未だにない。
【００２１】
上記課題に鑑み、本発明の目的は、モット絶縁体であるペロブスカイト型酸化物の絶縁体相－金属相間の相転移を容易に誘起することができるペロブスカイト型酸化物の相転移誘起方法、電子機能素子材料として用いられるペロブスカイト型酸化物、ペロブスカイト型酸化物を用いた電子機能素子及び電子装置を提供することである。
【課題を解決するための手段】
【００２２】
上記目的を達成するために、本発明者等は、圧力下でモット転移した後に低温で遍歴強磁性を示すモット絶縁体$Ca_2RuO_4$を用いて鋭意検討した結果、モット絶縁体$Ca_2RuO_4$に対し、乾電池１個に満たないわずかな電場を加えることで、絶縁破壊、すなわち、絶縁体－金属転移を引き起こし、さらに、その後、印加電圧を電池２～３個程度の電圧値まで上昇させ、冷却することにより金属強磁性が出現することを明らかにした。
【００２３】
すなわち、本発明におけるペロブスカイト型酸化物の相転移誘起方法は、ペロブスカイト型酸化物の相転移を誘起するための相転移誘起方法であって、前記ペロブスカイト型酸化物は、組成式$A_xB_yO_z$で表されるペロブスカイト型結晶構造を有し、前記組成式$A_xB_yO_z$において、前記元素Ａは、アルカリ土類金属から選ばれる少なくとも１種の元素であり、前記元素Ｂは、遷移元素から選ばれる少なくとも１種の元素のうち、４ｄ軌道または５ｄ軌道に存在する電子が１０個未満である元素である場合において、絶縁体相にあるペロブスカイト型酸化物に所定の電圧を与えることにより、前記ペロブスカイト型酸化物に所定の電場を印加する電場印加ステップと、前記電場印加ステップにおいて前記ペロブスカイト型酸化物に印加される前記電場を用いて、前記絶縁体相にある前記ペロブスカイト型酸化物を金属相に相転移させる第１の相転移誘起ステップとを含む。
【００２４】
上記のペロブスカイト型酸化物の相転移誘起方法では、絶縁体相にあるペロブスカイト型酸化物に所定の電圧を与えてペロブスカイト型酸化物に所定の電場を印加し、その印加電場を用いて、ペロブスカイト型酸化物を絶縁体相から金属相に相転移させている。

【００２５】
このため、従来では圧力印加や元素置換によって行なわれていたペロブスカイト型酸化物における絶縁体相－金属相間の相転移、つまり、モット転移を、電場を印加することにより誘起することができる。
【００２６】
すなわち、ペロブスカイト型酸化物への電場印加は、圧力印加や元素置換と比較して、より簡単な装置構成により実現することができるので、ペロブスカイト型酸化物のモット転移を従来と比べて容易に行なうことが可能となる。
【００２７】
前記第１の相転移誘起ステップにおいて前記金属相に相転移した前記ペロブスカイト型酸化物の雰囲気中の温度を降温する降温ステップと、前記降温ステップにおいて前記ペロブスカイト型酸化物を冷却させて、前記金属相にある前記ペロブスカイト型酸化物を強磁性金属相に相転移させる第２の相転移誘起ステップとをさらに含むことが好ましい。
【００２８】
この場合、金属相に相転移したペロブスカイト型酸化物の雰囲気中の温度を降温し、ペロブスカイト型酸化物を冷却させて、金属相にあるペロブスカイト型酸化物を強磁性金属相に相転移させることができる。
【００２９】
前記ペロブスカイト型酸化物を前記金属相に相転移させるときの雰囲気中の温度は、３５６Ｋ以下であることが好ましい。
【００３０】
前記ペロブスカイト型酸化物を前記金属相に相転移させるために印加すべき前記電場のしきい値の設定範囲は、雰囲気中が常温であるときに４０Ｖ／ｃｍ以上８０Ｖ／ｃｍ以下であることが好ましい。
【００３１】
前記ペロブスカイト型酸化物が前記金属相に相転移した後においては、前記ペロブスカイト型酸化物に印加される前記電場が２５Ｖ／ｃｍ以下になるまでは前記金属相が維持されることが好ましい。
【００３２】
前記ペロブスカイト型酸化物を前記強磁性金属相に相転移させるときの雰囲気中の温度は、２５Ｋ以下であることが好ましい。
【００３３】
前記ペロブスカイト型酸化物の組成式は、$A_3Ru_2O_7$、$A_2RuO_4$、$ARuO_3$、$A_4Ru_3O_{10}$、$A_2IrO_4$、$A_3Ir_2O_7$及び$A_2RhO_4$のうちのいずれかであって、且つ、前記元素Ａは、Ｃａ、Ｓｒ、Ｂａ、Ｌａのうちのいずれかであることが好ましい。
【００３４】
本発明におけるペロブスカイト型酸化物は、電子機能素子の材料として用いられるペロブスカイト型酸化物であって、前記ペロブスカイト型酸化物は、組成式$A_xB_yO_z$で表されるペロブスカイト型結晶構造を有し、前記組成式$A_xB_yO_z$において、前記元素Ａは、アルカリ土類金属から選ばれる少なくとも１種の元素であり、前記元素Ｂは、遷移元素から選ばれる少なくとも１種の元素のうち、４ｄ軌道または５ｄ軌道に存在する電子が１０個未満である元素である場合において、前記ペロブスカイト型酸化物は、自身に印加される電場を用いて、絶縁体相と金属相との間を相転移することにより、前記電子機能素子の機能を実現する。
【００３５】
上記のペロブスカイト型酸化物では、電場印加により絶縁体相と金属相との間を相転移することができるので、この電場印加による相転移を用いた新たな電子機能素子を実現することができる。
【００３６】
前記ペロブスカイト型酸化物は、前記絶縁体相から前記金属相に相転移した後において

、自身の温度の昇降を用いて、常磁性金属相と強磁性金属相との間を相転移することにより、前記電子機能素子の機能を実現することが好ましい。

【００３７】

この場合、温度の昇降により常磁性金属相と強磁性金属相との間を相転移することができるので、この温度の昇降による相転移を用いた新たな電子機能素子を実現することができる。

【００３８】

本発明における電子機能素子は、上記のペロブスカイト型酸化物を用いて所定の機能を実現する。

【００３９】

上記の電子機能素子では、ペロブスカイト型酸化物の相転移を用いた新たな電子機能素子を実現することができる。

【００４０】

本発明における電子装置は、上記のペロブスカイト型酸化物より成る可変抵抗部を有する電子機能素子と、前記可変抵抗部に印加する電圧を調整する電圧調整手段と、前記電子機能素子周辺の雰囲気温度を調整する温度調整手段と、を備える。

【００４１】

上記の電子装置では、電圧調整手段の電圧調整及び温度調整手段の温度調整により、ペロブスカイト型酸化物の相転移条件をフレキシブルに変更することができる。

【００４２】

この場合、前記温度調整手段は、前記雰囲気温度を、前記ペロブスカイト型酸化物が金属体から絶縁体に相転移する温度より低い温度に維持し、前記電圧調整手段は、前記ペロブスカイト型酸化物が前記絶縁体から前記金属体に相転移する第１の電圧より高い電圧を、前記可変抵抗部に印加するか、前記ペロブスカイト型酸化物が前記絶縁体から前記金属体に相転移する第２の電圧より低い電圧を、前記可変抵抗部に印加することにより、前記可変抵抗部の抵抗値を変更する、こととしてもよい。

【００４３】

このようにすれば、上記の電子装置を、揮発性のメモリとして動作させることができる。

【００４４】

また、前記温度調整手段は、前記雰囲気温度を、前記ペロブスカイト型酸化物が前記絶縁体から前記金属体に相転移する第１の温度より低く、前記ペロブスカイト型酸化物が前記金属体から前記絶縁体に相転移する第２の温度より高い温度に維持し、前記電圧調整手段は、前記ペロブスカイト型酸化物が絶縁体から金属体に相転移する第１の電圧より高い電圧を、前記可変抵抗部に印加することにより、前記可変抵抗部の抵抗値を変更する、こととしてもよい。

【００４５】

このようにすれば、上記の電子装置を、不揮発性のメモリとして動作させることができる。

【００４６】

また、前記可変抵抗部に加える圧力を調整する圧力調整手段をさらに備える、こととしてもよい。

【００４７】

圧力調整手段の圧力調整により、ペロブスカイト型酸化物の相転移条件をフレキシブルに変更することができる。

【発明の効果】

【００４８】

本発明のペロブスカイト型酸化物の相転移を誘起するための相転移誘起方法は、以上のように、絶縁体相にあるペロブスカイト型酸化物に所定の電圧を与えることにより、前記ペロブスカイト型酸化物に所定の電場を印加する電場印加ステップと、前記電場印加ステ

ップにおいて前記ペロブスカイト型酸化物に印加される電場を用いて、前記絶縁体相にある前記ペロブスカイト型酸化物を金属相に相転移させる第１の相転移誘起ステップとを含む方法である。

【００４９】

それゆえ、モット絶縁体であるペロブスカイト型酸化物の絶縁体相－金属相間の相転移を容易に誘起することができるという効果を奏する。

【図面の簡単な説明】

【００５０】

【図１】本発明の実施の形態１におけるペロブスカイト型酸化物の相転移を誘起するための相転移誘起方法の処理手順を示すフローチャートである。

【図２】本発明の実施の形態１におけるペロブスカイト型酸化物の相転移を評価するための測定回路の構成を示す概略図である。

【図３】本発明の実施の形態１におけるペロブスカイト型酸化物の電流－電圧特性を示すグラフ図である。

【図４】図４（Ａ）は、単結晶試料に歪みを加えたときの本発明の実施の形態１におけるペロブスカイト型酸化物のＸ線回折結果を示すグラフ図であり、図４（Ｂ）は、単結晶試料に歪みを加えていないときの本発明の実施の形態１におけるペロブスカイト型酸化物のＸ線回折結果を示すグラフ図である。

【図５】本発明の実施の形態１におけるペロブスカイト型酸化物の抵抗の温度依存性を示すグラフ図である。

【図６】図５のグラフ図における温度が０Ｋ～３０Ｋ付近を拡大したグラフ図である。

【図７】従来のペロブスカイト型酸化物の抵抗の温度依存性を示すグラフ図である。

【図８】本発明の実施の形態１におけるペロブスカイト型酸化物の磁化測定結果を示すグラフ図である。

【図９】本発明の実施の形態２における電界効果トランジスタの構成を示す断面図である。

【図１０】本発明の実施の形態３におけるＭＲＡＭの基本的な素子の構成を示す斜視図である。

【図１１】本発明の実施の形態３におけるＭＲＡＭの他の構成を示す斜視図である。

【図１２】本発明の実施の形態４における電子機能素子の構造を示す断面図である。

【図１３】本発明の実施の形態４におけるメモリ装置の構成を示すブロック図である。

【図１４】図１２の電子機能素子のペロブスカイト型酸化物層の抵抗の温度依存性の一例を示すグラフである。

【図１５】絶縁体相におけるペロブスカイト型酸化物層の電圧－電流特性の一例を示すグラフである。

【図１６】双安定相におけるペロブスカイト型酸化物層の電圧－電流特性の一例を示すグラフである。

【図１７】図１２の電子機能素子のペロブスカイト型酸化物層の抵抗の圧力依存性の一例を示すグラフである。

【発明を実施するための形態】

【００５１】

本発明の実施の形態について図１～図１７に基づいて説明すれば、以下の通りである。

【００５２】

〔実施の形態１〕

先ず、本発明の実施の形態１におけるペロブスカイト型酸化物について説明する。

【００５３】

本発明の実施の形態１におけるペロブスカイト型酸化物の単結晶は、公知の単結晶作製法、例えばＦＺ（フローティング・ゾーン）法等を用いて作製することができる。

【００５４】

また、本実施の形態におけるペロブスカイト型酸化物を層状で用いる場合、ＬＰＥ（リ

キッド・フェーズ・エピタキシー）法を用いる、あるいは、低ガス圧雰囲気で真空成膜法により形成することが好ましい。

【００５５】

真空成膜法の中では、ＭＢＥ（モレキュラー・ビーム・エピタキシー）法、レーザーアブレーション法や、高周波マグネトロンスパッタリング、直流スパッタリング、対向ターゲットスパッタリング、イオンビームスパッタリング等に代表されるスパッタリング法等が好ましい。

【００５６】

これら成膜法で作製する場合、エピタキシャル成長をさせるために、基板温度を少なくとも５５０℃以上７５０℃以下とすること、あるいは、成膜後にこれらの温度近傍で熱処理することが好ましい。

【００５７】

また、面内の一軸方向に異方性を形成するために、基板に対して一方向に磁界をかけながら成膜を行なうこと、一方向に磁界をかけながら３５０℃以下程度で熱処理すること、あるいは、単結晶基板の選択により特定方向に配向成長させること等が好ましい。

【００５８】

本実施の形態におけるペロブスカイト型酸化物は、組成式$A_xB_yO_z$で表されるペロブスカイト型結晶構造を有している。そして、この組成式$A_xB_yO_z$において、元素Ａは、アルカリ土類金属から選ばれる少なくとも１種の元素である。

【００５９】

また、元素Ｂは、遷移元素から選ばれる少なくとも１種の元素のうち、４ｄ軌道または５ｄ軌道に存在する電子が１０個未満である元素である。

【００６０】

具体的には、本実施の形態におけるペロブスカイト型酸化物は、その組成式が、$A_3Ru_2O_7$、$A_2RuO_4$、$ARuO_3$、$A_4Ru_3O_{10}$、$A_2IrO_4$、$A_3Ir_2O_7$及び$A_2RhO_4$のうちのいずれかであって、且つ、元素Ａが、Ｃａ、Ｓｒ、Ｂａ、Ｌａのうちのいずれかであるであることが好ましく、$Ca_2RuO_4$であることがより好ましい。

【００６１】

次に、本実施の形態におけるペロブスカイト型酸化物の相転移を誘起するための相転移誘起方法について説明する。図１は、本実施の形態におけるペロブスカイト型酸化物の相転移誘起方法の処理手順を示すフローチャートである。

【００６２】

図１に示すように、本実施の形態におけるペロブスカイト型酸化物の相転移誘起方法は、ペロブスカイト型酸化物に対する絶縁体相から金属相への第１の相転移を誘起する第１の相転移誘起ステップ（ステップＳ１０１）と、ステップＳ１０１において金属相に相転移したペロブスカイト型酸化物に対する常磁性金属相から強磁性金属相への第２の相転移を誘起する第２の相転移誘起ステップ（ステップＳ１０２）と、を含んでいる。

【００６３】

本実施の形態におけるペロブスカイト型酸化物の相転移誘起方法では、上記のステップＳ１０１において誘起される第１の相転移は、ペロブスカイト型酸化物に対して電場を印加することにより実現されている。背景技術の欄でも述べたように、従来では、ペロブスカイト型酸化物における絶縁体相から金属相への相転移、すなわち、公知のモット転移は、元素置換による電荷注入、あるいは、圧力印加による電子相関の制御によって行なわれてきた。元素置換による電荷注入による場合であれば、同時に電子の乱れも物質に導入してしまい、低温での本質的量子現象が隠されてしまうといった課題があった。また、圧力印加による場合であれば、圧力印加の技術的困難さと共に、圧力下で測定できる手段が限られてしまうといった課題があった。

【００６４】

一方、本実施の形態におけるペロブスカイト型酸化物の相転移誘起方法によれば、ペロブスカイト型酸化物の絶縁体相から金属相への第１の相転移を電場の印加により実現する

ことができる。この電場印加は、圧力印加や元素置換と比較して、より簡単な設備環境を用いて行なうことができる。

【００６５】

さらに、本実施の形態におけるペロブスカイト型酸化物の相転移誘起方法では、ペロブスカイト型酸化物の絶縁体相から金属相への第１の相転移を非常に弱い電場の印加により実現することができる。このため、この電場印加は、Ｎｉ酸化物や有機物のモット転移を電場印加により行なう場合と比較して、より簡単な設備環境を用いて行なうことができる。

【００６６】

したがって、このペロブスカイト型酸化物の絶縁体相から金属相への第１の相転移である新奇の量子相転移現象を用いることにより、従来にはなかった新規の電子機能素子を実現することができる。

【００６７】

次に、本実施の形態におけるペロブスカイト型酸化物の相転移誘起方法では、上記のステップＳ１０２において誘起される第２の相転移は、金属相に相転移したペロブスカイト型酸化物を徐々に温度を降下させると共に、そのペロブスカイト型酸化物に印加する電場を徐々に大きくすることにより実現されている。

【００６８】

したがって、このペロブスカイト型酸化物の絶縁体相から金属相への第１の相転移である新奇の量子相転移現象を用いることにより、又は第１の相転移である新奇の量子相転移現象と、金属相から強磁性金属相への第２の相転移である新奇の量子相転移現象とを組み合わせて用いることにより、従来にはなかった新規の電子機能素子を実現することができる。

【００６９】

（実施例１）

本実施例１では、本実施の形態におけるペロブスカイト型酸化物に含まれる$Ca_2RuO_4$を公知のＦＺ法を用いて作製し、単結晶試料を準備した。その試料の作製条件を下記に示す。

［作製条件］

試料：原料棒（酸化物混合原料２$CaCO_3$＋１．３３$RuO_2$）を１３５０℃で１２時間焼結し、赤外線集中加熱炉を用いたＦＺ法で約１０ｍｍ／ｈの成長速度で単結晶試料を成長させたもの

サイズ：（径；φ）５（ｍｍ）×（長さ；Ｌ）５０（ｍｍ）

また、本実施例１では、出来上がった試料を加工（適当なサイズにカット、劈開）した後、以下の測定に用いた。測定に用いた代表的な試料のサイズとしては、面積０．００２$cm^2$、厚さ０．００７５ｃｍであった。

【００７０】

次に、図２に示すように、上記の試料と負荷抵抗とを電気的に直列接続した測定回路１０を構成し、この測定回路１０を用いて、この試料に対する電流－電圧特性を測定した。

【００７１】

ここで、この測定回路１０においては、負荷抵抗１１は０Ω～８０Ω程度であり、試料に急激な電流が流れ込むことを防止するために接続されている。

【００７２】

なお、この負荷抵抗１１の値やその有無は、使用する電源によって異なるものであることは言うまでもない。したがって、試料の絶縁破壊によりリミッターを越える電流が流れる場合は必要となるが、高電圧・大電流に対応できる電源を使用したときには、必ずしも必要ではない。例えば、後述する図３、図５、図６の測定では、負荷抵抗１１は不要であり、図４（Ａ）の測定では、負荷抵抗１１の値は５０Ω～１００Ωとなる。

【００７３】

また、２端子測定のための２つの電極が、試料１２の長さ方向の両端部に接触されてお

り、このため、２つの電極間の距離はＬとなる。したがって、試料１２に印加される電場は、試料に印加される電圧をこの距離Ｌで割ったものとなる。

【００７４】

この測定回路１０には、電圧源１３と電流計１４とから構成された電場印加装置１５が直列接続されており、この電場印加装置１５の電圧源１３から供給される電圧が測定回路１０全体に印加される。また、電場印加装置１５の電流計１４は、電圧源１３から供給される電圧が測定回路１０に印加されると、測定回路１０に流れる電流を測定する。

【００７５】

負荷抵抗１１の両端部には、電圧計１６が接続されており、この電圧計１６を用いて負荷抵抗１１の両端部間の電圧を測定する。

【００７６】

この測定回路１０では、このようにして測定回路１０を流れる電流及び負荷抵抗１１の両端部の電圧を測定し、それらの測定結果に基づいて試料１２の電流－電圧特性を評価する。

【００７７】

次に、試料１２の電流－電圧特性の評価結果について説明する。

【００７８】

この評価においては、温度を３００Ｋ（常温）とし、電場印加装置１５の電圧源１３から供給される電圧を１ｍＶ／秒で上昇させながら、この測定回路１０に印加した。図３に、その電流－電圧特性を測定した結果を示す。

【００７９】

図３に示すように、印加電圧が０．６Ｖまでに達する以前では、電流はほとんど流れることがなく、試料１２の電流－電圧特性から算出される、試料１２の抵抗は約２００Ωであった。

【００８０】

ところが、印加電圧が０．６Ｖに達した時点で、すなわち、印加電場が８０Ｖ／ｃｍに達した時点で、この測定回路１０に急激に電流が流れ始め、その後、印加電圧の上昇に伴い、流れる電流も上昇した。試料１２の抵抗としては、印加電圧が０．６Ｖに達する以前と比較して、２桁も小さくなった。

【００８１】

このことから、この試料１２が乾電池１個に満たないわずかな電圧である０．６Ｖで金属化したことが分かる。

【００８２】

次に、印加電圧が０．６Ｖに達した時点で金属化し、その金属化の後、印加電圧を０．８Ｖまで上昇させた後、今度は、印加電圧を０．８Ｖから電圧を減少させた。このときの温度は、３００Ｋである。

【００８３】

図３に示すように、印加電圧が０．２Ｖに達するまでは、すなわち、印加電場が２５Ｖ／ｃｍに達するまでは、試料１２が金属状態を維持していることが分かる。

【００８４】

このようにして、本発明者等は、モット絶縁体$Ca_2RuO_4$に乾電池１個に満たないわずかな電圧を印加することにより、モット絶縁体$Ca_2RuO_4$に絶縁破壊、すなわち、絶縁体－金属転移を引き起こすことができることを明らかにした。

【００８５】

また、図３に示すように、試料１２の電流－電圧特性の曲線はヒステリシスを描いている。この大きなヒステリシスの存在は、モット絶縁体$Ca_2RuO_4$への電圧印加により誘起される絶縁体－金属転移が１次相転移であることを意味している。

【００８６】

さらに、図３に示した評価結果では、印加電圧を０．８Ｖから０．２Ｖまで減少させた時点で、試料１２の破壊が起こっている。この破壊の発生は、印加電圧が０．２Ｖに達し

たとき、試料１２の結晶系である斜方晶系が、ｃ軸が長く、体積の小さなＬ－Ｐｂｃａから、ｃ軸が短く、体積の大きなＳ－Ｐｂｃａに構造転移したことを示唆している。

【００８７】

すなわち、試料１２の破壊の発生時に、この試料１２は、Ｌ－Ｐｂｃａを持つ金属相からＳ－Ｐｂｃａを持つ絶縁体相へ相転移していると考えることができる。

【００８８】

このことは、次の事柄からも裏付けられる。すなわち、従来、モット絶縁体$Ca_2RuO_4$は加圧や冷却による相転移に伴ってモット転移（金属化）すると共に、金属相から絶縁体相に戻るときの体積膨張に伴って単結晶試料を構成するモット絶縁体$Ca_2RuO_4$が破壊されてしまうことが知られている。

【００８９】

したがって、電圧印加によりモット転移（金属化）した上記の試料に起こった破壊が、金属相から絶縁体相への構造転移に起因するものと考えられるからである。

【００９０】

ここで、図４（Ａ）に、上記の電流－電圧特性の評価に用いた試料と同一の試料についてのＸ線回折の評価結果を示す。

【００９１】

ここでは、試料に印加される電圧が０Ｖ、１．５Ｖ、２．５Ｖ、２．７Ｖ、２．８Ｖの各々のときにおける、Ｘ線回折結果が示されている。

【００９２】

図４（Ａ）に示すように、印加電圧が０Ｖであるときには、試料はｃ軸の短いＳ－Ｐｂｃａの斜方晶系を持つ絶縁体相にあることが分かる。また、印加電圧が２．８Ｖであるときには、試料はｃ軸の長いＬ－Ｐｂｃａの斜方晶系を持つ金属相にあることが分かる。

【００９３】

さらに、印加電圧が２．５Ｖ及び２．７Ｖであるときには、試料はＳ－Ｐｂｃａの斜方晶系を持つ絶縁体相とＬ－Ｐｂｃａの斜方晶系を持つ金属相の２つの相が共存する２相共存相にあることが分かる。

【００９４】

この２相共存相やヒステリシスの存在は、Ｓ－ＰｂｃａからＬ－Ｐｂｃａへの構造転移が、潜熱を伴う１次相転移であることを意味する。

【００９５】

すなわち、この試料は、電圧の印加、つまり、電場の印加により、絶縁体相から金属相への相転移が誘起されている。

【００９６】

なお、図４（Ａ）に示した評価では、このような絶縁体相－金属相間の相転移は、印加電圧が１．５Ｖを越えた付近で起こっている。印加電圧が０Ｖであるとき、試料の抵抗が約２００Ωであったが、１．６Ｖ以上の印加電圧により金属相が出現すると、試料の抵抗は約１０Ωまで小さくなった。

【００９７】

また、図４（Ａ）に示した評価では、試料をＸ線の照射位置に正確に固定させるため、ガラス基板に単結晶試料を、電極材（銀ペースト）を用いて完全に固定した。これに対して、試料の電極を薄い金の蒸着膜とし、その電極に０．００２５ｃｍの金線を取り付けただけの配置、すなわち、単結晶試料に歪みが生じていない状態でも測定を行なった。これにより、図４（Ｂ）に示すような測定結果が得られた。図４（Ａ）に示すように単結晶試料に歪みを加えた場合には、単結晶試料の結晶伸縮性が妨げられ、絶縁破壊電圧が、図４（Ｂ）の場合と比較して増大しているのがわかる。

【００９８】

このことから逆に、試料にひずみを加えることで、試料の絶縁破壊電圧を制御することができると言える。したがって、例えば、圧電素子などに試料を固定し、ab面（$RuO_2$面内）方向に試料を圧縮することで絶縁破壊電圧を減少させ、一方、ab面（$RuO_2$面内

）方向に試料が膨張または収縮することを妨げることで絶縁破壊電圧を増加させることができる。

【００９９】

（実施例２）

本実施例２では、絶縁体相から金属相へ転移した試料を用いて、その抵抗の温度依存性を測定した。その降温条件は、４（Ｋ／分）である。

【０１００】

ここでは、上記の実施例１において金属相に転移した試料を用い、その試料を徐々に降温させながら、試料の電流－電圧特性から抵抗を算出した。また、試料を降温させるときに印加電圧としては、４Ｖ、及び、５Ｖを用いて行なった。

【０１０１】

図５に、試料の抵抗の温度依存性を示し、図６に、図５の０Ｋ～３０Ｋ付近の拡大図を示す。

【０１０２】

図５及び図６に示すように、試料の印加電圧を４Ｖとしたときに、温度を５Ｋまで降温しても、試料の金属状態を維持することができた。また、印加電圧が４Ｖであったときには、温度が１０Ｋに達した時点で、試料の抵抗の急激な減少が観測された。さらに、試料の金属状態を低温まで維持するために最低限必要な電圧は４Ｖであった。

【０１０３】

また、印加電圧が５Ｖであったときには、温度が１２．５Ｋに達した時点で、試料の抵抗の急激な減少が観測された。

【０１０４】

ところで、このような試料の抵抗の減少は、公知の圧力印加によるモット転移（金属化）したモット絶縁体$Ca_2RuO_4$においても観測されている。図７は、その観測結果である。

【０１０５】

図７に示す観測結果は、モット絶縁体$Ca_2RuO_4$における強磁性秩序の発生による磁気散乱の減少による現象と理解されている。そして、図５及び図６に示した、試料の抵抗の急激な減少が開始する温度が、図７に示した強磁性転移温度と見事に一致している。

【０１０６】

この２つの温度の一致から、上記の実施例１で電圧の印加によりモット転移（金属化）したモット絶縁体$Ca_2RuO_4$において、強磁性が出現したことが分かる。

【０１０７】

なお、上記の観測においては、モット絶縁体$Ca_2RuO_4$における強磁性金属相への転移は１０Ｋ以下の温度で出現しているが、現在観測されている圧力印加に基づく相図からは、モット絶縁体$Ca_2RuO_4$における強磁性金属相への転移は、２５Ｋ以下の温度で出現することが既に実証されている。

【０１０８】

このことから、本実施の形態における電場印加に基づいて金属相に転移したモット絶縁体$Ca_2RuO_4$においても、同様に、１０Ｋ以下の温度で強磁性金属相への転移が出現することが予想される。

【０１０９】

次に、ＳＱＵＩＤ磁化測定装置を用いて試料に出現した強磁性を直接観測した結果を図８に示す。この観測においては、磁場を０．１テスラ、温度を６Ｋとし、電場なし（０Ｖ／ｃｍ）と電場を加えたとき（２２０Ｖ／ｃｍ）の２つの条件下における磁化測定を行なった。

【０１１０】

図８において、横軸をスキャン幅とし、試料の位置がそのスキャン幅の中心位置である。縦軸は磁化に比例したＳＱＵＩＤ信号（電圧）であり、凸型信号は磁場の方向に磁化が発生していることを意味する。

【０１１１】
図８に示すように、電場を加えることで試料に強磁性の出現を意味する大きな信号が出現した。この測定結果から求められるＲｕ１個当たりの磁化は０．０１５μＢ／Ｒｕ‐ｉｏｎであり、強磁性の出現を強く示唆するものであった。
【０１１２】
〔実施の形態２〕
次に、本発明の実施の形態２について説明する。本発明の実施の形態２は、上記の実施の形態１におけるペロブスカイト型酸化物を用いた電子機能素子を説明する形態である。
【０１１３】
本実施の形態における電子機能素子は、公知の電界効果トランジスタにおけるシリコン導電層を置換する、上記の実施の形態１におけるペロブスカイト型酸化物からなる層を有する電界効果トランジスタである。
【０１１４】
本実施の形態における電界効果トランジスタは、ペロブスカイト型酸化物層に形成されたソース領域及びドレイン領域と、そのソース領域とドレイン領域との間に配置されたゲート構造と、を備えている。図９は、本実施の形態における電界効果トランジスタの構成を示す断面図である。
【０１１５】
図９に示すように、本実施の形態における電界効果トランジスタ２０は、ゲート電極２１と、基板２６上に堆積されたペロブスカイト型酸化物層２５と、ペロブスカイト型酸化物層２５を挟むようにして基板２６上に堆積され、互いに反対の型の高濃度な不純物イオンを有するソース領域２３及びドレイン領域２４と、ゲート電極２１とペロブスカイト型酸化物層２５との間に配置されたゲート絶縁層２２と、を備えている。
【０１１６】
本実施の形態における電界型トランジスタの導電性チャネル層は、ペロブスカイト型酸化物層２５を用いて実現されている。以下、この電界効果トランジスタの動作について説明する。
【０１１７】
図９において、ゲート電極２１に正電圧が印加された場合には、ゲート電極２１に印加された正電圧がゲート絶縁層２２を介してペロブスカイト型酸化物層２５に印加される。
【０１１８】
そして、この正電圧がペロブスカイト型酸化物層２５の絶縁体相から金属相への相転移を誘起する電圧を越えると、ペロブスカイト型酸化物層２５が金属化する。
【０１１９】
このペロブスカイト型酸化物層２５の金属化により、ペロブスカイト型酸化物層２５内に高導電性チャネル（図示省略）が形成される。したがって、この電界効果トランジスタ２０は導通状態となる。
【０１２０】
すなわち、ソース領域２３とドレイン領域２４との間にバイアス電圧が印加される場合に、この電界効果トランジスタ２０を介して電流が流れることになる。
【０１２１】
次に、図９において、ゲート電極２１に負電圧が印加された場合には、ゲート電極２１に印加された負電圧がゲート絶縁層２２を介してペロブスカイト型酸化物層２５に印加される。
【０１２２】
そして、この負電圧がペロブスカイト型酸化物層２５の絶縁体相から金属相への相転移を誘起する電圧を下回ると、ペロブスカイト型酸化物層２５が再び絶縁体に戻ることになる。
【０１２３】
このペロブスカイト型酸化物層２５が絶縁体に戻ることにより、ペロブスカイト型酸化

物層２５内に形成されていた高導電性チャネル（図示省略）が消滅する。したがって、この電界効果トランジスタ２０は非導通状態となる。

【０１２４】

すなわち、ソース領域２３とドレイン領域２４との間にバイアス電圧が印加されても、この電界効果トランジスタ２０を介して電流が流れることはない。

【０１２５】

〔実施の形態３〕

次に、本発明の実施の形態３について説明する。本発明の実施の形態３は、上記の実施の形態１におけるペロブスカイト型酸化物を用いた他の電子機能素子を説明する形態である。

【０１２６】

本実施の形態における電子機能素子は、公知の磁気ランダムアクセスメモリ（以下、単に「ＭＲＡＭ」と呼ぶ。）における強磁性層を置換する、上記の実施の形態１におけるペロブスカイト型酸化物からなる層を有するＭＲＡＭである。

【０１２７】

上記の実施の形態１において、本発明者等は、電圧印加によりモット転移したペロブスカイト型酸化物に強磁性が出現することを見出した。本実施の形態におけるＭＲＡＭは、本発明者等が見出したペロブスカイト型酸化物に出現する強磁性を利用するものである。

【０１２８】

なお、ＭＲＡＭの基本となる素子として巨大磁気抵抗効果を用いた素子とトンネル磁気抵抗効果を用いた素子の２種類がある。本実施の形態では、いずれの素子についても適用可能である。

【０１２９】

図１０は、本実施の形態におけるＭＲＡＭの基本的な素子の構成を示す斜視図である。

【０１３０】

図１０に示すように、本実施の形態におけるＭＲＡＭ３０は、第１強磁性層３１と、非磁性層３２と、第２強磁性層３３とが、この順に配置された３層構造を備えている。

【０１３１】

このＭＲＡＭ３０の第１強磁性層及び第２強磁性層３１、３３は、上記の実施の形態１におけるペロブスカイト型酸化物から構成されている。そして、このＭＲＡＭ３０のメモリ情報は、第１強磁性層及び第２強磁性層３１、３３の各スピンの向きにより保持されており、この第１強磁性層及び第２強磁性層３１、３３の向きが相対的に平行か反平行かによりメモリ情報の「１」、「０」を規定している。

【０１３２】

通常、第１強磁性層３１と第２強磁性層３３との相対的なスピンの向きが反平行のとき、スピンの向きが平行のときに比べて、磁気抵抗の値が大きくなる。この磁気抵抗の値の差を利用して、メモリ情報の「１」、「０」の違いを読み出すことができる。

【０１３３】

上記の実施の形態１におけるペロブスカイト型酸化物の強磁性の出現は、上述したように、温度が１０Ｋの付近で観測されている。このため、本実施の形態におけるＭＲＡＭは、例えば、冷凍機等の冷却装置を制御するための制御装置に搭載される記憶装置として用いることができる。

【０１３４】

〔実施の形態４〕

次に、本発明の実施の形態４について説明する。本発明の実施の形態４では、上記の実施の形態１におけるペロブスカイト型酸化物を用いた電子機能素子を備えるメモリ装置について説明する。

【０１３５】

本実施の形態におけるメモリ装置は、抵抗変化型メモリ（以下、単に「ＲｅＲＡＭ」と呼ぶ）である。

【０１３６】
図１２には、本実施の形態に係る電子機能素子１００の構造が示されている。この電子機能素子１００は、電界効果トランジスタ（ＦＥＴ）である。図１２に示すように、電子機能素子１００は、基板５０上に形成されている。この基板５０に、ソース領域５１と、ドレイン領域５２が形成されている。ソース領域５１とドレイン領域５２との間のチャンネル５３の上には、ゲート絶縁膜５４が形成されている。また、ソース領域５１上には、上記の実施の形態１におけるペロブスカイト型酸化物から成る可変抵抗素子層５５が積層されている。
【０１３７】
図１２に示すように、ドレイン領域５２にビット線６０を接続し、ゲート絶縁膜５４をワード線６１に接続し、可変抵抗素子層５５をソース線６２に接続すれば、電子機能素子１００をメモリセルとして用いることができる。
【０１３８】
図１３には、電子機能素子１００をメモリセルとするメモリ装置２００の構成が示されている。メモリ装置２００は、メモリセルとしての電子機能素子１００、ビット線６０、ワード線６１、ソース線６２に加え、ゲート電圧調整手段７０、ソース電圧調整手段７１、データ読出手段７２、温度調整手段７３、圧力調整手段７４を備える。
【０１３９】
ゲート電圧調整手段７０は、ワード線６１に接続されている。ソース電圧調整手段７１は、ビット線６０、ソース線６２に接続されている。データ読出手段７２はビット線６０に接続されている。書き込み又は読み出しを行う際に、ゲート電圧調整手段７０は、ワード線６１を介してゲート絶縁膜５３に適切な電圧を印加する。そして、ソース電圧調整手段７１は、ビット線６０とソース線６２を介して、可変抵抗素子層５５→ソース領域５１→チャンネル５３→ドレイン領域５２間に電圧を印加する。データ読出手段７２は、ビット線６０の電位に基づいて、電子機能素子１００に保持されたデータを読み出す。
【０１４０】
温度調整手段７３は、メモリ装置２００の温度、すなわち電子機能素子１００の周辺の雰囲気温度を調整する。圧力調整手段７４は、例えば、不図示の圧電素子などを駆動して可変抵抗素子層５５に圧力を加えてひずみを与える。
【０１４１】
このメモリ装置２００は、温度調整手段７３によって調整される電子機能素子１００の温度によっては、ＲＯＭ（Read Only Memory）としても動作するし、ＲＡＭ（Random Access Memory）としても動作する。
【０１４２】
図１４には、電子機能素子１００の可変抵抗素子層５５として採用されるペロブスカイト型酸化物の一例であるモット絶縁体$Ca_2RuO_4$の抵抗の温度依存性のグラフが示されている。このグラフでは、可変抵抗素子層５５に０．２６ＧＰａの圧力を加えた状態で、雰囲気温度を３００Ｋ以下の温度から３３０Ｋ以上の温度へ昇温し、続いて３００Ｋ以下の温度に降温させたときのモット絶縁体$Ca_2RuO_4$の抵抗の変化の様子が示されている。
【０１４３】
図１４に示すように、雰囲気温度を３００Ｋ付近から昇温させると、モット絶縁体$Ca_2RuO_4$は、第１の温度としての３２８Ｋで金属体に相転移する。金属体に相転移した後、雰囲気温度を降温させると、モット絶縁体$Ca_2RuO_4$は、雰囲気温度が３２８Ｋより下がっても金属体のままであるが、第２の温度としての３０２Ｋで絶縁体に相転移する。
【０１４４】
ここで、３０２Ｋより小さい温度領域を絶縁体相Iとし、３０２Ｋ以上３２８未満を双安定相IIとし、３２８Ｋ以上を金属相IIIとする。絶縁体相Iと、双安定相IIとでは、モット絶縁体$Ca_2RuO_4$は、異なった電圧－電流特性を示す。
【０１４５】

図１５には、０．２６ＧＰａの圧力を加え、雰囲気温度を３０１Ｋとしたときの、モット絶縁体$Ca_2RuO_4$の電圧－電流特性の一例が示されている。図１５に示すように、印加する電圧を０Ｖから上げていくと、モット絶縁体$Ca_2RuO_4$は、約１．４Ｖ付近で、絶縁体から金属体に相転移する。さらに、金属体に相転移したモット絶縁体$Ca_2RuO_4$に対して印加する電圧を下げていき、その電圧が約０．５Ｖになると、モット絶縁体$Ca_2RuO_4$は、金属体から絶縁体に相転移する。この圧力条件及び温度条件において、モット絶縁体$Ca_2RuO_4$の電圧－電流特性は、電圧の正負によらず、対称となっている。

【０１４６】

この特性を利用して、圧力調整手段７４により、可変抵抗素子層５５に０．２６ＧＰａの圧力を加え、温度調整手段７３により、雰囲気温度を絶縁体相I（例えば３０１Ｋ）に調整すれば、メモリ装置２００を、揮発性メモリとして動作させることができる。

【０１４７】

電子機能素子１００にデータをセットする際には、ゲート電圧調整手段７０によりワード線６１を介して電子機能素子１００にゲート電圧を印加しつつ、ソース電圧調整手段７１により、ソース線６２及びビット線６０を介して、可変抵抗素子層５５に、第１の電圧としての約１．４Ｖ以上の電圧を印加する。これにより、可変抵抗素子層５５は、金属体に遷移する。

【０１４８】

データをセットした後、可変抵抗素子層５５には、０．５Ｖ以上１．４Ｖ未満の電源電圧が印加されている。これにより、可変抵抗素子層５５の抵抗値は維持されている。したがって、ゲート電圧調整手段７０によりゲート電圧を印加すれば、データ読出手段７２が、ビット線６０の電位を読み取ることにより、セットされたデータを読み出すことができる。

【０１４９】

また、データをセットした後にリセットする際には、ゲート電圧調整手段７０によりワード線６１を介して電子機能素子１００にゲート電圧を印加しつつ、ソース電圧調整手段７１によりソース線６２及びビット線６０を介して可変抵抗素子層５５に印加する電圧を、第２の電圧としての０．５Ｖより低くする。これにより、可変抵抗素子層５５は、絶縁体に遷移する。

【０１５０】

上述のように、可変抵抗素子層５５には、０．５Ｖ以上１．４Ｖ未満の電源電圧が印加されている。これにより、可変抵抗素子層５５の抵抗値は維持されている。したがって、ゲート電圧調整手段７０によりゲート電圧を印加すれば、データ読出手段７２が、ビット線６０の電位を読み取ることにより、リセットされたデータを読み出すことができる。

【０１５１】

一方、図１６には、０．２６ＧＰａの圧力を加え、雰囲気温度を３１０Ｋに調整したときの、モット絶縁体$Ca_2RuO_4$の電圧－電流特性の一例が示されている。図１６に示すように、印加する電圧を０Ｖから上げていくと、モット絶縁体$Ca_2RuO_4$は、約１．４Ｖ付近で、絶縁体から金属体に相転移する。しかしながら、金属体に相転移したモット絶縁体$Ca_2RuO_4$に対して、印加する電圧を下げていっても、モット絶縁体$Ca_2RuO_4$は、金属体の状態を維持し続ける。この場合のモット絶縁体$Ca_2RuO_4$の電圧－電流特性は、電圧０に対して非対称となる。

【０１５２】

この特性を利用して、圧力調整手段７４により、可変抵抗素子層５５に０．２６ＧＰａの圧力を加え、温度調整手段７３により、雰囲気温度を双安定相II（例えば３１０Ｋ）に調整すれば、メモリ装置２００を、不揮発性メモリとして機能させることができる。

【０１５３】

電子機能素子１００にデータをセットする際には、ゲート電圧調整手段７０によりゲート電圧を印加しつつ、ソース電圧調整手段７１により、可変抵抗素子層５５に、第１の電圧としての１．４Ｖ以上の電圧を印加する。

【０１５４】
その後、可変抵抗素子層５５に印加される電圧が０になっても、可変抵抗素子層５５の抵抗値は維持されているため、ゲート電圧調整手段７０によりゲート電圧を印加すれば、データ読出手段７２がビット線６０の電位を読み取ることにより、セットされたデータを読み出すことができる。
【０１５５】
絶縁体相I、双安定相II、絶縁体相IIIの温度範囲は、圧力調整手段７４によって可変抵抗素子層５５に加えられる圧力によって調整することができる。図１７に示すように、可変抵抗素子層５５に加えられる圧力が０．２６ＧＰａとなっている場合には、絶縁体から金属体への第１の温度は３２８Ｋであり、金属体から絶縁体への第２の温度は３０２Ｋであった。
【０１５６】
これに対して、可変抵抗素子層５５に加えられる圧力が０ＧＰａとなっている場合には、絶縁体から金属体への第１の温度は３６２Ｋであり、金属体から絶縁体への第２の温度は、３４４Ｋであった。このように、可変抵抗素子層５５に加えられる圧力を調整すれば、揮発性メモリとして動作させる時の温度や、不揮発性メモリとして動作させる時の温度を変えることができる。
【０１５７】
逆に言うと、可変抵抗素子層５５に印加される電圧を変えるのではなく、可変抵抗素子層５５に加えられる圧力を変化させることによって、メモリ装置２００のデータのセット、リセットを制御するようにすることもできる。
【０１５８】
同様に、可変抵抗素子層５５の周辺の雰囲気温度を変化させることによって、メモリ装置２００のデータのセット、リセットを制御するようにすることもできる。
【０１５９】
このように、上記の実施の形態１におけるペロブスカイト型酸化物を用いたトランジスタ１００を用いれば、常温常圧下において、ＲＯＭとＲＡＭの両方の特性を必要に応じて使い分けることができるメモリを作製することができる。
【０１６０】
なお、ＲｅＲＡＭの構成は、図１２、図１３に示すものには限られず、他の回路構成を有するＲｅＲＡＭであっても、図１３乃至図１７に示されるペロブスカイト型酸化物の温度、電圧、圧力に関する特性を利用して、高速で駆動するＲＯＭ、ＲＡＭを構築することは可能である。例えば、図９に示す電界効果トランジスタ２０を用いて、メモリ装置を構築するようにしてもかまわない。
【０１６１】
また、上述した特性を考慮すれば、電子機能素子１００を圧力センサーやひずみゲージとして用いることも可能である。
【０１６２】
〔その他の実施の形態〕
上記の実施の形態２においては、上記の実施の形態１におけるペロブスカイト型酸化物を用いた電界効果トランジスタを開示し、上記の実施の形態３においては、上記の実施の形態１におけるペロブスカイト型酸化物を用いたＭＲＡＭを開示し、上記の実施の形態４においては、上記の実施の形態１におけるペロブスカイト型酸化物を用いたＲｅＲＡＭを開示したが、本発明はこれらに限られるものではない。
【０１６３】
例えば、上記の実施の形態１におけるペロブスカイト型酸化物の低温状態での強磁性の出現現象を利用した温度検出素子や磁場センサーであっても、本発明に含まれるものである。
【０１６４】
また、上記の実施の形態３におけるＭＲＡＭは、図１１に示したように、３層構造を基

本とするものであったが、本発明はこの構造に限られるものではない。例えば、図１１に示すように、単層構造のＭＲＡＭも実現可能である。

【０１６５】

すなわち、図１１に示すＭＲＡＭ４０は、ペロブスカイト型酸化物層４１の上部に複数の第１電極配線$V_1$～$V_4$を配置すると共に、その下部に複数の第２電極配線$H_1$～$H_4$を配置している。そして、これら第１電極配線$V_1$～$V_4$と第２電極配線$H_1$～$H_4$とは互いに交差し、マトリックス状に配置されている。

【０１６６】

これまでの圧力印加により誘起される強磁性では、磁場の方向で正負の符号を異にする約８０％の磁気抵抗が得られるという、異方的巨大磁気抵抗効果が観測されている。

【０１６７】

この効果は、高性能の磁気センサーとしての利用が期待されるが、圧力印加中の現象を実用化するには困難が多かった。

【０１６８】

一方、図１１に示すＭＲＡＭ４０では、強磁性の誘起が電場印加によるため、その制御が簡単であり、上記のような異方的巨大磁気抵抗効果を容易に実用化できる。

【０１６９】

例えば、図１１に示したＭＲＡＭ４０において、図中Ａで示す領域に強磁性を誘起させる場合であれば、この領域に第１電極配線$V_2$と第２電極配線$H_2$とを用いて電圧を与えて、この領域に電場を印加すればよい。そうすることにより、この領域のみに強磁性を出現させることができる。

【０１７０】

本発明は上述した各実施形態に限定されるものではなく、請求項に示した範囲で種々の変更が可能であり、異なる実施形態にそれぞれ開示された技術的手段を適宜組み合わせて得られる実施形態についても本発明の技術的範囲に含まれる。

【０１７１】

例えば、上記実施の形態では、ペロブスカイト型酸化物が絶縁体から金属体へ遷移する印加電場のしきい値を、８０Ｖ／ｃｍとしたが、実際には、４０Ｖ／ｃｍ程度までしきい値を低下させることができることが可能である。すなわち、ペロブスカイト型酸化物を前記金属相に相転移させるために印加すべき電場のしきい値の設定範囲は、雰囲気中が常温であるときに４０Ｖ／ｃｍ以上８０Ｖ／ｃｍ以下となる。

【産業上の利用可能性】

【０１７２】

本発明のペロブスカイト型酸化物の相転移を誘起するための相転移誘起方法は、電場を用いてスイッチングさせることを原理とする電子機能素子等に適用できる。

【符号の説明】

【０１７３】

１０　測定回路
１１　負荷抵抗
１２　試料
１３　電圧源
１４　電流計
１５　電場印加装置
１６　電圧計
２０　電界効果トランジスタ
２１　ゲート電極
２２　ゲート絶縁層
２３　ソース領域
２４　ドレイン領域
２５、４１　ペロブスカイト型酸化物層

２６　基板
３０、４０　ＭＲＡＭ
３１　第１強磁性層
３２　非磁性層
３３　第２強磁性層
５０　基板
５１　ソース領域
５２　ドレイン領域
５３　チャンネル
５４　ゲート絶縁膜
５５　可変抵抗素子層
６０　ビット線
６１　ワード線
６２　ソース線
７０　ゲート電圧調整手段
７１　ソース電圧調整手段
７２　データ読出手段
７３　温度調整手段
７４　圧力調整手段
１００　電子機能素子
２００　メモリ装置
$V_1$、$V_2$、$V_3$、$V_4$　第１電極配線
$H_1$、$H_2$、$H_3$、$H_4$　第２電極配線

【図１】

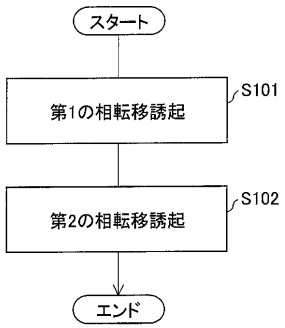


【図２】

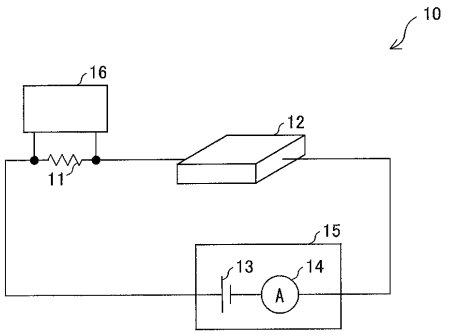

【図３】

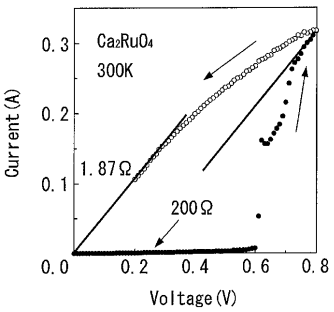
Ca2RuO4
300K
1.87Ω
200Ω
Current(A)
Voltage(V)
0.0
0.1
0.2
0.3
0.2
0.4
0.6
0.8

【図４】

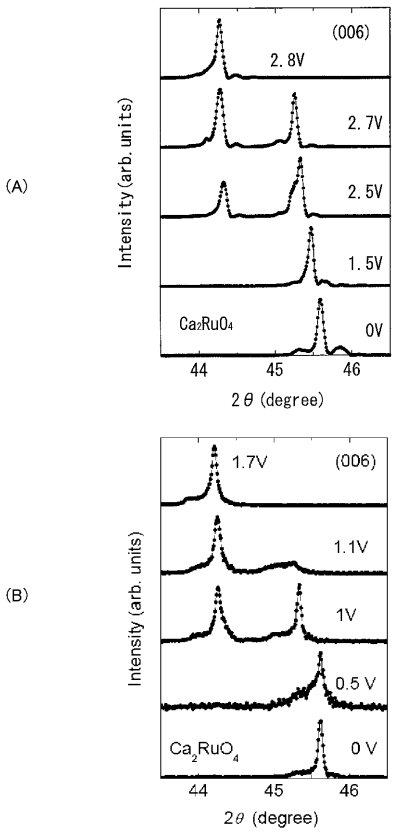
(A)
(006)
2.8V
2.7V
2.5V
1.5V
0V
Ca2RuO4
Intensity(arb.units)
44
45
46
2θ (degree)
(B)
1.7V
(006)
1.1V
1V
0.5V
0V
Ca2RuO4
Intensity (arb. units)
44
45
46
2θ (degree)

【図５】

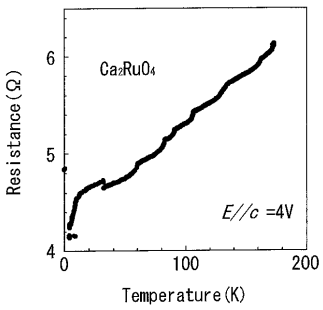
Ca2RuO4
E//c =4V
Resistance(Ω)
Temperature(K)
4
5
6
0
100
200

【図６】

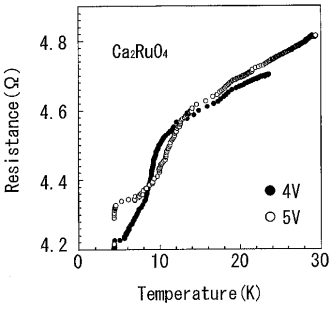
Ca2RuO4
4V
5V
Resistance(Ω)
Temperature(K)
4.2
4.4
4.6
4.8
0
10
20
30

【図７】

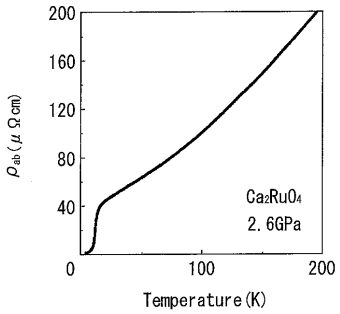
200
160
120
80
40
0
100
200
$\rho_{ab}$ ($\mu\Omega$cm)
Temperature (K)
$Ca_2RuO_4$
2.6GPa

【図８】

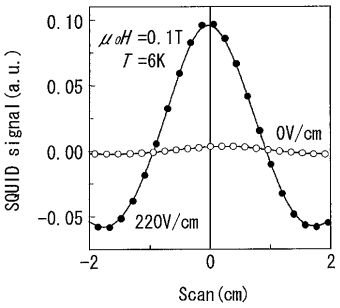
0.10
0.05
0.00
−0.05
−2
0
2
SQUID signal (a.u.)
Scan (cm)
$\mu_0 H$ =0.1T
$T$ =6K
0V/cm
220V/cm

【図９】

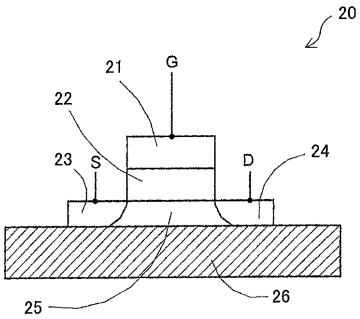
20
21
G
22
23
S
D
24
25
26

【図１０】

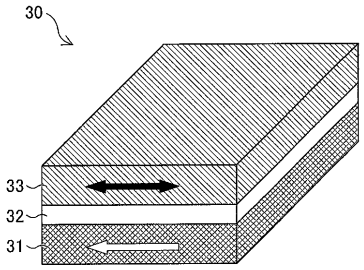
30
33
32
31

【図１１】

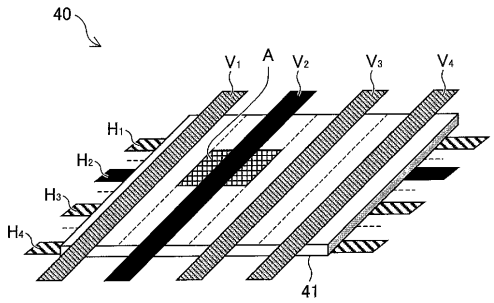


【図１２】

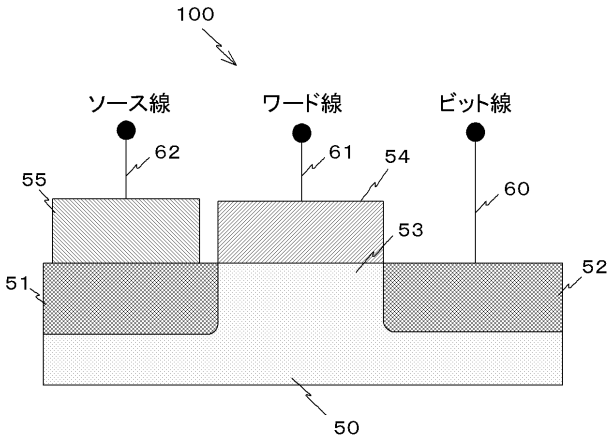


【図１３】

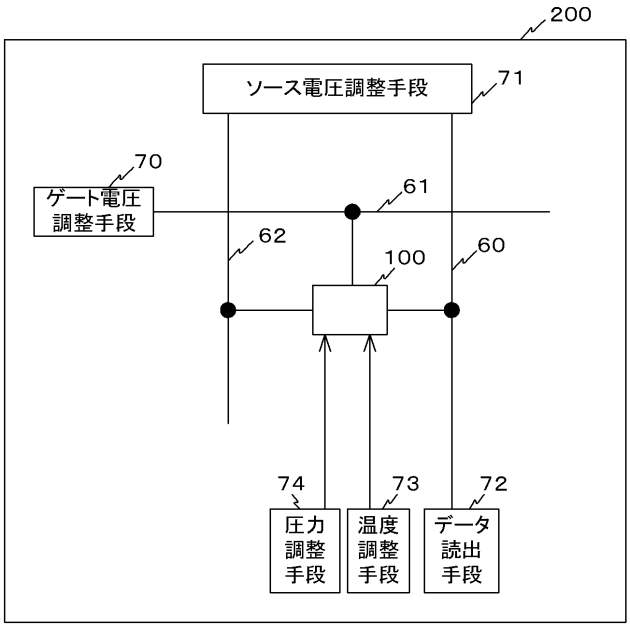


【図１４】

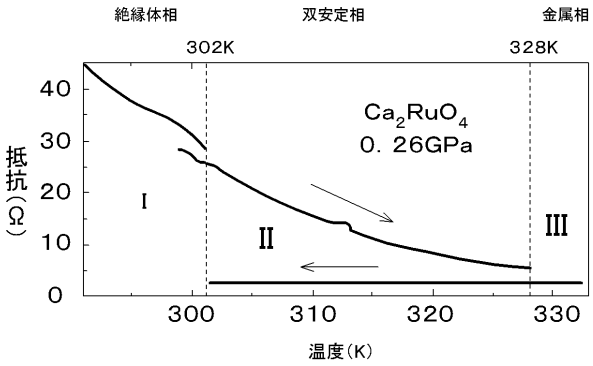

【図１５】

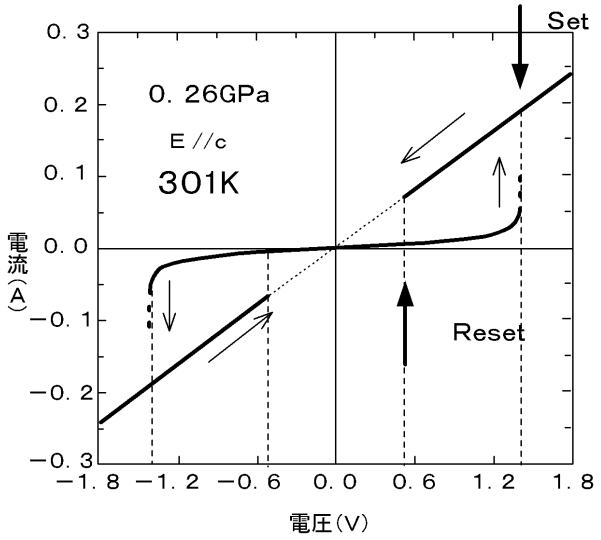
絶縁体相 I
Set
Reset
0.26GPa
E //c
301K
電流(A)
電圧(V)
0.3
0.2
0.1
0.0
−0.1
−0.2
−0.3
−1.8 −1.2 −0.6 0.0 0.6 1.2 1.8

【図１６】

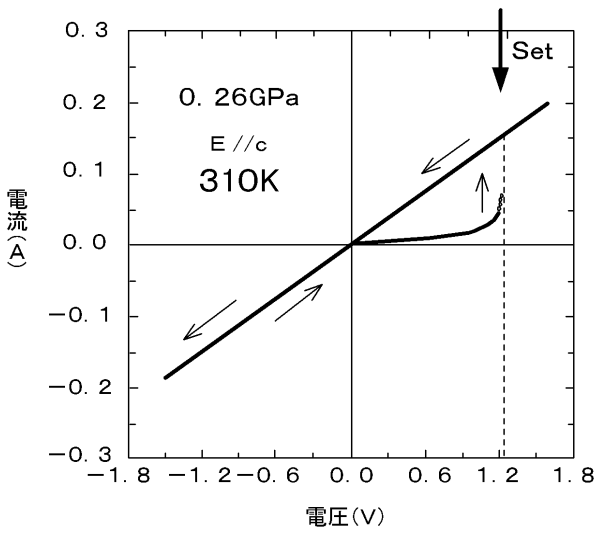
双安定相 II
Set
0.26GPa
E //c
310K
電流(A)
電圧(V)
0.3
0.2
0.1
0.0
−0.1
−0.2
−0.3
−1.8 −1.2 −0.6 0.0 0.6 1.2 1.8

【図１７】

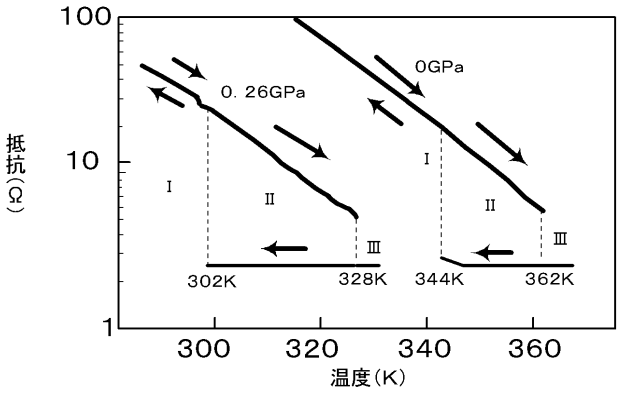
0.26GPa
0GPa
I
II
III
302K
328K
344K
362K
抵抗(Ω)
温度(K)
100
10
1
300 320 340 360

フロントページの続き

| (51) Int.Cl. | | F I | | | テーマコード（参考） |
|---|---|---|---|---|---|
| ***H01L 49/00*** | ***(2006.01)*** | H01L | 49/00 | Z | 5F110 |
| ***H01L 29/786*** | ***(2006.01)*** | H01L | 29/78 | 618B | |
| ***H01L 29/84*** | ***(2006.01)*** | H01L | 29/84 | Z | |
| *C01G 55/00* | *(2006.01)* | C01G | 55/00 | | |

(72) 発明者 竹本 哲雄
広島県東広島市鏡山一丁目３番１号 国立大学法人広島大学大学院先端物質科学研究科内
(72) 発明者 坂木 麻里子
広島県東広島市鏡山一丁目３番１号 国立大学法人広島大学大学院先端物質科学研究科内
(72) 発明者 山内 洋平
広島県東広島市鏡山一丁目３番１号 国立大学法人広島大学大学院先端物質科学研究科内

Ｆターム(参考) 4G048 AA05 AB03 AD08
4M112 AA01 BA01 BA03 CA41 CA42 CA47 CA48 CA49 CA51 CA52
CA53 DA06 DA07 DA09 DA13 EA01 EA03 EA11 EA13 FA01
FA07 GA03
4M119 BB01 BB03 DD42
5F083 CR20 FZ10 JA60
5F092 AB07 AC08 AC12 BB25 BB45
5F110 AA30 BB13 CC02 GG01 GG42 GG43